Micro/Nano-Scale Light Sources for Integrated Photonics on Silicon

Mohammad Hadi Tavakoli Dastjerdi



Department of Electrical and Computer Engineering
Faculty of Engineering
McGill University
Montreal

January 2015

A thesis submitted to McGill University in partial fulfillment of the requirements of the degree of Doctor of Philosophy

© Mohammad Hadi Tavakoli Dastjerdi 2015

To my family

Table of Contents

Table of Co	ontents	i
	ires	
	les	
	onyms	
	,	
Abrégé		xi
	on of Authors	
	. Introduction	
1.1 Opt	ical Interconnects	3
1.2 Rol	led-up Microtubes	4
1.2.1	Fabrication Principles of Rolled-up Semiconductor Tubes	4
1.2.2	Transfer of Rolled-up Tube Structures	7
1.2.3	Optical Characteristics and Control of the Optical	
	Resonance Modes	8
1.3 FD'	TD Analysis of Rolled-up Tubes and Dielectricl Planar Waveuide	
Mo	del	12
1.4 Rec	ent Developments of Microtube-Based Devices	14
1.4.1	Biosensors	14
1.4.2	Optical Communications	15
1.4.3	Other Applications	15
1.5 Ult	raviolet LEDs	16
	Nanowire LEDs	
1.6 Org	ganization of the Thesis	18
	Optically-Pumped Quantum Dot/Dash Tube Lasers at Telec	
_	th	
	oduction	
2.2 InA	s/InGaAsP Quantum Dot Tube Lasers at 80 K	
2.2.1	Device Design and Fabrication Procedure	
	Photoluminescence Studies and Discussions	
	s/InGaAsP Quantum Dash Tube Lasers at Room Temperature	
	Fabrication Procedure and Optimization	
	Photoluminescence Studies and Discussions	
	nclusion	34
-	. InAs/GaAs Rolled-up Quantum Dot Tube Infrared Photoder	
Devices	•••••••	
	oduction	
	vice Design and Fabrication Procedure	
3.3 Me	asurement Results and Discussion	
24 (l	11

Chapter 4.	Electrically Injected InP/InGaAsP Quantum Well Tube La	asers at
Telecom W	Vavelength	42
4.1 Intro	oduction	42
	Ga _{1-x} As Quantum Well Heterostructure Design	
4.3 Fab	rication Procedure	45
4.4 Elec	etroluminescence Results and Discussion	48
4.5 Con	clusion	53
Chapter 5.	Deep Ultraviolet AlN Nanowire LEDs	54
5.1 Intro	oduction	54
5.2 AlN	I nanowire LEDs	55
5.2.1	Growth of Nanowire LEDs	55
5.2.2	Fabrication Procedure and Characterization	56
5.3 Pass	sivation Polymer Material for UV Nanowire LEDs	59
5.4 Con	clusion	62
Chapter 6.	Conclusions and Future Works	63
_	clusions	
6.2 Futi	ıre Works	65
6.2.1	SiOx Rolled-up Microtubes	65
6.2.2	III-N Rolled-up Tubes	68
6.2.3	Incorporation of Other Active Materials for Microtube Light	
	Sources	69
6.2.4	Room temperature electrically injected rolled-up Lasers and	
	Photodetectors	72
Bibliograph	ıy	

List of Figures

Figure 1.1 Illustration of the rolling mechanism for a strained InAs/GaAs bilayer membrane [29]
Figure 1.2 Illustration of the fabrication of free-standing semiconductor tube optical cavities. (a) Lithographically defined U-shaped mesa. (b) Rolled-up tube resulting from the sacrificial etching and release of the U-shaped mesa. (c) Optical microscopy image of a rolled-up InGaAsP tube
Figure 1.3 (a) Schematic illustration of the transfer method with the use of abruptly tapered optical fibers. (b) Optical microscopy image of a semiconductor tube on the tip of an abrupt fiber taper. Inset: Scanning electron microscopy image of the transition between the glass fiber and the tube [50]
Figure 1.4 (a) Illustration of the spiral geometry of a rolled-up tube, showing the presence of inner and outer notches. (b) SEM image of the free-standing part of a tube device showing the presence of surface corrugations for axial mode confinement
Figure 1.5 (a) Photoluminescence spectrum of a microtube with an average wall thickness of ~ 100 nm. The corresponding mode numbers are identified. Shown in the inset are the optical microscopy image of the lithographically defined U-shaped mesa and schematic of the electric field of the first few axial modes. (b) Photoluminescence spectrum of a microtube with a wall thickness of ~ 50 nm shown with the corresponding mode numbers. Shown in the inset are the optical microscopy image of the U-shaped mesa and schematic of the electric field of the first few axial modes. The scale bar corresponds to a length of 50 μ m in both (a) and (b) [60]
Figure 1.6 (a) Calculated resonance mode distribution of a tube cavity using a two-dimensional finite-difference time-domain algorithm. (b) Calculated electric field distribution, plotted using a linear color scale to emphasize the field confinement. The black arrow marks the position of the inner rolling edge. Inset: Detail of the marked square, using a modified color scale to emphasize the directional emission pattern [50]. 12
Figure 1.7 Cross-section of a tube structure showing different wall thicknesses with inner and outer notches in the structure
Figure 1.8 The epitaxial growth of (a) epilayer, and (b) nanowire structure. Due to the lattice mismatched substrate, the epilayer experiences severe strain. However, due to the lateral stress relaxation, stress is properly accommodated in nanowire structure
Figure 2.1 (a) Schematic illustration of InAs/InGaAsP quantum dot heterostructures grown on InP substrate. (b) Illustration of the U-shaped mesa defined to obtain free-

standing tubes. The starting edge, rolling direction, and stopping edge defined by a photoresist layer are also shown. (c) Schematic illustration of a free-standing quantum dot tube structure
Figure 2.2 (a) Optical microscopy image of a rolled-up tube. (b) Scanning electron microscopy image showing a detailed view of the surface modifications [94]
Figure 2.3 PL spectra of a tube device measured at 82 K. The lower (weaker) spectrum corresponds to a small incident pump power of 180 nW, while the upper (stronger) one was measured at a high incident pump power of 5.6 μW. The lower intensity spectrum has been multiplied by 10 to improve its visibility. The dashed line represents the spectrum (multiplied 75 times, for better visibility) of an as-grown quantum do heterostructure measured at the same temperature for reference [94]
Figure 2.4 Light-light curve (circles) for modes (22,1) (circles) and (22,4) (squares) in Fig. 3.3. Mode (22,1) shows a lasing threshold of 1.26 μW pump power. The dashed line are a guide to estimate the threshold power. Mode (22,4) shows no threshold behavior The background emission extracted from the box in Fig. 3 (multiplied by a factor of 5 for better visibility) is indicated by the open diamonds. Inset: Full-width half-maximum (FWHM) of mode (22,1) as a function of pump power [94]
Figure 2.5 (a) Schematic illustration of InAs/InGaAsP quantum dash heterostructures grown on InP substrate. (b) Illustration of the U-shaped mesa. (c) Illustration of the formation of rolled-up InAs/InGaAsP quantum dot/dash microtubes when the underlying InP substrate is selectively etched. (d) Schematic of free-standing microtubes with SiO protective layer covering the side pieces of the U-shaped mesa [60]
Figure 2.6 (a) SEM image of a free-standing microtube rolled along the [100] crystal direction. (b) Optical microscopy image from arrays of rolled-up InAs/InGaAsP tuber showing high fabrication yield. (c) SEM image of a microtube illustrating the engineered surface corrugations for axial mode confinement. (d) Cross-sectional SEM image of the microtube showing multiple turns. (e) SEM image from arrays of rolled-up InAs/InGaAsP tubes showing high fabrication yield
Figure 2.7 (a) Photoluminescence spectrum of a quantum dash microtube measured a room temperature with an incident pump power of \sim 19.9 μ W. The measured spectrum of the as-grown quantum dash sample is shown as the dashed lines and also in the inset. The curves are vertically shifted for display purpose. (b) Integrated intensity vs. pump power for the mode (21,2) and for the background emission extracted from the box shown in (a). The inset shows the FWHM of the mode (21,2) measured under various inciden pump powers [60].
Figure 2.8 Simulated distribution of the resonance mode in a rolled-up InGaAsI microtube with a radius of \sim 2.4 μ m and wall thickness of \sim 100 nm by the two dimensional finite-difference time-domain method. The presence of inside and outside notches are shown by the arrows [60].

Figure 3.1 (a) Schematic illustration of the fabrication of InAs quantum dot tube photodetectors. The p-i-n junction is defined by selective Si and Be implantation. The undoped active region is not drawn to scale. The tube device is formed by selectively etching the underlying AlAs sacrificial layer of a U-shaped mesa. The InAs/GaAs quantum dot heterostructure is shown in the inset. (b) SEM image of the fabricated InAs quantum dot tube photodetector. The arrow indicates the tube rolling direction [72] 37
Figure 3.2 (a) Measured current versus voltage under dark condition. The inset shows the I-V under 632.8 nm and 1064 nm excitation at 300 K. (b) Responsivity of the tube detector versus the applied bias for 1064 nm excitation at 84 K and 300 K [72]
Figure 4.1 (a) Schematic of coherently strained InGaAs/InGaAsP quantum well heterostructures grown on semi-insulating InP substrate. (b) Photoluminescence spectrum measured at room temperature [112].
Figure 4.2 (a) Optical microscopy image of a free-standing rolled up tube device with the presence of n- and p-metal contacts on the two side pieces. The yellow arrow shows the rolling direction of the tube device. (b) SEM image of the fabricated tube device with <i>n</i> - and <i>p</i> -metal contacts. (c) SEM image of the tube device showing the side view of the tube cavity. (d) SEM image of the free-standing part of the tube device showing the presence of surface corrugations for axial mode confinement [112]
Figure 4.3 Schematic flowchart presenting the key device fabrication steps
Figure 4.4 (a) Measured current-voltage characteristic of the device at room temperature. (b) Schematic of the electrically injected free-standing rolled-up tube laser on InP substrate [112]
Figure 4.5 (a) Electroluminescence spectra of the rolled-up tube device measured at 0.9 mA (below threshold) and 1.25 mA (above threshold). (b) Integrated intensity versus current for the mode (24,1) and for the background emission extracted from the box shown in (a). Inset: Full-width-at-half-maximum of the mode (24,1) versus current. (c) Resonance mode distribution in a rolled-up InGaAsP tube with a wall thickness of ~140 nm and diameter of ~ 5µm calculated by the two-dimensional finite-difference time-domain method. The presence of inside notch is shown by the arrow [112]
Figure 4.6 Schematic of coherently strained InAs/InGaAsP QD heterostructures grown on semi-insulating InP substrate
Figure 5.1 (a) SEM image of AlN/GaN nanowires grown on Si substrate. (b) PL spectra taken from AlN:Mg nanowires at room temperature and low temperature with an excitation of 1 mW [119]
Figure 5.2 (a) Schematic diagram of the AlN <i>p-i-n</i> LED on GaN template on Si substrate. (b) Schematic diagram of the fabricated UV LED

Figure 5.3 (a) The I-V characteristics of AlN LEDs (b) The EL spectra of AlN LEDs under different injection levels measured at room temperature with the inset showing the output [119]
Figure 5.4 (a) Variations of the light extraction efficiency with nanowire diameter. (b) Variations of the light extraction efficiency with nanowire spacing
Figure 5.5 Final thickness of the spin-coated polyisobutylene/toluene solution measured on silicon wafer using ellipsometry versus the solution concentration. The solution was spin coated for 65 sec at 4000 rpm.
Figure 5.6 Absorption spectrum for spin-coated polyisobutylene/toluene and polyimide coatings with $\sim 1 \mu m$ thickness
Figure 6.1 SiO/SiO2 rolled-up tube on Si substrate.
Figure 6.2 SiO/SiO2 rolled-up tube using InGaAsP sacrificial layer
Figure 6.3 (a) Schematic of GaN LED and nanotube structure. Snapshot of the time domain simulation showing the electrical field pattern of the structure: (b) without nanotube and (c) with nanotube [123].
Figure 6.4 (a) Rolled-up GaAs-based microtubes embedding long InN NWs. The devices are mostly broken during rolling due to large dimensions of the NWs. (b) Rolled-up GaAs-based microtubes embedding short InN NWs

List of Tables

List of Acronyms

CBE Chemical Beam Epitaxy

CMOS Complementary Metal-Oxide Semiconductor

DUV Deep Ultraviolet

EL Electroluminescence

EQE External Quantum Efficiency

FDTD Finite-Difference Time-Domain

FSR Free Spectral Range

FWHM Full-Width-at-Half-Maxima

HF Hydro-Fluoric

IR InfraRed

LED Light Emitting Diode

MBE Molecular Beam Epitaxy

MOCVD Metal-Organic Chemical Vapor Deposition

MOVPE Metal-Organic Vapor Phase Epitaxy

MQW Multiple Quantum Well

NC Nano Crystal

NIR Near InfraRed

PAMBE Plasma Assisted Molecular Beam Epitaxy

PD Photo Detector

PECVD Plasma-Enhanced Chemical Vapor Deposition

PL Photoluminescence

QCSE Quantum Confined Stark Effect

QD Quantum Dot

QW Quantum Well

RF Radio Frequency

RIE Reactive Ion Etching

RPM Revolutions Per Minute

TE Transverse Electric

TM Transverse Magnetic

UV Ultraviolet

WGM Whispering Gallery Mode

Abstract

In order to achieve highly efficient and compact light sources for chip-level optical communications, different types of microcavity structures have been extensively studied. Among them, rolled-up III-V semiconductor microtubes exhibit distinct characteristics including directional emission and polarization control and can be readily transferred on Si substrate. Such tubular structures are formed when a coherently strained nanomembrane is selectively released from its native substrate. This dissertation reports on the achievement, for the first time, of III-V based optically and electrically pumped microtube lasers and also photodetectors operating at telecom wavelength. Furthermore, we report on the achievement of the first AlN nanowire LEDs emitting at 210 nm. One of the principle advantages of such III-N nanowire structures compared to their planar counterparts is their ability to grow dislocation-free crystal on a foreign substrate.

We have achieved lasing at telecom wavelength region from InAs/InGaAsP quantum dot/dash rolled-up tube devices at 80 K and room temperature with extremely low threshold values of $\sim 1.2~\mu W$ and $\sim 6~\mu W$, respectively.

We have also reported InAs/GaAs quantum dot rolled-up photodetector tube devices in which the light absorption length and charge carrier transport can be separately optimized. At room temperature the devices show a responsivity of ~ 0.066 A/W at 1064 nm, with an external quantum efficiency of $\sim 8\%$.

Through optimizing the design and fabrication, we have demonstrated, for the first time, electrically injected InGaAs/InGaAsP quantum well rolled-up tube lasers operating at \sim 1.5 μ m. Such devices present a threshold of \sim 1.05 mA at 80 K. This paves the way for the practical implementation of such tubular optical cavities in chip-level optical communication systems.

Furthermore, we have achieved the first nanowire based AlN deep UV p-i-n LEDs with emission at ~ 210 nm. These devices exhibit a turn-on voltage of ~ 6 V and a low operating voltage (8 V at 20 mA). We have also studied the optical characterization and processing of a new polymer to be used as the passivating material for UV nanowire LED fabrication.

Abrégé

Afin d'obtenir des sources de lumière très efficaces et compactes pour les communications optiques au niveau de la puce, les différents types de structures en microcavités ont été largement étudiés. Parmi eux, les microtubes enroulés présentent des caractéristiques distinctes, notamment les émissions directionnelles et le contrôle de la polarisation. Ils peuvent également être facilement transférés sur un substrat en Si. Ces structures tubulaires sont formées quand un nanomembrane cohérentement tendues est libéré d'une manière sélective de son substrat d'origine. Cette thèse rend compte de la réalisation, pour la première fois, des lasers de microtubes basés sur III-V, pompés optiquement et électriquement, ainsi que des photodétecteurs fonctionnant en longueur d'onde des télécommunications. En outre, nous présentons la réalisation du premier DEL en nanofils AIN émettant à 210 nm.

L'un des principaux avantages de ces structures de nanofils III-N par rapport à leurs homologues planaires est leur capacité à croître du cristal sans dislocation sur un substrat étranger.

Nous avons obtenu un effet laser dans la zone des longueurs d'onde des télécommunications à partir des dispositifs de tubes enroulés point/tiret (dot/dash) quantique InAs / InGaAsP en 80 k et dans la température ambiante avec des valeurs de seuil extrêmement bases de $\sim 1.2~\mu W$ et $\sim 6~\mu W$, respectivement.

Nous avons également signalé des dispositifs de tubes photodétecteurs enroulés point (dot) quantique InAs / InGaAsP dans lesquels la longueur d'absorption de la lumière et le transport du support de la charge peuvent être optimisés séparément.

Dans la température ambiante, les dispositifs montrent une sensibilité de $\sim 0,066$ A / W à 1064 nm, avec un rendement quantique externe de $\sim 8\%$.

En optimisant la conception et la fabrication, nous avons, pour la première fois, démontré les lasers de tubes enroulés en puits quantiques InGaAs / InGaAsP électriquement injectés fonctionnant à $\sim 1,5$ µm. Ces dispositifs présentent un seuil de $\sim 1,05$ mA à 80 K. Cela ouvre la voie à la mise en œuvre pratique de ces cavités optiques tubulaires dans les systèmes de communication optique au niveau de la puce.

En outre, nous avons obtenu le premier AIN UV p-i-n DEL en base du nanofil émettant à ~ 210 nm. Ces dispositifs présentent une tension d'allumage de ~ 6 V et une basse tension de fonctionnement (8 V à 20 mA). Nous avons également étudié la caractérisation optique et le traitement d'un nouveau polymère à utiliser comme matière de passivation pour la fabrication des DELs nanofils UV.

Acknowledgement

First of all, I would like to thank my parents for their love and support throughout my life. I wish to express my sincere gratitude and appreciation to my advisor, Dr. Zetian Mi for his remarkable guidance, support and encouragement during my PhD studies. I would also like to thank my committee members, Dr. Vamsy Chodavarapu and Dr. Nathaniel Quitoriano for their valuable assessments and suggestions during the examination of the work. I would like to thank Prof. Pablo Bianucci for great discussions and to get me acquainted with device processing and characterization. I am thankful to Dr. Phillip Poole for epitaxial growth of the material and Dr. Shmasul Arafin for valuable suggestions and discussions. I would like to also express my gratitude to McGill nanotools microfab members including Dr. Matthieu Nannini, Donald Berry, Jun Lee and Dr. Lino Eugene for their technical training and fruitful discussions. I am very much grateful to my past and current research group members including Mehrdad Djavid, Dr. Qi Wang, Dr. Songrui Zhao, Binh Huy Le, Shouvik Mukherjee, Dr. Saeed Fathololoumi, Md Golam Kibria, Dr. Omid Salehzadeh, Dr. Hieu Pham Trung Nguyen, Dr. Kwai Hei Li, Xianhe Liu, Dr Yong-Ho Ra, Ashfiqua Connie, Bandar AlOtaibi, Shizhao Fan, Renjie Wang, Nhung Hong Tran, Sharif M. Sadaf and Junjie Kang. A special thanks to Dr. Afshin Moin for translating the abstract to French.

Finally, I would like to thank Natural Sciences and Engineering Research Council of Canada and U.S. Army Research Office for their financial support on this research.

Contribution of Authors

This dissertation work is enriched with the contribution of the candidate and other individuals. The candidate and his supervisor, Dr. Zetian Mi defined the projects and worked closely on discussions regarding the methodology and progress of the projects. The design and optimization of rolled-up microtube research work were done by the candidate and Dr. Zetian Mi with the help of Dr. Pablo Bianucci. The microtube device fabrication and characterization were done primarily by the candidate with some help from Dr. Shamsul Arafain and Shouvik Mukherjee. The molecular beam epitaxial growth of the InAs-InGaAsP quantum dot/dash material and UV nanowires were done by Dr. Phillip Poole and Dr. Songrui Zhao, respectively. The device simulation was done by Mehrdad Djavid. The candidate and Sharif Md. Sadaf contributed in the AlN NW LED device fabrication. The characterization of UV NW LEDs was performed by Ashfiqua Connie, Dr. Songrui Zhao and Dr. Qi Wang.

Chapter 1. Introduction

Next generation of telecommunications, computing and information processing systems requires low power, high speed and small device components [1]. These characteristics are critical for keeping up with the exponential reduction of feature sizes on electronics chips as ruled by Moore's law. Although electronics components are still essential for processing applications, the fundamental limitations of electrical interconnects are the roadblocks to achieve high densities of fast and low power on-chip device components [2-7]. A potential approach to address these issues is to use photons instead of electrons to transfer the information by employing optoelectronics devices and optical interconnects. The result is the hybrid integration of the electronic and optoelectronic passive and active components for which silicon (Si) is used as the platform.

In contrast to III-V materials, Si has an indirect bandgap and therefore cannot be used as the active material for light emitting devices such as LEDs and lasers. On the other hand, the micromachining and CMOS integration technology of Si is of low cost and very well advanced which makes it an interesting substrate material choice. Moreover, when used as the substrate material, Si provides a much more efficient heat sink for the integrated electronic and optoelectronic components due to the higher thermal conductivity of Si compared to III-V materials resulting in less heating effect issues. Therefore, the heterogeneous integration of compound III-Vs as the direct band gap, active material on silicon substrates is a promising solution which can take advantage the desirable characteristics of III-V semiconductors together with the already mature CMOS processing and integration.

In order to complete the integrated photonics toolbox, an on-chip, electrically-injected light source is needed. III-V based microcavity lasers are attractive candidates because of their small dimensions which allow higher integration densities, higher speed and less power consumption. For the goal of achieving emissions at the 1.55 μ m, i.e. the telecommunication wavelength, InP/InGaAsP material system would be a suitable choice. Among different types of III-V based microcavity light sources, we have studied the characteristics of a specific type, called rolled-up microtubes [8] in this thesis that

will be described in detail in the following sections. These III-V based tube devices can be readily transferred to other substrates including Si without the degradation of the device performance, which together with their unique characteristics defines them as promising candidates for integrated light sources / photodetectors in silicon photonics.

Also, in this thesis we have studied the fabrication and device passivation of UV LEDs based on III-nitride nanowires (AlN) that are grown on Si substrate using MBE. Group III-nitride compound semiconductors offer exceptional electrical and optical properties required in optoelectronic device applications thanks to their unique characteristics such as high electron mobility, large saturation velocity, good thermal conductivity and high breakdown electric field [9-11]. One of the great properties of the III-nitride semiconductor group materials is their direct bandgap energy that can absorb and emit light very efficiently over nearly the entire solar spectrum ranging from infrared (IR) range of ~ 0.65 eV (InN) to ultraviolet (UV) range of ~ 6.1 eV (AlN) [9, 11-14].

Compared to III-nitride planar structures, III-nitride nanowires offer the possibility of growing dislocation-free crystals on a foreign substrate and therefore are considered as promising candidates for optoelectronic devices such as LEDs and lasers. In this regard, we have discussed the device fabrication and device passivation challenges for AlN LEDs emitting at the DUV range (~ 210 nm).

The characteristics of optically-pumped InP/InGaAsP quantum dot/dash tube lasers at 80 K and room temperature, InAs/InGaAs quantum dot tube photodetectors, electrically injected InGaAs/InGaAsP quantum well lasers at 80 K and AlN UV nanowire LED device fabrication and passivation have been studied in this thesis.

In this chapter, advantages of optical interconnects and an introduction to rolled-up microtube devices followed by a review on some of the recent developments of microtube-based devices for different applications will be discussed. Subsequently the requirement for UV emitting sources and advantages of UV LEDs over conventional UV light sources will be discussed. A brief introduction to nanowire LEDs and their advantages compared to planar structures is also presented.

1.1 Optical Interconnects

Optical interconnects have become the interesting alternative to electrical interconnects for long distance as well as chip-level communications mainly because electrical interconnects do not meet the requirements for high data rates [15-18]. Recently, as the consequence of shrinking down the electronic components to reach higher integration densities, fundamental limitations of electrical interconnects have become an issue. Electrical interconnects have a resistive frequency dependent loss that will be even more problematic at very long distances. Because of the interline capacitances, electrical interconnects also suffer from cross talk related issues. On the other hand, very short carrier wavelengths of optical signals (on the order of $\sim 1\text{-}1.5~\mu\text{m}$ or less) make it possible for them to use dielectric waveguides which can have very low resistive loss compared to conventional copper cables by avoiding the metallic waveguide that is required for the confinement of radio-frequency waves associated with electrical interconnects [15, 19] . The amount of bit rate for electrical interconnects is limited to a value relative to their physical dimensions, i.e. cross section area and the length of the wires:

$$B < B_0(\frac{A}{L^2}) \tag{1.1}$$

where A and L are the cross section area and the length of the wires, respectively and B_0 is $\sim 10^{16}$ (b/s) for typical resistive-capacitive lines on chip. Such a limitation on bit rate does not apply to optical systems. Thus, photonic information processing can, in principle, be faster and require less energy [15, 16, 20, 21]. Although the use of optical interconnects for long distance communication has already become dominant by employing optical fibers, their dominance on shorter communication distances, namely between chips or on chip has not yet occurred. This, to a large extent is due to the lack of essential optoelectronics devices, including light sources, that are compatible with the low cost CMOS technology. Due to the large dimensions of conventional lasers as well as the materials incompatibility with Si, the achievement of highly reliable and densely integrated lasers on a CMOS chip has not been possible. Drastically different laser technologies are therefore urgently required. In this regard, low threshold, ultrahigh speed micro- and nanoscale lasers that can be directly integrated with optoelectronic and

electronic components on a CMOS chip are in demand for future chip-level optical communications. Among the various semiconductor micro- and nanoscale optical cavities that have been investigated, rolled-up semiconductor tube cavities present unique characteristics as discussed in detail in the following sections.

1.2 Rolled-up Microtubes

As mentioned previously, in order to achieve a low threshold micro- or nanoscale laser that can be integrated on a Si platform, different varieties of microcavities have been studied over the years. Among them are photonic crystals [22], InGaAs nanopilars [23], micro-rings [24], micro-disks [25], and GaAs/InAs quantum dot rolled up microtubes [26]. Integration difficulties associated with nanowires, etching process-induced surface roughness of micro-disk and rings and the resulting high optical loss, and extensive use of electron beam lithography for the fabrication of photonic crystals, make the rolled-up microtubes a more desirable option for the purpose of fabricating microcavity lasers. Another advantage of microtube devices over other microcavity structures is the relatively straight-forward fabrication processing of these devices, as discussed in the following section. They also exhibit directional emission and polarization control and can be readily transferred onto Si substrate.

1.2.1 Fabrication Principles of Rolled-up Semiconductor Tubes

The formation of rolled-up microtubes, first discovered by Prinz [8] and collaborators in 2000 in the GaAs/InGaAs system, is based on the release of strain in nanomembranes. Figure 1.1 shows a schematic of an InAs/GaAs membrane and the related tube formation process. Since GaAs has a smaller lattice constant than InAs, the GaAs layer is tensile-strained after its pseudomorphic deposition on top of the InAs. Rolled-up tubes are formed because of the strain relaxation in the membrane when it is released from the substrate. As a consequence, the curvature of the rolled-up tube can be controlled by adjusting the built-in strain in the bilayer and the respective thicknesses of its constituent membranes. With the use of a continuum mechanics model [27], it is possible to predict the diameter of the resulting microtube with the following formula,

$$D = \frac{1}{3} \frac{1}{\varepsilon} \frac{(d_1 + d_2)^3}{d_1 d_2} \tag{1.2}$$

where ε is the in-plane strain, and d_1 and d_2 are the thicknesses of the layers. In general, tubes prepared with optical applications in mind may have diameters on the order of several μ m, although tubes with diameters as small as tens of nanometers have been demonstrated [28]:

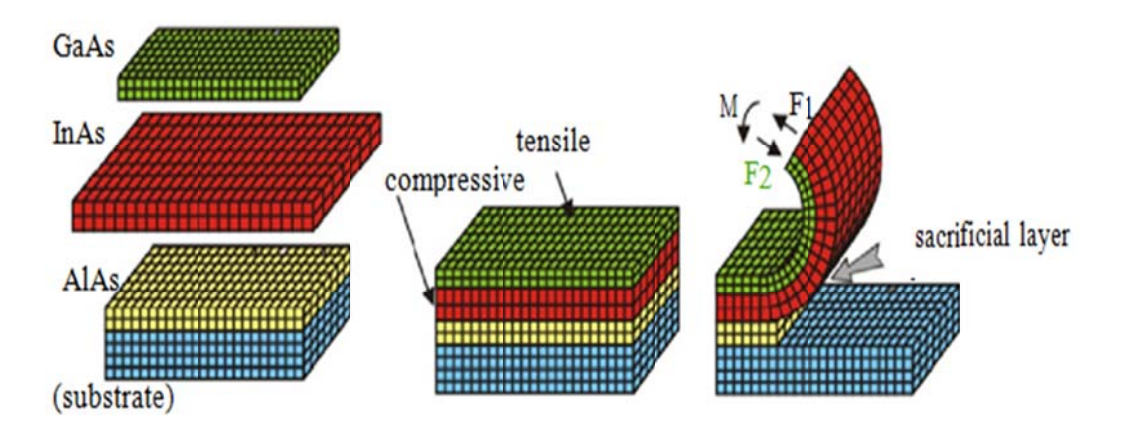


Figure 1.1 Illustration of the rolling mechanism for a strained InAs/GaAs bilayer membrane [29]

The tube rolling generally takes place along the [100] crystal direction in this system, because of the anisotropy of the Young's modulus in this kind of crystals [30]. Not only can the tube diameter be controlled, but also its final surface geometry. This can be achieved by patterning the nanomembrane [31, 32]. For instance, when patterned in the shape of high aspect ratio rectangles, the membrane will roll along its short side. For rectangles with a lower aspect ratio, the rolling occurs preferentially along the long side [31]. In addition, the starting rolling edge and resulting geometry can be altered by external means such as pinning the membrane with photoresist [33]. The semiconductor tube fabrication combines the top-down and bottom-up approaches. Starting from a strained nanomembrane, standard photolithography and top-down etching processes are used to define a starting edge for the rolling process. In crystalline materials, the associated mesas need to have the proper crystallographic alignment for controlled rolling to occur (for instance, along the aforementioned [100] axis in crystalline semiconductor III-V systems [31]). To realize free-standing tube cavities, a U-shaped

mesa is commonly employed as shown in Fig. 1.2(a). In this scheme, both the thickness of the free-standing tube and the vertical separation from the substrate can be entirely controlled by the shape of the mesa. The tubes will then self-assemble (in a bottom-up fashion) by means of a sacrificial etching process as seen in Fig. 1.2 (b). As shown in Fig. 1.1 for InGaAs/GaAs nanomembranes, the AlAs layer is the sacrificial layer [32, 34]. In the case of InP/InGaAsP material system, the strained bilayer is composed of two layers of In_xGa_{1-x}As_yP_{1-y} with different compositions lattice matched to InP substrate. In this material system, the InP substrate itself plays the role of sacrificial layer due to the possibility of selective etching. GaAs and InP-based microtubes have a diameter of between 5-7 μm with 50-150 nm wall thickness and about 100 μm length as seen in Fig. 1.2(c).

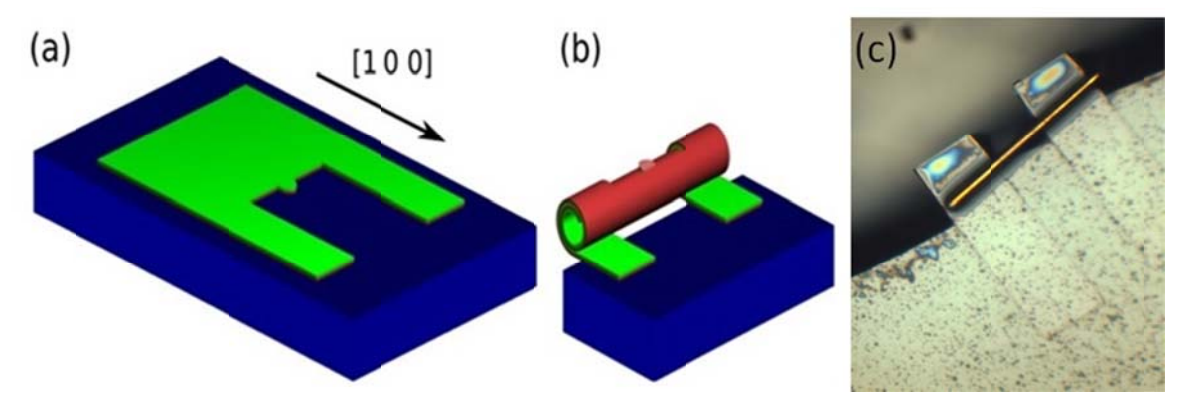


Figure 1.2 Illustration of the fabrication of free-standing semiconductor tube optical cavities. (a) Lithographically defined U-shaped mesa. (b) Rolled-up tube resulting from the sacrificial etching and release of the U-shaped mesa. (c) Optical microscopy image of a rolled-up InGaAsP tube.

There have also been many reports on the fabrication of rolled-up tube structures using metal and dielectric membranes. For example, strain driven SiO_x/Si tubes which show PL in the NIR range, have been demonstrated [35]. Polymer tubes fabricated using deposited or electrospun polymers have also been reported [36-38]. Single and bimetallic (Au,Ti) tubes have been fabricated from self-rolled polymer templates [39]. Combining different kinds of materials, hybrid rolled-up tubes have been reported such as InGaAs/GaAs/Au and InGaAs/GaAs/Nb [40] metallized tubes, and InGaAs/GaAs/polymer hybrid organic-semiconductor tubes [41].

1.2.2 Transfer of Rolled-Up Tube Structures

To take advantage of the already mature silicon CMOS technology and simultaneously benefit from the III-V semiconductor characteristics such as direct bandgap and high carrier mobility, it is necessary to use a proper technique to transfer the active III-V devices onto silicon substrates. Although special techniques such as wafer bonding [42, 43] and dry-printing [44-46] have been developed, it is not possible to use them for rolled-up microtubes as they tend to break during the transfer process. In this regard, certain methods have been demonstrated to effectively transfer the microtubes. In the recently reported substrate-on-substrate transfer process [47], the host substrate (GaAs wafer), with the presence of free-standing InGaAs/GaAs tubes, is pressed on top of a silicon wafer in the presence of a solvent. By removing the GaAs substrate, the tubes preferentially stay on the Si substrate due to the gravitational force induced by the solvent around the tube structure. Thanks to surface tension forces, the tubes are subsequently attached to the Si substrate. Alternatively, rolled-up tube structures can also be transferred on foreign substrates by first dispersing them in a solvent solution which is then drop-cast on the substrate [28]. A unique fibre-taper assisted transfer process has been developed to achieve precise control over the transfer process [48]. In this approach, abruptly tapered optical fibers are inserted at one or both ends of the tube structure and are used as a handle to pick up the tube from its host substrate. The transfer process is schematically illustrated in Fig. 1.3. Subsequently, the tube can be transferred to a foreign substrate with precise positioning, compared to other transfer processes. Using this transfer technique, direct integration of rolled-up optical tube cavities with silicon-oninsulator waveguides has been demonstrated [49].

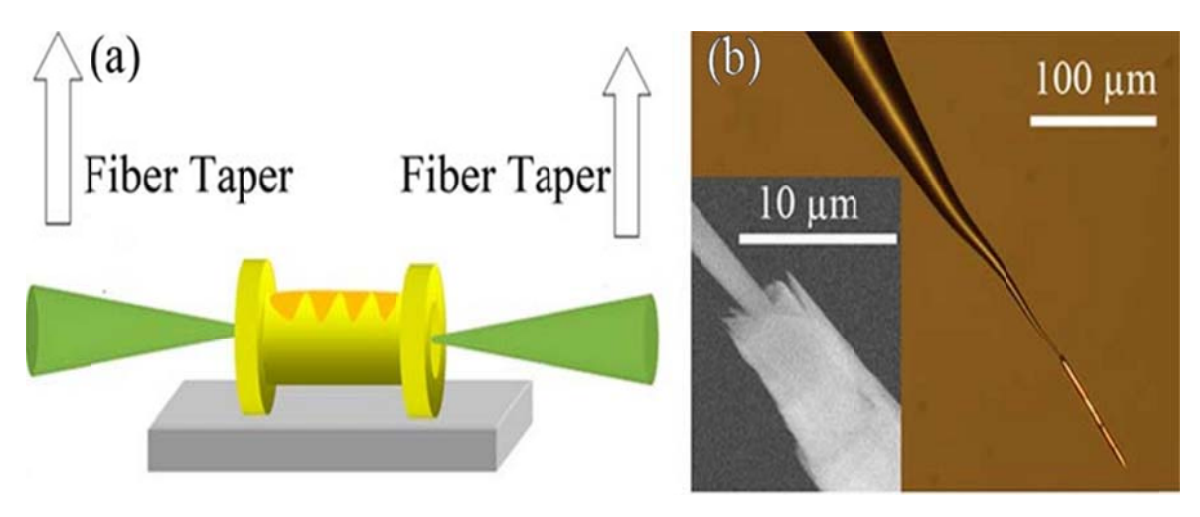


Figure 1.3 (a) Schematic illustration of the transfer method with the use of abruptly tapered optical fibers. (b) Optical microscopy image of a semiconductor tube on the tip of an abrupt fiber taper. Inset: Scanning electron microscopy image of the transition between the glass fiber and the tube [50].

1.2.3 Optical Characteristics and Control of the Optical Resonance Modes

With the formation of rolled-up semiconductor tubes, improvement in the optical properties, such as enhancement in the photoluminescence intensity of the quantum wells or dots embedded in the tube structure, has been commonly observed [51-53]. Coupling between the photoluminescence emission and the cavity resonant modes can lead to regularly spaced emission peaks for these cavities. Consequently, their optical properties are highly tunable by changing their diameters, wall thicknesses and surface geometry [34, 54]. These parameters can be easily determined by controlling the material growth process and a simple, high-throughput, optical lithographically step. They also show well defined polarized and directional emission and can have cold-cavity Q-factors in the order of 10⁵ [8, 26, 32, 54-56]. By using MBE or CBE growth techniques, these devices have a very smooth surface leading to less loss. Additionally, compared to conventional optical cavities with a circular cross-section, such as microrings [24], microdisks [25] and microspheres [57], rolled-up tube cavities exhibit spiral symmetry due to the presence of inside and outside notches, illustrated in Fig. 1.4(a), which break the degeneracy of optical modes propagating in clockwise and counterclockwise directions [58]. It has also been observed that rolled-up semiconductor tubes with relatively thin walls can only

support transverse electric (TE) modes, with the electric field polarized along the tube surface [59].

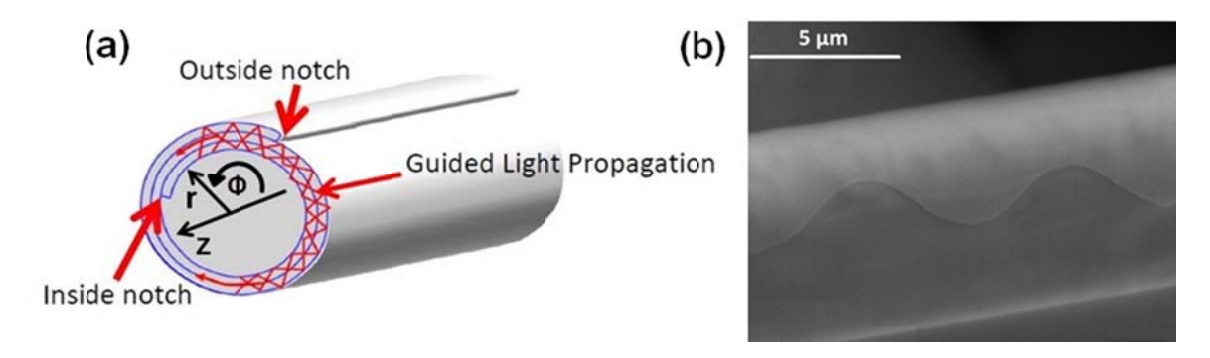


Figure 1.4 (a) Illustration of the spiral geometry of a rolled-up tube, showing the presence of inner and outer notches. (b) SEM image of the free-standing part of a tube device showing the presence of surface corrugations for axial mode confinement.

The azimuthal confinement of the optical modes in the tubular structures is due to the ring resonator nature of the tubes, in which the microtube wall acts as a waveguide for the light due to total internal reflections as seen from Fig 1.4 (a). This results in constructive interference of the guided light if the phase of the guided wave matches after one roundtrip. Compared to other optical microresonators, emission characteristics of rolled-up tube cavities can be readily tailored during the device fabrication process. First, the layered structures that form the tubes can be engineered to determine the tube diameters (see Equation 1.2). The diameter, as is the case with regular ring resonators, will largely determine the free spectral range (the spectral separation between consecutive azimuthal modes) according to:

$$FSR \approx \frac{\lambda^2}{\pi nD} \tag{1.3}$$

where λ is the resonant wavelength, n is the effective refractive index and D is the microtube's diameter. Thus the basic resonance mode characteristics can be determined, to a large extent, during the materials growth/synthesis process. The other important parameter that can be varied is the wall thickness, which is specified using lithography and is related to the number of windings that will form the rolled-up tube. The wall

thickness affects the radial mode properties, as well as the polarization of the confined photons.

Additionally, the axial mode profile of the tube cavity can be tailored by changing the profile of the averaged refractive index along the tube axis as seen in Fig 1.4(b). This is also schematically shown in Fig. 1.2 (a). The axial index profile can be controllably varied by defining a pattern around the inner or outer edge of the mesa during the device fabrication process. Properly designed patterns will induce confinement along the axial direction that can lead to three-dimensionally confined optical modes. Careful tuning of the pattern offers detailed control of the separation between these axial modes. As an example, the emission spectra for two InGaAsP/InAs quantum dot tubes simultaneously fabricated from the same starting bilayer are shown in Fig. 1.5. Shown in Fig. 1.5 (a) and (b) are the spectra measured for a 2-turn and 1-turn tube, with an average wall thickness of ~100 and 50 nm, respectively. The associated azimuthal (m) and axial (p) mode numbers are identified [34]. The spacing between consecutive azimuthal modes is ~27 meV, consistent with a tube diameter of ~5 μ m. It is seen that for the two-turn tube, the linewidth is much narrower (~0.9 meV), compared to that (~3 meV) of the 1-turn tube, due to the enhanced optical confinement associated with the increased wall thickness.

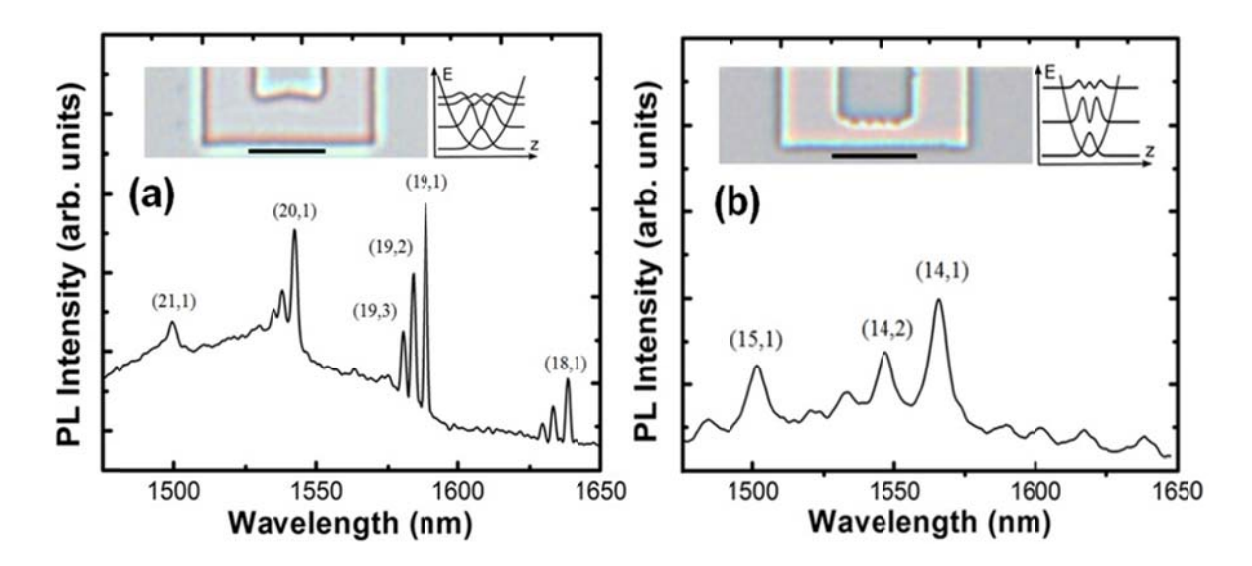


Figure 1.5 (a) Photoluminescence spectrum of a microtube with an average wall thickness of ~ 100 nm. The corresponding mode numbers are identified. Shown in the inset are the optical microscopy image of the lithographically defined U-shaped mesa and schematic of the electric field of the first few axial modes. (b) Photoluminescence spectrum of a microtube with a wall thickness of ~ 50 nm shown with the corresponding mode numbers. Shown in the inset are the optical microscopy image of the U-shaped mesa and schematic of the electric field of the first few axial modes. The scale bar corresponds to a length of 50 μ m in both (a) and (b) [60].

Additionally, it is observed that the axial modes can be controlled by varying the tube surface geometry. The shapes of the inner edge of the lithographically defined mesas are illustrated in the insets of Fig. 1.5(a) and (b) for the 2-turn and 1-turn tube cavities, respectively. The surface corrugations of the 2-turn and 1-turn devices exhibit correspondingly low and high curvatures. The resulting weak and strong axial optical confinements, schematically shown in the right insets in Fig. 1.5(a) and (b), yield relatively small (~2.3 meV) and large (~9.5 meV) energy spacing between adjacent axial modes for the 2-turn and 1-turn tube devices, respectively. It is therefore evident that the three-dimensionally confined optical modes can be tailored by varying the tube diameter, wall thickness and surface geometry using a simple, high-throughput, optical lithographical step.

1.3 FDTD Analysis of Rolled-up Tubes and the Dielectric Planar Waveguide Model

FDTD is one of the most important methods to compute resonant mode wavelengths and field distributions [61]. Throughout this thesis, our FDTD simulations are restricted to two dimensions where we compute the spectra and fields for the cross-section of a rolled-up tube. Although this simplified approach only considers in-plane wavevectors and therefore does not show the axial behavior of the modes, other features of tubular structures can be assessed. For instance, it allows identification of azimuthal modes and their corresponding mode numbers. Figure 1.6 shows an example of such computations for a tube cavity. Figure 1.6 (a) shows a mode spectrum calculated by using a broadband dipole source. A strong mode near 1425 nm was selected and a narrow band dipole source at that wavelength excited that mode. After the build-up of the mode a snapshot of the electric filed intensity was captured as shown in Fig. 1.6 (b). It is interesting to notice that the emission occurs preferentially from the inner rolling edge of the tube rather than being isotropic as is the case for an ideal ring resonator [54, 58], which leads to directional emission of rolled-up tube structures.

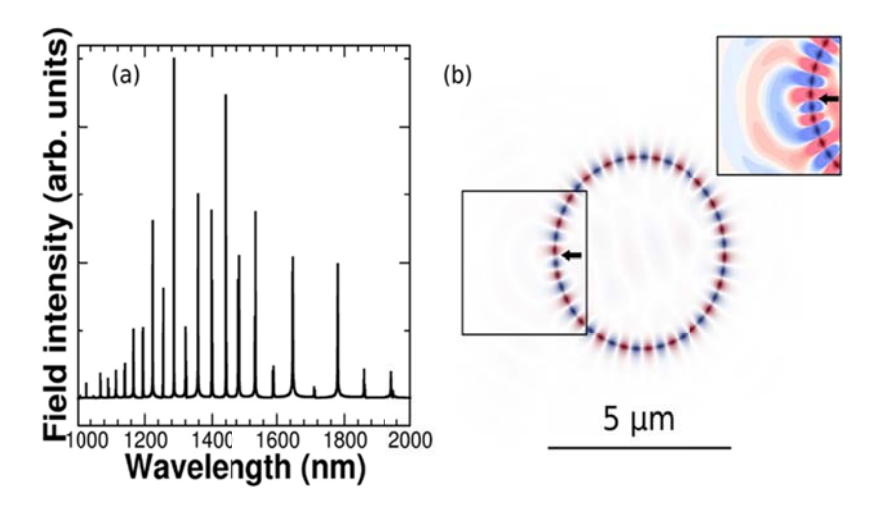


Figure 1.6 (a) Calculated resonance mode distribution of a tube cavity using a twodimensional finite-difference time-domain algorithm. (b) Calculated electric field distribution, plotted using a linear color scale to emphasize the field confinement. The black arrow marks the position of the inner rolling edge. Inset: Detail of the marked square, using a modified color scale to emphasize the directional emission pattern [50].

Due to the spiral symmetry of the microtube, it cannot be simply approximated as a twodimensional ring resonator. Moreover, the axial mode confinement in the microtube structure is provided by surface corrugations that are introduced during the fabrication processing. One useful model to calculate the axial modes of a micrtoube structure is a dielectric planar waveguide model which considers the microtube as an effective planar slab waveguide. As seen in Fig. 1.7, upon rolling, the tube consists of two different wall thicknesses. Therefore, the effective planar waveguide is composed of two slabs with different thicknesses and a step and can be analyzed using a straight forward method. For a tube with a diameter R, at any given z position the equivalent waveguide is composed of two parts with L_{thick} and L_{thin} so that L_{thick} + L_{thin} = $2\pi R$. The effective indices of the two different thicknesses are n_{thick} and n_{thin} which can be computed using the well-known solutions for planar slab waveguides. We then consider an average effective index of $n_{circ}(z) = L_{thick}(z)n_{thick} + L_{thin}(z)n_{thin}$ for a two-dimensional planar waveguide. Since the polarization of the emission in microtubes with thin walls is predominantly along the tube wall (the z axis), we can analyze the modes by applying the scalar Helmholtz equation to the waveguide:

$$\frac{-1}{n_{circ(z)}^2} \left(\frac{d^2}{dz^2} E(l, z) + \frac{d^2}{dl^2} E(l, z) \right) = k^2 E(l, z)$$
 (1.4)

Where E(l,z) is the electric field and k is the vacuum wavevector. By assuming separation of variables we can substitute $E(l,z) = \Phi(z) \exp(i\beta l)$ and by considering the azimuthal resonance condition of $\beta R = m$ we obtain:

$$-\frac{\partial^2 \Phi}{\partial z^2}(z) - n_{circ}(z^2) K^2 \Phi(z) = -\beta^2 \Phi(z)$$
 (1.5)

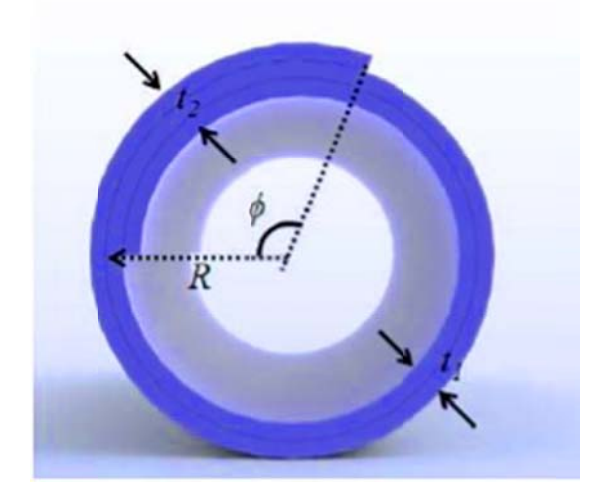


Figure 1.7 Cross-section of a tube structure showing different wall thicknesses with inner and outer notches in the structure

Which is similar to Schrödinger equation and therefore called "photonic quasi-Schrödinger equation". Each solution to the equation (1.5) corresponds to a different axial mode. Therefore, by changing the shape of the surface corrugations we can change the spectrum of axial modes as experimentally demonstrated [54].

1.4 Recent Developments of Microtube-Based Devices

A brief overview is provided in this section for the recent developments of microtube-based devices for biosensors, chip-level optical communications, and other applications.

1.4.1 Biosensors

The fabrication flexibility of rolled-up tubes makes it possible to create optical resonators with sub-wavelength wall thicknesses, leading to a highly enhanced evanescent field. As a consequence, the resonant modes in the device are ultrasensitive to optical perturbations outside its walls (to a distance determined by the exponential decay of this evanescent field, usually on the order of several hundred nanometers), thereby promising optical sensing devices capable of detecting minute changes in the refractive index of their environment. Ma *et al.* have demonstrated the detection of dynamical molecular processes using a whispering gallery mode microtube sensor, by which the quantitative

information of molecule layer changes on the tube surface were acquired by measuring the changes in the position of the resonant mode of the tubular cavity [62]. Huang *et al.* has demonstrated this concept by measuring the changes in the emission spectrum of SiO/SiO₂ microtubes as a function of their environment. Measurements taken in air, ethanol, water, and a mixture of the last two showed a shift of the resonant mode wavelengths to the red, as well as a broadening of the mode peaks, when the medium refractive index was increased [50, 63]. The hollow structure of the tube devices makes them suitable to be used together with microfluidics, wherein the liquid to be sensed can flow through the hollow channel of the rolled-up tube device, providing an interesting possibility for realizing an integrated tube-based microfluidic sensing system [50, 64-67].

1.4.2 Optical Communications

Previously the advantages of rolled-up microtube devices including their small dimensions, tenability, ease of fabrication, directional emission and direct transfer on foreign substrates were described, which define them as promising candidates for an integrated light source for chip-level optical communications [34]. Zhong *et al.* have demonstrated coupling modulation by thermally tuning the coupling gap between a rolled-up micotube and the silicon waveguide which facilitates optical switching and modulations of microtubes on photonics integrated circuits [68]. Bhowmick *et al.* have shown an optoelectronic integrated circuit using microtubes both as light source and photodetector [69]. Rolled-up tube devices have also been shown to function as add-drop filters [49, 70], directional couplers [71] and photodetectors [72].

1.4.3 Other Applications

Apart from their optical applications, rolled-up tubes have been employed in numerous other promising applications. For example, it is possible to fabricate rolled-up tube capacitors by using a set of strained layers in a conductor-dielectric-conductor configuration. Ji *et al.* have demonstrated a RuO₂ microtube supercapacitor with 7 μ m diameter and 1.0 μ F capacitance [73]. Compared to commercial capacitors, these results have shown a considerable reduction in size of about two orders of magnitude. In another example, Sharma *et al.* have shown more than 100% of increase in capacitance compared

to their planar counterparts by employing high-k oxides such as HfO₂ and TiO₂ and also effectively decrease the occupied device footprint [74]. Rolled-up tubes have also been used in bio-related studies. For instance, Xi *et al.* have encapsulated single living cells into transparent SiO/SiO₂ tubular nanomembranes and have shown that spatial confinement of mitotic cells inside tubular architectures could provide important clues into how spatial constraints dictate cellular behavior and function [75]. Huang *et al.* have shown on-chip inductors using SiN_x microtubes that can be used in radio frequency integrated circuits [76]. Tube structures have also been used as scaffolding for the growth of cells [77] where a biocompatible-based rolled-up tube has been employed to guide the growth of yeast cells and study their behavior in confined environments.

In another very interesting development, Solovev et al. have demonstrated a catalytic microjet engine [78] in which the tube structure is designed in such a way that it is slightly tapered with its inside surface including a catalytic platinum film. When the tube is placed in the hydrogen peroxide solution, the catalytic action of the platinum decomposes the peroxide in water and oxygen, forming a microbubble which moves towards the end of the tube and exits. This will move the tube forward in the fluid causing the fresh peroxide to enter and maintain the motion.

1.5 Ultraviolet LEDs

There is a huge demand for UV light emitting devices for a great number of applications such as medical instrumentation, disinfection and sterilization, water purification and biological sensors. However, there are a number of drawbacks associated with currently dominant Xenon and mercury lamps. These UV sources are bulky and expensive and are very inefficient considering their short lifetime and high voltage operation. Moreover, their operating wavelengths are not tunable and they are considered as environmentally hazardous due to the presence of mercury [79]. On the other hand, LEDs are much more efficient regarding their lifetime and operating voltage. They are also smaller, cheaper and free from such polluting materials. In addition, it is possible to tune the emission wavelengths of these semiconductor components by engineering their bandgaps ,and their market is expected to grow very rapidly within the near future [80, 81].

1.5.1 Nanowire LEDs

Despite their aforementioned unique electrical and optical properties, III-nitride planar structures exhibit high dislocation densities resulting in poor device performance due to the lack of native substrates. On the other hand, nanowires can be grown vertically and have diameters in submicron range and therefore they show lateral strain relaxation, leading to drastically reduced dislocation densities when grown on foreign substrates. Si, Sapphire and SiC are the commonly used substrates for III-N materials growth [82]. However, all of these substrates have large mismatches in lattice constants and thermal conductivities which are critical parameters during growth. Epitaxially grown lattice mismatched layers undergo tensile or compressive strain. When the layers grow to above a critical thickness, on the order of a few nanometers or less, dislocations start to be generated within the structure. The dislocation density of GaN grown on these substrates is typically in the range of $10^8 \sim 10^{10}$ cm⁻² [83-85]. These dislocations will become nonradiative recombination centers as they introduce new electronic states in the bandgap. leading to severe degradation in the electrical and optical performance of the devices. Additionally, strain can cause piezoelectric polarization, considerably degrading the LED performance. In this respect and in direct contrast to planar structures, the MBE grown nanowire structures with small diameters, offer lateral stress relaxation [86]. This, in turn, results in increased critical thickness in the case of nanowires [87] and therefore the crystal quality is much higher compared to planar structures. The strain relaxation process in thin film and nanowire structure is schematically shown in Fig. 1.8.

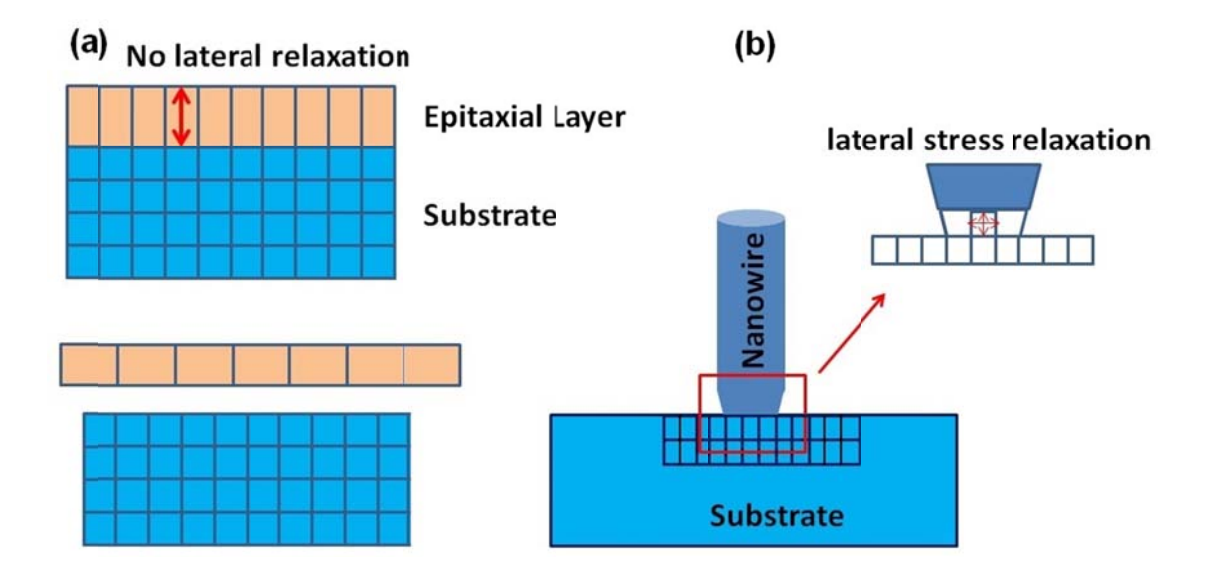


Figure 1.8 The epitaxial growth of (a) epilayer, and (b) nanowire structure. Due to the lattice mismatched substrate, the epilayer experiences severe strain. However, due to the lateral stress relaxation, stress is properly accommodated in nanowire structure.

It is difficult to have high performance planar UV LEDs especially in the DUP range. This is mainly due to low crystal quality as a result of lack of suitable substrate, difficulties in impurity doping due to high activation energy of Mg and also light extraction issues. On the other hand AlN nanowires offer significantly improved properties due to drastically reduced densities of defects and dislocations. Also due to the reduced formation energy of substitutional doping in the near surface region of the nanowires, they offer enhanced surface doping and conductivity [88]. Also in the case of planar LEDs, light extraction is strongly limited by the total internal reflection due to the difference in the refractive index of the semiconductor material and air. On the other hand, nanowire structures offer low effective index resulting in reduction in total internal reflection. They also exhibit high surface-to-volume ratio which provides more area for the photons to be extracted.

1.6 Organization of the Thesis

This thesis is focused on development of III-V based rolled-up microtube optoelectronic devices, namely lasers and photodetectors and their integration on Si platforms, suitable for future practical chip-level optical communication systems. Moreover, results and fabrication challenges of ongoing studies of III-N nanowire structures with emission in

the deep UV range of the spectrum are also presented. The first demonstrations of optically-pumped InP/InGaAsP quantum dot/dash tube lasers, InAs/InGaAs quantum dot tube photodetectors, electrically injected InGaAs/InGaAsP quantum well lasers, and AlN UV nanowire LEDs emitting at deep UV (210 nm) are presented in this thesis.

Chapter 1 provides an overview of optical interconnects and their advantages over electrical interconnects for future optical communications. A detailed introduction on different aspects of rolled-up microtubes as an important class of microcavity structures with unique characteristics suitable for integrated photonic devices in optical communication systems, together with a review on recent developments of microtube-based devices for different applications are also presented in this chapter. The need for UV emitting light sources and suitable properties of III-N semiconductors for such applications together with the introduction of nanowires and their advantages over planar structures is also discussed in this chapter.

In chapter 2, the design, fabrication and optical performance of InP-based InAs/InGaAsP quantum dot/dash tube laser devices, with emission wavelengths at $\sim 1.5 \mu m$ measured at low temperature and room temperature are described in detail.

Chapter 3 is related to the design, fabrication and characterization of novel GaAs-based rolled-up InAs quantum dot tube infrared photodetectors.

In Chapter 4, we have investigated the design, fabrication and characterization of electrically injected InP/InGaAsP rolled-up tube light sources wherein multiple InGaAs quantum wells are incorporated as the gain media. We have further demonstrated lasing from such devices, for the first time, defining them as practical candidates for on-chip optical light sources.

In Chapter 5, the fabrication procedure and electrical characterization of the first UV nanowire LEDs emitting at 210 nm are discussed. Such devices show much better performance compared to their planar counterparts. Also a new synthetic polymer material for the passivation of nanowire UV LEDs is introduced, and the processing and optical characterization of the material is presented.

Finally, summary of this thesis and a guideline to future works are discussed in Chapter 6.

Chapter 2. Optically-Pumped Quantum Dot/Dash Tube Lasers at Telecom Wavelength

2.1 Introduction

In order to achieve ultralow threshold nanoscale lasers, self-organized quantum dots and quantum wells have been incorporated in such tubular cavities as the gain media [26, 34, 51, 89] with lasing under optical pumping being demonstrated at room-temperature[26, 90] and 4 K[32], respectively. Due to the superior 3-dimensional carrier confinement and the discrete density of states, self-organized quantum dot lasers can exhibit significantly reduced threshold and improved temperature stability, compared to quantum well or nanowire devices [91]. In addition, their large differential gain enables higher modulation frequencies for ultrahigh speed applications. In this chapter the design, fabrication and optical performance of InP-based InAs/InGaAsP quantum dot tube laser devices, with emission wavelengths at ~1.5 µm measured at low temperature are described in detail. Such tubular optical cavities are formed when coherently strained quantum dot/dash nanomembrane is selectively released from the host substrate. Subsequently, the enhanced fabrication technique resulting in much higher device fabrication yield is presented leading to quantum dash tube laser devices operating at room temperature. The lasing wavelength of 1.59 µm was reported for the InAs quantum dash tube lasers operating at room temperature.

2.2 InAs/InGaAsP Quantum Dot Tube Lasers at 80 K

In what follows, the design, fabrication and characterization of InAs/InGaAsP quantum dot rolled-up tube lasers are presented and discussed in detail.

2.2.1 Device Design and Fabrication Procedure

Device fabrication commences with the growth by CBE of appropriately strained nanomembranes. Illustrated in Fig. 2.1(a), coherently strained InGaAsP bilayers consisting of 38 nm $In_{0.81}Ga_{0.19}As_{0.41}P_{0.59}$ and 15 nm $In_{0.68}Ga_{0.32}As_{0.41}P_{0.59}$ are first grown on an InP substrate. The top $In_{0.68}Ga_{0.32}As_{0.41}P_{0.59}$ layer is tensile-strained, while the

underlying $In_{0.81}Ga_{0.19}As_{0.41}P_{0.59}$ layer is lattice matched to the InP substrate. Two layers of self-organized InAs quantum dots, each with a density 3×10^{10} cm⁻² and separated by 12 nm, are incorporated in the $In_{0.81}Ga_{0.19}As_{0.41}P_{0.59}$ layer as the gain medium [92]. To realize free-standing tube cavities [54, 93], a U-shaped mesa (illustrated in Fig. 2.1(b)) is first defined by etching through the InGaAsP layers to the InP substrate using a 1:2:1 solution of concentrated (37%) hydrochloric acid, concentrated (70%) nitric acid, and deionized water. Subsequently, with selective etching of the underlying InP layer performed using an HCl:H₂O (2:1) solution, the strained mesa can be controllably released from the substrate. A layer of photoresist is used to cover the side pieces of the U-shaped mesa, illustrated in Fig. 2.1(b), so that the rolling process can take place only at the starting edge. The resulting quantum dot nanomembranes then roll-up into tube structures, with a reduced strain distribution.

The strain driven self-rolling process takes place preferentially along the [1 0 0] crystal direction, resulting in a tube-like structure, shown in Fig. 2.1(c). Since the substrate (as opposed to just a thin sacrificial layer, as discussed in section 1.2.1 [26, 32], is etched to release the membrane, the central part of the tube is well separated from the high index substrate to drastically reduce optical loss into the substrate. The wall thickness of the free-standing quantum dot tubes can be precisely controlled by the width of the strained mesa. Moreover, as described previously, the tube surface geometry can be engineered by varying the shape of the mesa, which provides an additional dimension for controlling the axial optical confinement, compared to conventional microring or microdisk resonators[54].

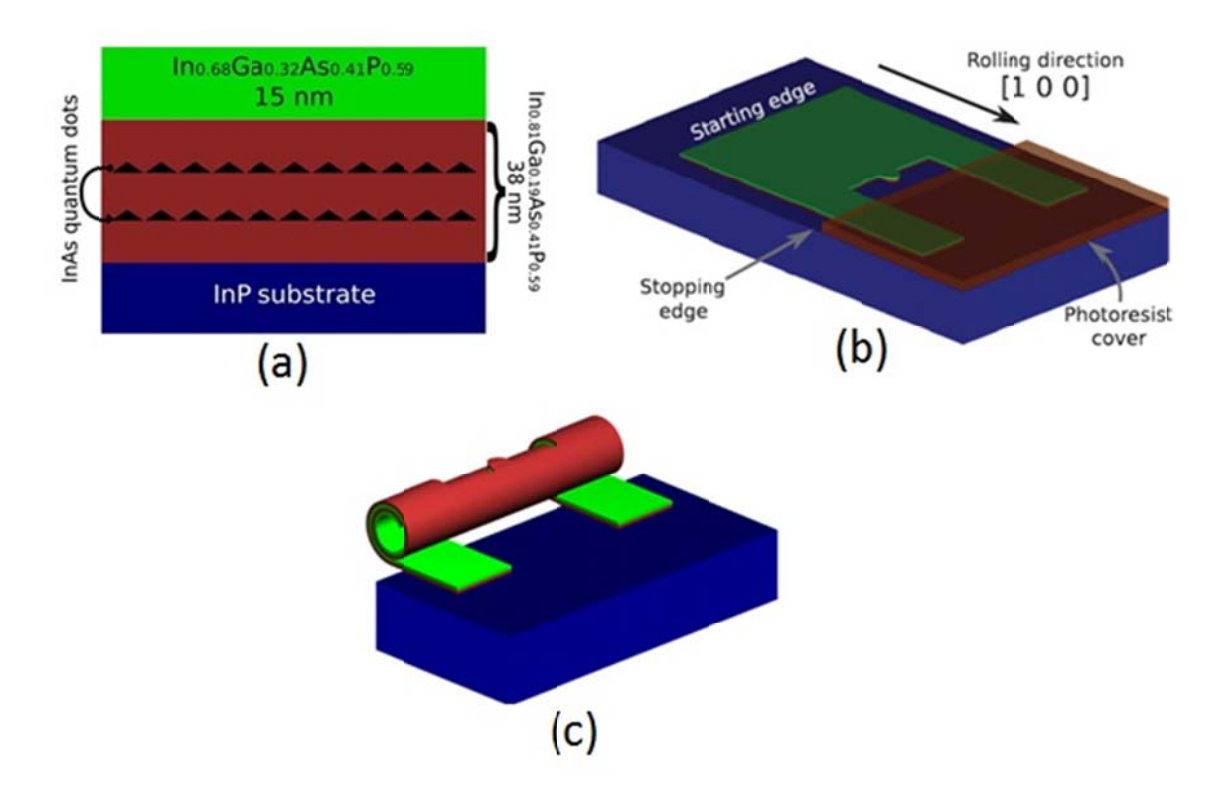


Figure 2.1 (a) Schematic illustration of InAs/InGaAsP quantum dot heterostructures grown on InP substrate. (b) Illustration of the U-shaped mesa defined to obtain free-standing tubes. The starting edge, rolling direction, and stopping edge defined by a photoresist layer are also shown. (c) Schematic illustration of a free-standing quantum dot tube structure.

An optical microscopy picture of a fabricated microtube with a length of $\sim 150~\mu m$ is illustrated in Fig. 2.2(a), clearly showing that the central part of the tube is free-standing. A scanning electron microscopy image of the surface corrugations of another tube device is shown in Fig. 2.2(b). In this study, we have focused on InAs/InGaAsP quantum dot tube devices with diameters between 5 and 7 μm , wall thicknesses between 50 and 100 nm, and varying parabolic-like surface geometries.

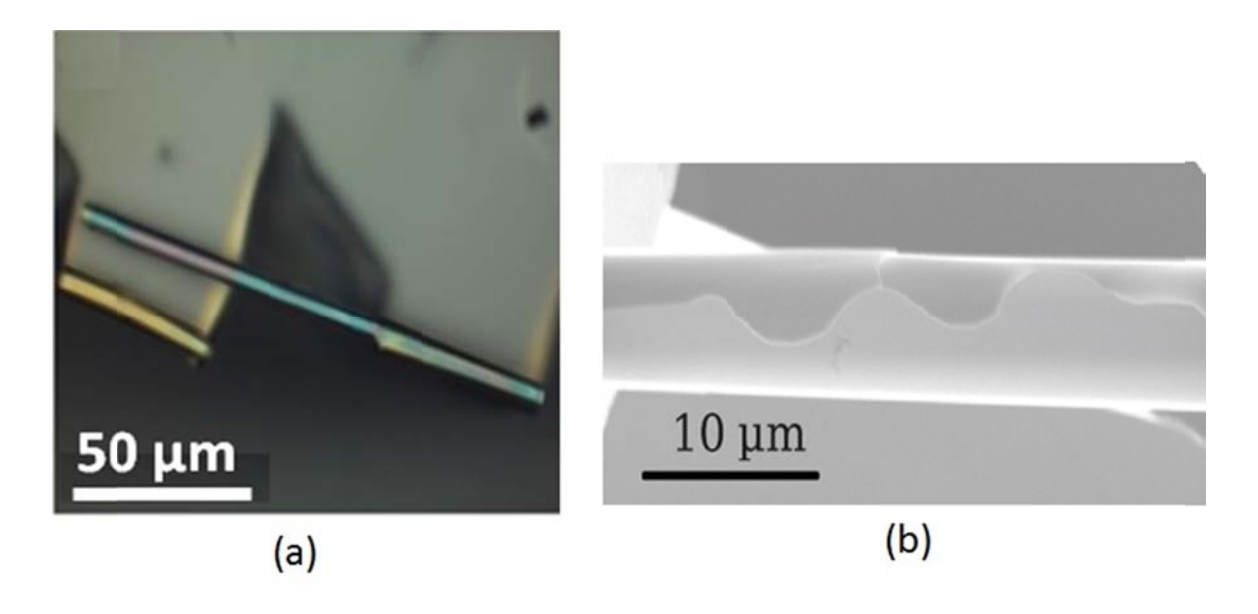


Figure 2.2 (a) Optical microscopy image of a rolled-up tube. (b) Scanning electron microscopy image showing a detailed view of the surface modifications [94].

2.2.2 Photoluminescence Studies and Discussions

The emission characteristics of rolled-up quantum dot tube cavities were studied using a variable temperature micro-photoluminescence system. The tube device was optically pumped using a 635 nm diode laser through a $100\times$ microscope objective (~ 0.70 NA) resulting in an excitation spot with a diameter of ~ 1 µm. The photoluminescence emitted by the sample was collected with the same objective and analyzed by a high-resolution spectrometer and a single-channel, liquid nitrogen cooled, InGaAs photodetector with lock-in amplification. The excitation power was measured before the microscope objective and then corrected for reflection losses in the microscope, cryostat window, and the microtube material itself.

The emission spectra measured at two different excitation powers ($\sim 0.18~\mu W$ and 5.8 μW) are shown in Fig. 2.3. Also shown in the figure, as a reference, is the photoluminescence spectrum measured from as-grown InAs/InGaAsP quantum dot heterostructures. Both tube spectra show clear mode structures, with very little background emission from the quantum dots, indicating a good coupling between the quantum dot photoluminescence emission and the optical modes. The associated azimuthal (m) and axial (p) mode numbers are identified by fitting the parameters of a planar waveguide model [33, 59] until the peak positions and spacing were reproduced.

The azimuthal mode properties are determined by the tube diameter and wall thickness. The spacing between consecutive azimuthal modes is 27 meV, consistent with a tube diameter of \sim 5 μm .

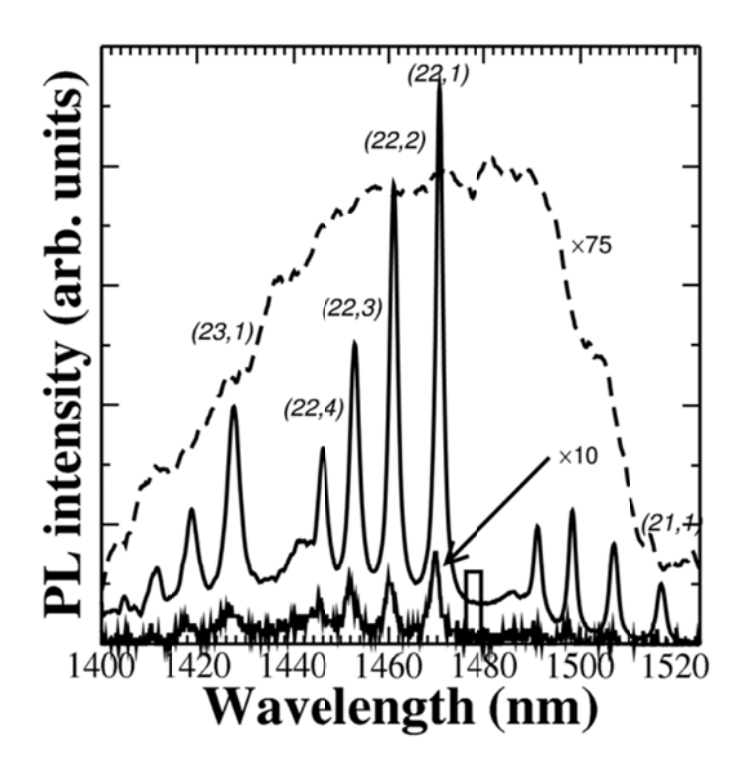


Figure 2.3 PL spectra of a tube device measured at 82 K. The lower (weaker) spectrum corresponds to a small incident pump power of 180 nW, while the upper (stronger) one was measured at a high incident pump power of $5.6~\mu W$. The lower intensity spectrum has been multiplied by 10 to improve its visibility. The dashed line represents the spectrum (multiplied 75 times, for better visibility) of an as-grown quantum dot heterostructure measured at the same temperature for reference [94].

We measured spectra at different pump excitation levels to study the power-dependent behavior. The emission peaks are further analyzed by fitting with Lorentzian functions. From this analysis, we extracted the integrated area and linewidth of each mode. This fitting process also provided estimated errors for all the parameters. Variation of the integrated intensity vs. the pump power for mode (22,1) is shown in Fig. 2.4 as red circles. The light-light curve shows a clear kink, from which we estimated a 1.26 μW lasing threshold. Illustrated in the inset of Fig. 2.4 is the measured spectral linewidth that shows a clear reduction (from ~2.2 to 1.8 nm) at or near the lasing threshold. This linewidth narrowing, due to the increased temporal coherence, further suggests the

achievement of lasing. As previously discussed, the intrinsic linewidth can be substantially smaller, due to the presence of doublet modes [58] related to the spiral asymmetry of rolled-up semiconductor tubes. We have further calculated the integrated background emission to evaluate its behavior at different pump powers, shown as diamonds in Fig. 2.4. We chose a spectral width of ~ 4 nm, separated from the lasing peak by 8 nm, such that this spectral range is still approximately within the homogeneous broadening limit of the lasing mode. This spectral area is marked by the square box shown in Fig. 2.3 It is seen that, at or near the lasing threshold (between 1 and 2 μ W), the background emission stays nearly constant which is in direct contrast to the sharp increase of the intensity for the lasing mode (22,1). This observation is consistent with the fact that, for a semiconductor laser, the carrier density above threshold should be clamped at that of the threshold, thereby providing unambiguous evidence for the achievement of lasing. With further increasing power, the background emission shows a very small increase, with a slope more than 100 times smaller than that of the light-light curve for mode (22,1). This small increase can be explained by the commonly observed hot carrier effect of quantum dot lasers. At large injection conditions, charge carriers are thermally distributed into the many available states and can lead to enhanced background emission [91]. Also illustrated in Fig. 2.4 as black squares, the light-light characteristics of mode (22,4) are examined. The integrated peak area increases linearly with pump power, with no appreciable kinks. From this observation, we can conclude that this particular mode is not lasing. The fact that this mode does not show lasing behavior rules out experimental artifacts during the measurement as the cause of the observed lasing behavior of mode (22,1). Detailed analysis (not shown) further confirms that the emission at 1454 and 1462 nm, corresponding to modes (22,3) and (22,2), shows weak lasing behavior, and the rest of the peaks in the spectrum do not show evidence of lasing. It is envisioned that rolled-up semiconductor tube lasers, with multiple emission wavelengths and controlled emission characteristics, can be readily achieved using tube cavities with improved Q-factors by optimizing wall thicknesses and surface geometry.

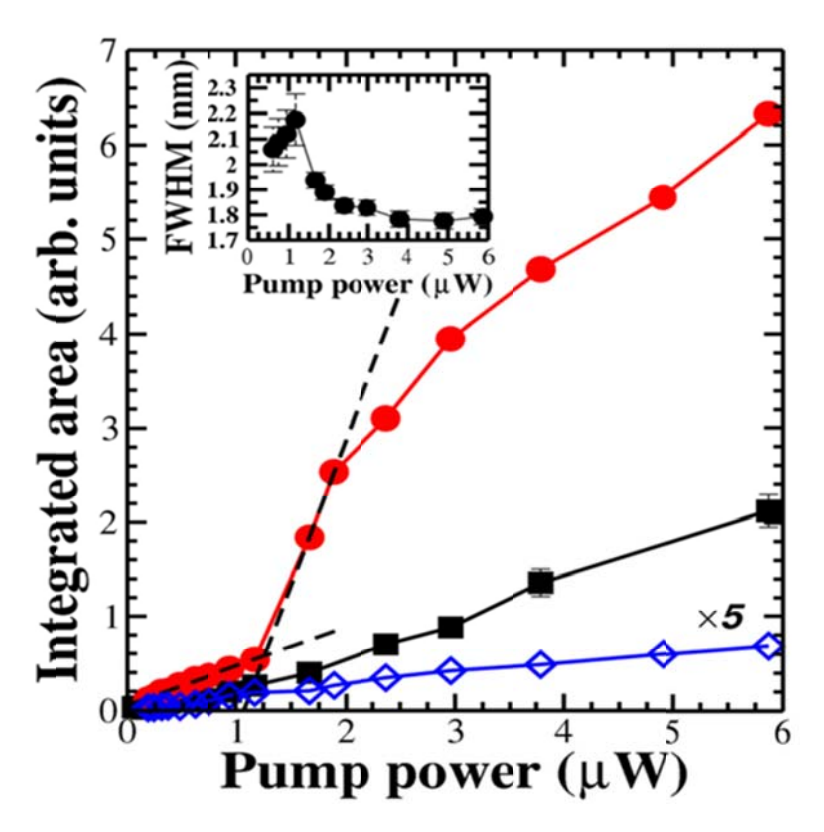


Figure 2.4 Light-light curve (circles) for modes (22,1) (circles) and (22,4) (squares) in Fig. 3.3. Mode (22,1) shows a lasing threshold of 1.26 μW pump power. The dashed lines are a guide to estimate the threshold power. Mode (22,4) shows no threshold behavior. The background emission extracted from the box in Fig. 3 (multiplied by a factor of 5 for better visibility) is indicated by the open diamonds. Inset: Full-width half-maximum (FWHM) of mode (22,1) as a function of pump power [94].

From the value of threshold pump power, we can use a rate-equation model [95] to estimate β , the fraction of spontaneous emission coupled to the optical mode. From this model, we can derive $\delta P th/(h\omega_p) = \omega_c/(Q\beta)(1+\tau_{sp}/\tau_{nr})$, where P_{th} is the pump threshold power, δ is the fraction of pump power absorbed by the InGaAsP matrix, ω_p and ω_c are the angular frequencies of the pump and cavity mode light, respectively, and τ_{sp} and τ_{nr} are the characteristic times for spontaneous and non-radiative recombination of an electron hole pair in the gain medium. Neglecting nonradiative recombination (which gives a lower bound on β , since $\tau_{nr} \rightarrow \infty$ in this case), and using Q = 1400 (from the mode linewidth below the lasing threshold, considering the presence of a doublet), $P_{th} = 1:26$ μW , $\lambda_p = 635$ nm, and $\lambda_c = 1470$ nm, and $\delta = 0.75$, we then obtain $\beta = 0.30$. We can also estimate the Purcell factor for the combined quantum-dot/microcavity system, using the formula [96]:

$$F_{p} = \left(\frac{3}{4\pi^{2}}\right) \left(\frac{\lambda_{c}}{n_{eff}}\right)^{3} \left(\frac{Q}{V_{eff}}\right) \tag{2.1}$$

(V_{eff} is the effective mode volume, while n_{eff} is the effective refractive index). With $n_{eff} \sim 2.09$ for the optical mode (obtained from an equivalent planar waveguide model) and $V_{eff} \sim 8.5~\mu m^3$, we derived a Purcell factor of ~ 4.8 . Both the spontaneous emission coupling factor and Purcell factor can be drastically improved by optimizing the Q-factors of the tube cavity.

2.3 InAs/InGaAsP Quantum Dash Tube Lasers at Room Temperature

To achieve room-temperature lasing from rolled-up microtube devices, a substantial increase in the total fabrication yield of the tubular microcavities with high Q factors and low optical loss was required. Additionally, in the new design, quantum dashes were used as the active gain material due to their large saturation gain compared to quantum dots. In this regard, some alterations to device fabrication have been made resulting in drastic improvement of the device Q factor and optical loss with near-perfect fabrication yield. In what follows the fabrication process together with characterization of the lasing tubes are presented. The photoluminescence setup to characterize the tubes is the same as the previously mentioned. A detailed discussion on the results is also presented.

2.3.1 Fabrication Procedure and Optimization

The quantum dot/dash tube device heterostructures were grown on InP substrate by CBE. Schematically shown in Fig. 2.5(a), the coherently strained InGaAsP bilayers consist of ~36 nm In_{0.81}Ga_{0.19}As_{0.41}P_{0.59} and ~15 nm In_{0.68}Ga_{0.32}As_{0.41}P_{0.59}, which are lattice matched to the InP substrate and tensile-strained, respectively. The rolling, depending on the mesa shape, generally takes place along <100> crystal directions [30]. Two layers of self-organized InAs quantum dashes are incorporated in the In_{0.81}Ga_{0.19}As_{0.41}P_{0.59} layer, shown in Fig. 2.5(a). Similar to previously described, a U-shaped mesa, shown in Fig. 2.5(b), was first defined by etching to the In_{0.81}Ga_{0.19}As_{0.41}P_{0.59} layer using HCl:HNO₃:H₂O (1:2:10) and with selective etching of the underlying InP substrate, the coherently strained InAs/InGaAsP quantum dot/dash heterostructures can roll into micro-

or nanotubes, shown in Fig. 2.5(c). To ensure that the rolling process initiates only at the starting edge of the U-shaped mesa, we have previously introduced a photoresist layer to cover part of the side pieces of the U-shaped mesa [94]. In this study, we have further improved the device fabrication process by introducing a recessed SiO₂ protective layer on the two side pieces of the U-shaped mesa, shown in Fig. 2.5(d).

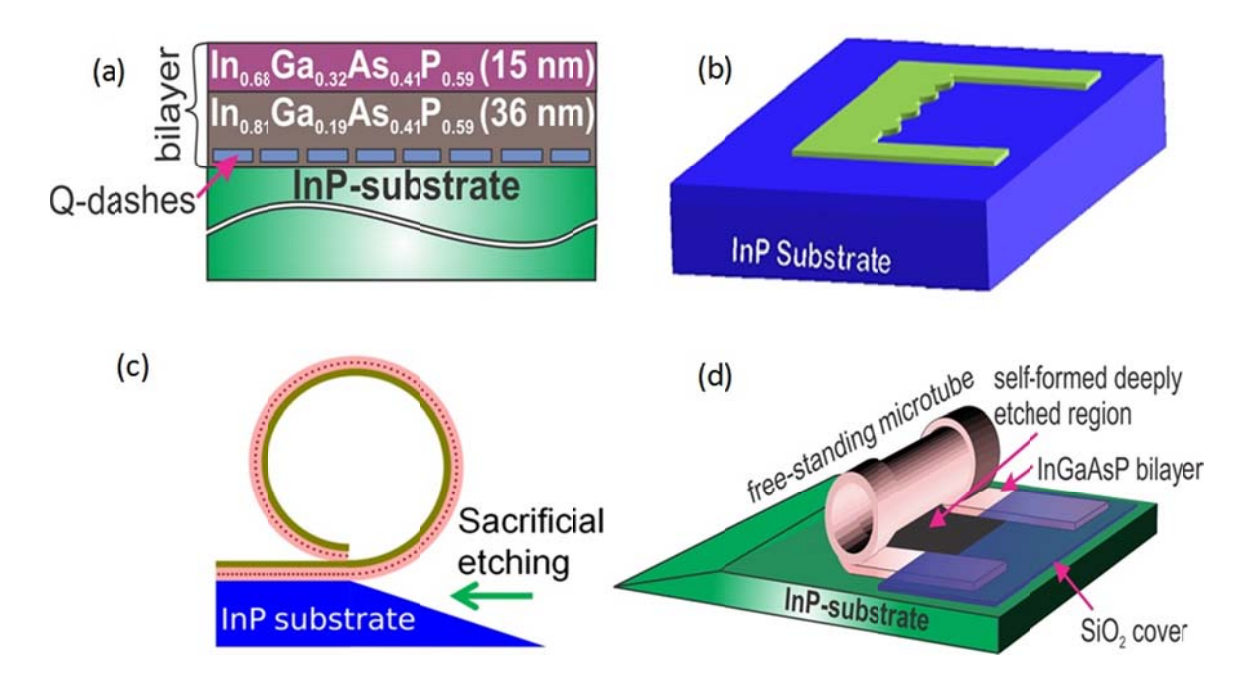


Figure 2.5 (a) Schematic illustration of InAs/InGaAsP quantum dash heterostructures grown on InP substrate. (b) Illustration of the U-shaped mesa. (c) Illustration of the formation of rolled-up InAs/InGaAsP quantum dot/dash microtubes when the underlying InP substrate is selectively etched. (d) Schematic of free-standing microtubes with SiO₂ protective layer covering the side pieces of the U-shaped mesa [60].

The tube rolling process stops when hitting the SiO_x layer. The recessed region of the SiO_x layer between the two side pieces can ensure that the center part of the tube cavity is not in contact with SiO_2 , thereby leading to reduced optical loss and high Q-factors. The scanning electron microscopy image of the fabricated device is shown in Fig. 2.6(a), wherein the various regions are identified. Significantly, near-perfect yield can be achieved using this device fabrication process. The optical image of arrays of rolled-up InAs/InGaAsP tubes is shown in Fig. 2.6(b).

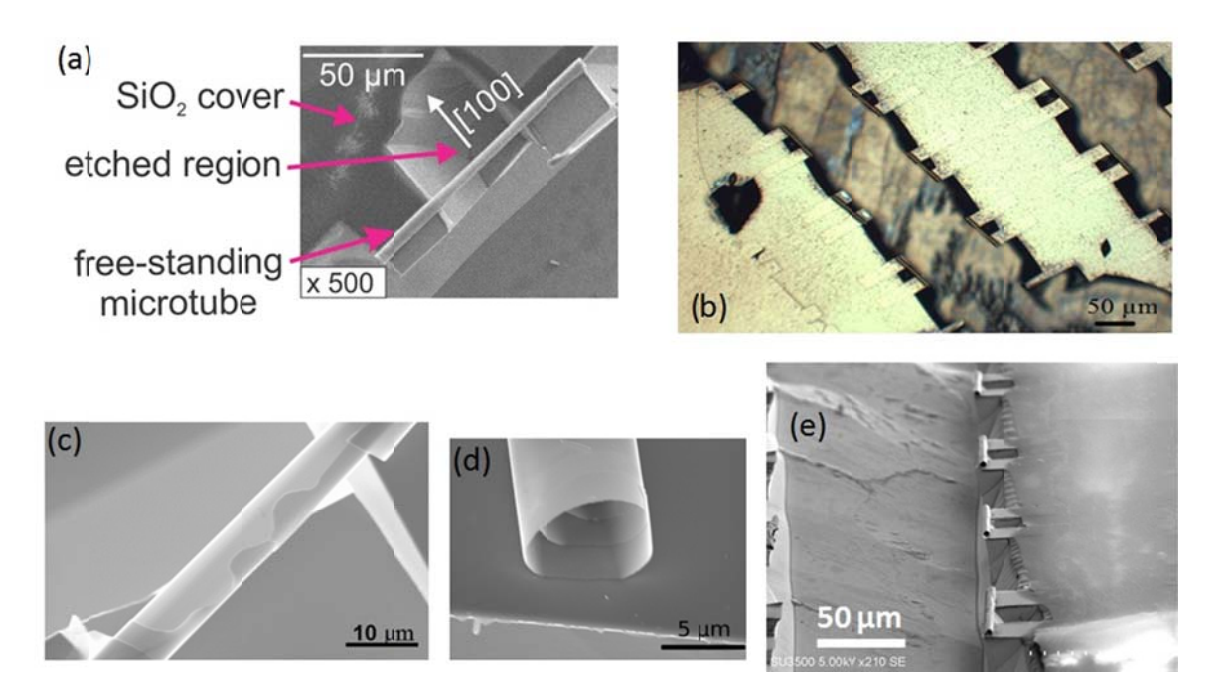


Figure 2.6 (a) SEM image of a free-standing microtube rolled along the [100] crystal direction. (b) Optical microscopy image from arrays of rolled-up InAs/InGaAsP tubes showing high fabrication yield. (c) SEM image of a microtube illustrating the engineered surface corrugations for axial mode confinement. (d) Cross-sectional SEM image of the microtube showing multiple turns. (e) SEM image from arrays of rolled-up InAs/InGaAsP tubes showing high fabrication yield.

Additionally, the surface geometry of the rolled-up tube optical cavity can be precisely defined by introducing corrugations along the inner edge of the mesa (see Fig. 2.5(b)). The resulting engineered surface geometry, shown in Fig. 2.6(c), can provide an effective optical confinement along the tube axial direction and offer an additional dimension for controlling the optical performance of rolled-up tube lasers. In this study, the wall thickness is \sim 50 nm for a single-turn tube. The tube wall thickness can be further varied by controlling the number of turns, i.e. the width of the center part of the U-shaped mesa. InAs/InGaAsP quantum dot/dash tubes, with diameters in the range of \sim 5 to 7 μ m and wall thicknesses of \sim 50 to 200 nm, depending on the number of turns, have been fabricated and characterized. The cross-sectional SEM image of a multi-turn tube is shown in Fig. 2.6(d). Also the SEM image from arrays of rolled-up InAs/InGaAsP tubes showing high fabrication yield is shown in Fig. 2.6(e).

2.3.2 Photoluminescence Studies and Discussions

The same micro-photoluminescence setup as previously described in section 2.3.1 was used in order to study the optical performance of the tube devices.

The emission spectrum measured from the tube at an excitation power of $\sim 19.9~\mu W$ is shown in Fig. 2.7(a). The corresponding azimuthal and axial mode numbers are identified. For comparison, also shown in the figure is the photoluminescence spectrum measured from the as-grown InAs quantum dash sample. The optical modes were analyzed by fitting them using Lorentzian functions to extract the corresponding integrated area and full-width-at-half-maximum (FWHM) at each excitation power level. Fig. 2.7(b) shows the integrated intensity vs. pump power for the mode (21,2) (at $\sim 1590~\mu M$) calculated from the results of power dependent measurements.

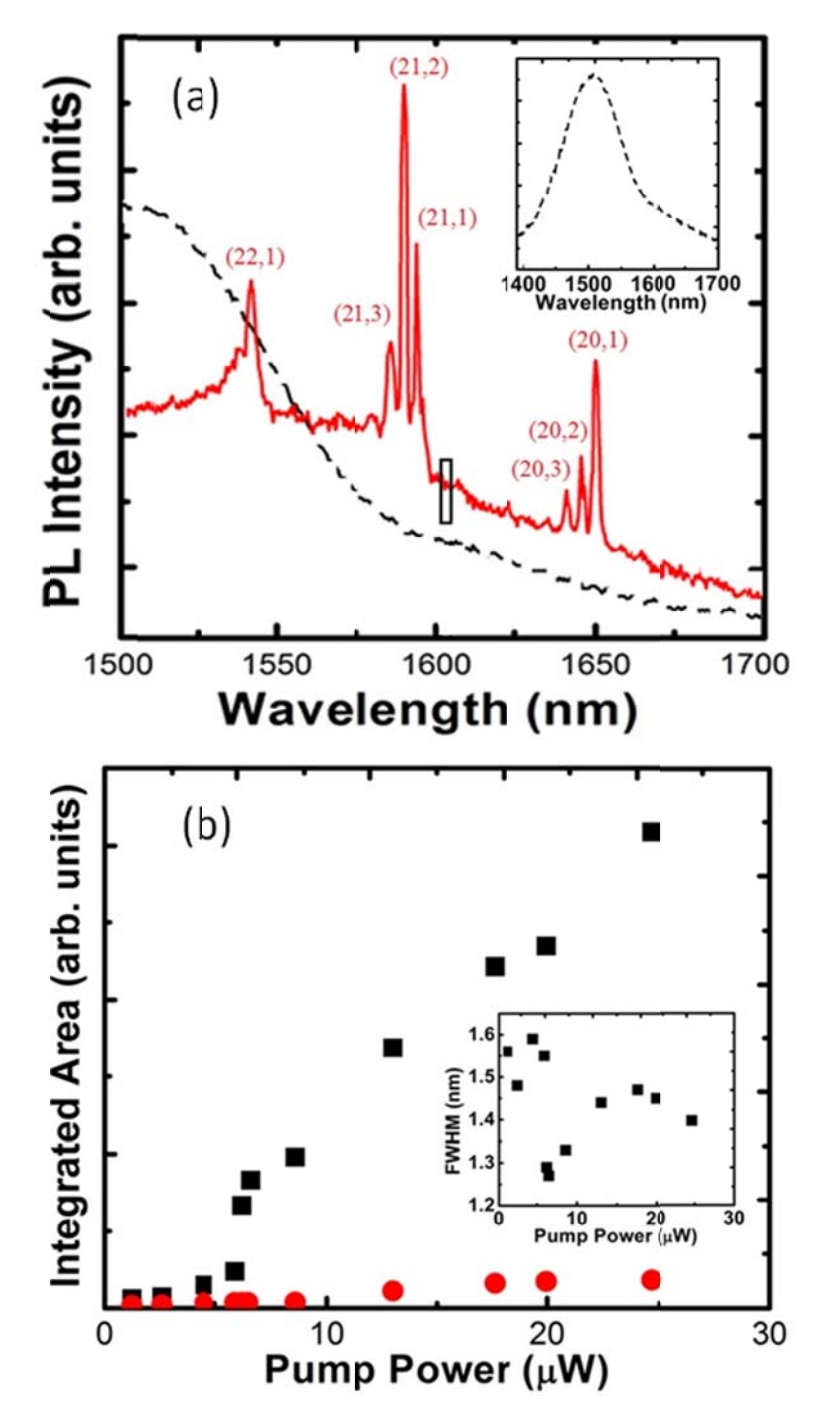


Figure 2.7 (a) Photoluminescence spectrum of a quantum dash microtube measured at room temperature with an incident pump power of ~19.9 μ W. The measured spectrum of the as-grown quantum dash sample is shown as the dashed lines and also in the inset. The curves are vertically shifted for display purpose. (b) Integrated intensity vs. pump power for the mode (21,2) and for the background emission extracted from the box shown in (a). The inset shows the FWHM of the mode (21,2) measured under various incident pump powers [60].

A clear threshold is observed at \sim 6 μ W excitation power level. Variations of the FWHM of this mode vs. pump power are shown in the inset. A reduction of the spectral linewidth from \sim 1.6 nm to 1.25 nm is also measured at the threshold, suggesting the achievement of lasing. It may also be noticed that the linewidth showed a small increase with increasing power, due to the heating effect of the tube device [49]. To further confirm the lasing behavior, we have derived the integrated background emission at different pump powers by calculating the integrated area of a spectral width of \sim 4 nm separated by \sim 12 nm from the mode (21,2) (see the square box in Fig. 2.7(a)). It is seen that the background emission is negligibly small and stays nearly constant at or above threshold power, shown in Fig. 2.7(b). With further increasing pump power, the background emission is slightly enhanced, due to the hot carrier effect commonly observed in quantum dot/dash lasers [91].

Similar analysis was performed for other modes shown in Fig. 2.7(a). However, a clear linewidth reduction or threshold behavior in the light-light plot was not measured, indicating lasing was not achieved for these modes. The underlying reason has been investigated. It is noticed that the mode (22,1) shows weaker emission, compared to the mode (21,2), which is in direct contrast to the strong photoluminescence emission from the as-grown sample in the wavelength range of ~ 1540 nm. Additionally, the mode (20,1) exhibits comparatively strong intensity in spite of the extremely weak photoluminescence emission from the as-grown sample in this wavelength range. This discrepancy is explained by the wavelength-dependent cavity Q-factor. Due to the large inhomogeneity of InAs quantum dashes, the cavity Q-factors for resonance modes at shorter wavelengths suffer severely from the photon absorption by non-resonant quantum dashes with relatively small transition energies. The reduction of the Q-factor of rolled-up tube optical cavities, due to the optical absorption by the quantum dots/dashes, has been further confirmed by the transmission measurements of such structures [97]. Additionally, the Q-factor associated with various axial modes can be strongly influenced by the shape of the surface geometry during the device fabrication process.

Compared to an ideal ring resonator, the Q-factor of rolled-up tube cavities is further limited by the rapid change in thicknesses at the discontinuous rolling edges, i.e. the inside and outside notches, which leads to strong light scattering.

Illustrated in Fig. 2.8 is the distribution of the simulated optical resonance mode (azimuthal mode of 21) for a microtube with a wall thickness of ~100 nm by the two-dimensional finite-difference time-domain method. It is seen that light scattered out by the inside notch can serve as useful output from rolled-up tube lasers, thereby leading to micro/nanoscale lasers with controlled directional emission. Moreover, the output coupling efficiency can be varied by controlling the number of turns. For example, a larger Q-factor can be achieved in rolled-up tube cavities with multi-turns, compared to a single turn device.

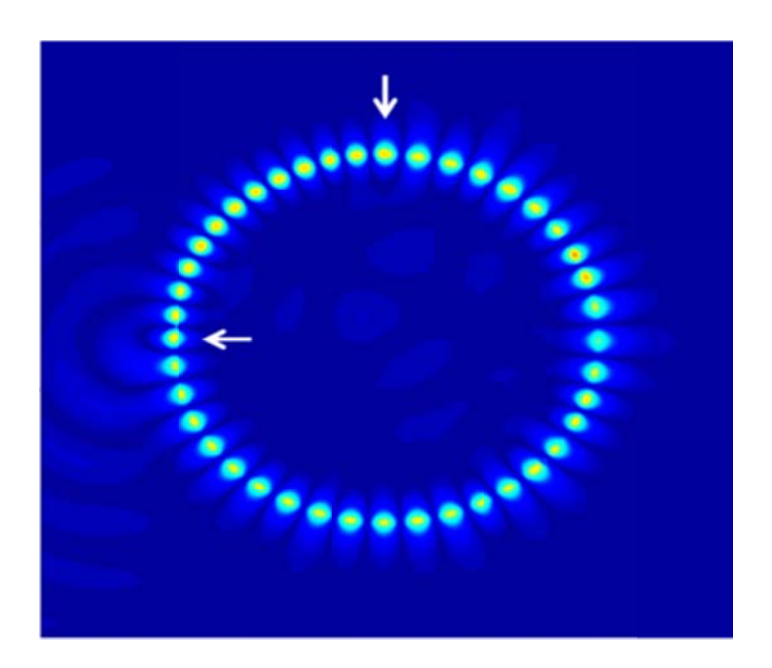


Figure 2.8 Simulated distribution of the resonance mode in a rolled-up InGaAsP microtube with a radius of \sim 2.4 μ m and wall thickness of \sim 100 nm by the two-dimensional finite-difference time-domain method. The presence of inside and outside notches are shown by the arrows [60].

For the lasing mode (21,2), Q is ~1,200, and $V_{\rm eff}$ and $n_{\rm eff}$ are estimated to be ~8 μ m³ and ~1.91, respectively. The Purcell factor is derived to be ~6.54 from equation (2.1). The spontaneous emission coupling factor (β) is further estimated to be ~0.87, indicating strong coupling of the spontaneous emission to the cavity mode.

2.4 Conclusion

In summary we have demonstrated optically-pumped InAs/InGaAsP quantum dot tube laser devices with emission at telecom wavelength, operating at 80 K. The laser devices show a threshold of $\sim 1.26~\mu W$ with Q-factor of ~ 1400 and estimated Purcell factor of $\sim 4.8.$ By taking advantage of high saturation gain of quantum dash active material and improving the device fabrication, we have demonstrated, for the first time, room-temperature optically-pumped tube lasers emitting at $\sim \! 1590$ nm. The laser threshold and the estimated Purcell factor of the devices were estimated to be $\sim 6~\mu W$ and of ~ 6.54 , respectively. The emission wavelengths of such laser devices can be further tuned by varying the dot sizes and/or compositions. Moreover, such nanophotonic devices can be transferred directly on a foreign substrate and monolithically integrated with Si-waveguides and other nanophotonic components in a CMOS compatible process, thereby leading to integrated nanophotonic circuits on a Si-platform required for the emerging chip-level optical communications.

Chapter 3. InAs/GaAs Rolled-Up Quantum Dot Infrared Photodetector Tube Devices

3.1 Introduction

A highly sensitive, nanoscale infrared photodetector that can be directly integrated with other electronic and optoelectronic components on a Si-platform is essentially required for the emerging chip-level optical interconnects [98]. In this regard, significant progress has been made in Ge and III-V based photodetectors grown directly on Si [99, 100]. Flip chip integration and bonding techniques have also been used to transfer the active InGaAs membrane devices onto Si [101]. The device performance, however, has been severely limited by the presence of high densities of dislocations, due to the large lattice and thermal mismatch between the device active region and the underlying Si substrate. Recently, significantly improved performance has been made by using self-organized quantum dot heterostructures grown directly on Si, due to the superior carrier confinement and reduced defect densities of the quantum dots [100, 102]. Self-organized quantum dot photodetectors can exhibit reduced dark current and high temperature operation, and the operation wavelength can be readily tuned by engineering the sizes/compositions of the dots.

In this chapter, we have demonstrated rolled-up InAs quantum dot tube photodetectors that can be potentially transferred directly on a Si-platform. The InAs quantum dot tube is formed by selectively releasing the coherently strained InAs quantum dot heterostructures from the host substrate. The pin diode is defined along the tube axial direction using a two-step ion implantation process. In this unique tube photodetector, the light absorption length and charge carrier transport can be separately optimized, promising both ultrahigh-speed and high-efficiency operation. At 300 K, the device responsivity is measured to be ~ 0.066 A/W at 1064 nm, with an external quantum efficiency of $\sim 8\%$.

3.2 Device Design and Fabrication Procedure

The coherently strained InAs/GaAs quantum dot heterostructure was first grown on GaAs substrate by molecular beam epitaxy. As schematically shown in the inset of Fig. 3.1(a), the device heterostructure consists of a 50 nm AlAs sacrificial layer, 20 nm In_{0.18} Ga_{0.82}As and 30 nm GaAs with the incorporation of self-organised InAs quantum dots. Rolled-up InAs/GaAs quantum dot tubes can be spontaneously formed due to strain relaxation as discussed in section 1.2.1. Prior to the tube formation, a two-step ion implantation of Si and Be was performed to selectively dope part of the tube to be n- and p-type, respectively, shown in Fig. 3.1(a). A SiO_x protective layer was used to protect the rest of the sample during ion-implantation which was subsequently removed after implantation process. The centre region of the tube, with a width of ~ 1.5 µm, is nominally undoped, which serves as the device active region. The implanted dopant was activated by annealing the sample at \sim 710°C for 20 s with the use of a suitable SiNx capping layer. Ni/Ge/Au (10/20/100 nm) and Pd/Ti/Pd/Au (10/10/40/100 nm) were deposited as the n- and p-metal contacts, respectively. The fabrication is continued by thermal annealing of the contacts at 400°C for 1 min and then defining the rolling edge and the U-shaped mesas using photolithography steps and wet etching.

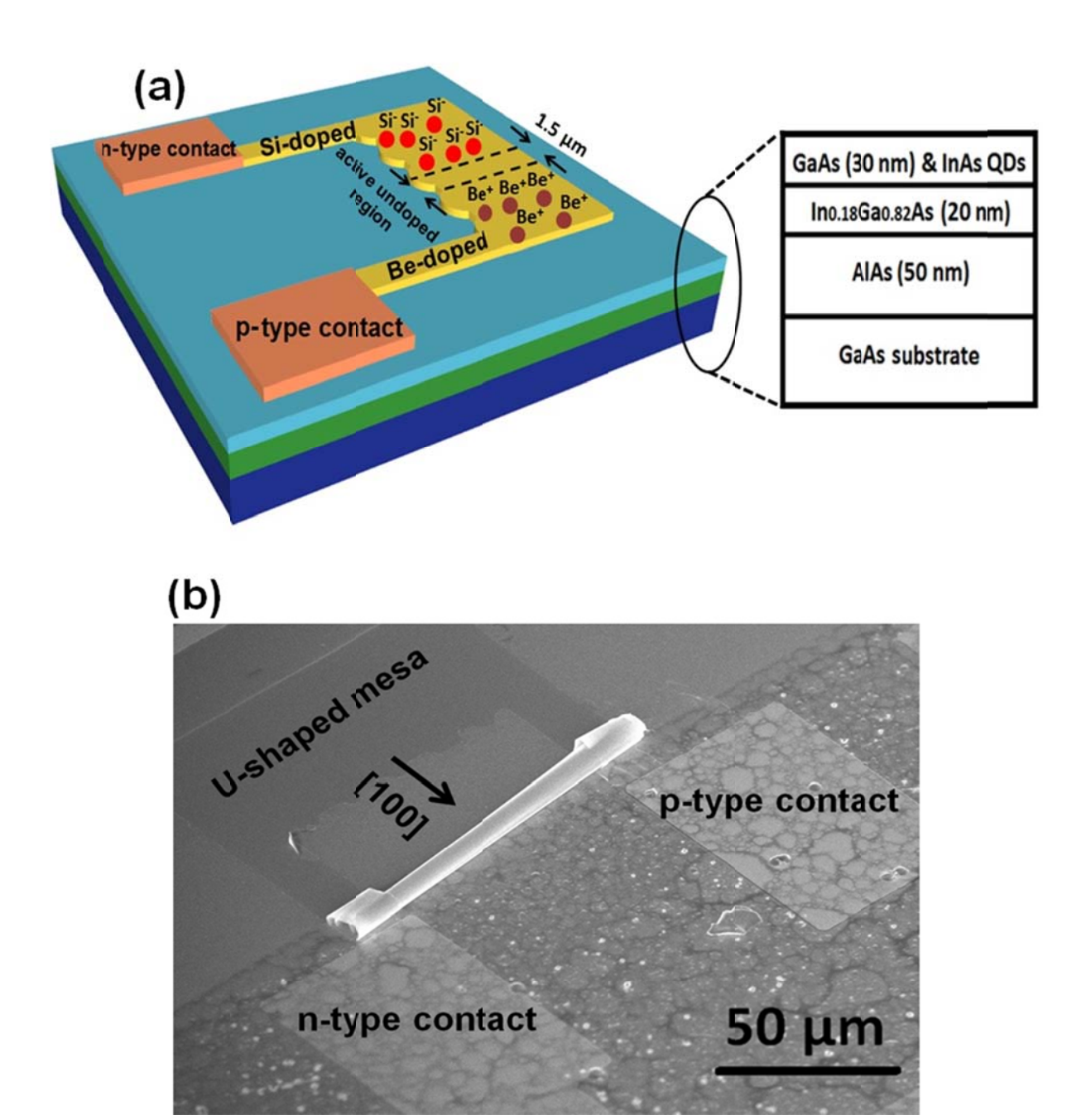


Figure 3.1 (a) Schematic illustration of the fabrication of InAs quantum dot tube photodetectors. The p-i-n junction is defined by selective Si and Be implantation. The undoped active region is not drawn to scale. The tube device is formed by selectively etching the underlying AlAs sacrificial layer of a U-shaped mesa. The InAs/GaAs quantum dot heterostructure is shown in the inset. (b) SEM image of the fabricated InAs quantum dot tube photodetector. The arrow indicates the tube rolling direction [72].

Upon sacrificial etching, the InAs/GaAs quantum dot nanomembrane can gradually rollup, due to the strain release, and form a tubular structure. The schematic of the U-shaped mesa together with the metallic contacts on the doped areas is shown in Fig. 3.1 (a). Fig. 3.1 (b) shows the SEM image of the microtube together with the ohmic contacts.

3.3 Measurement Results and Discussion

The performance of InAs quantum dot tube detectors was studied at 80 K and 300 K. Illustrated in Fig. 3.2(a), the tube device exhibits excellent current-voltage characteristics, with a relatively low level of dark current (\sim 140 nA) at -5 V. Both He-Ne laser (\sim 632.8 nm) and Nd:YAG laser (1064 nm) were used as the optical excitation source. The laser beam was focused on the device active region through a 100× objective with a diameter of \sim 1 μ m. Shown in the inset of Fig. 3.2(a), clear photo-response was measured under both 632.8 nm and 1064 nm excitation at 300 K. The incident power is \sim 13 μ W. At -5 V, the measured photocurrent is \sim 4 μ A and \sim 1.6 μ A at 632.8 nm and 1064 nm, respectively. The larger photocurrent at 632.8 nm excitation is due to the additional response of the GaAs layer.

The responsivity of the InAs quantum dot photodetector was derived by measuring the photocurrent under varying excitation intensities at a fixed bias voltage. Fig. 3.2(b) shows the responsivity of the device versus applied bias for 1064 nm excitation at 84 K and 300 K.

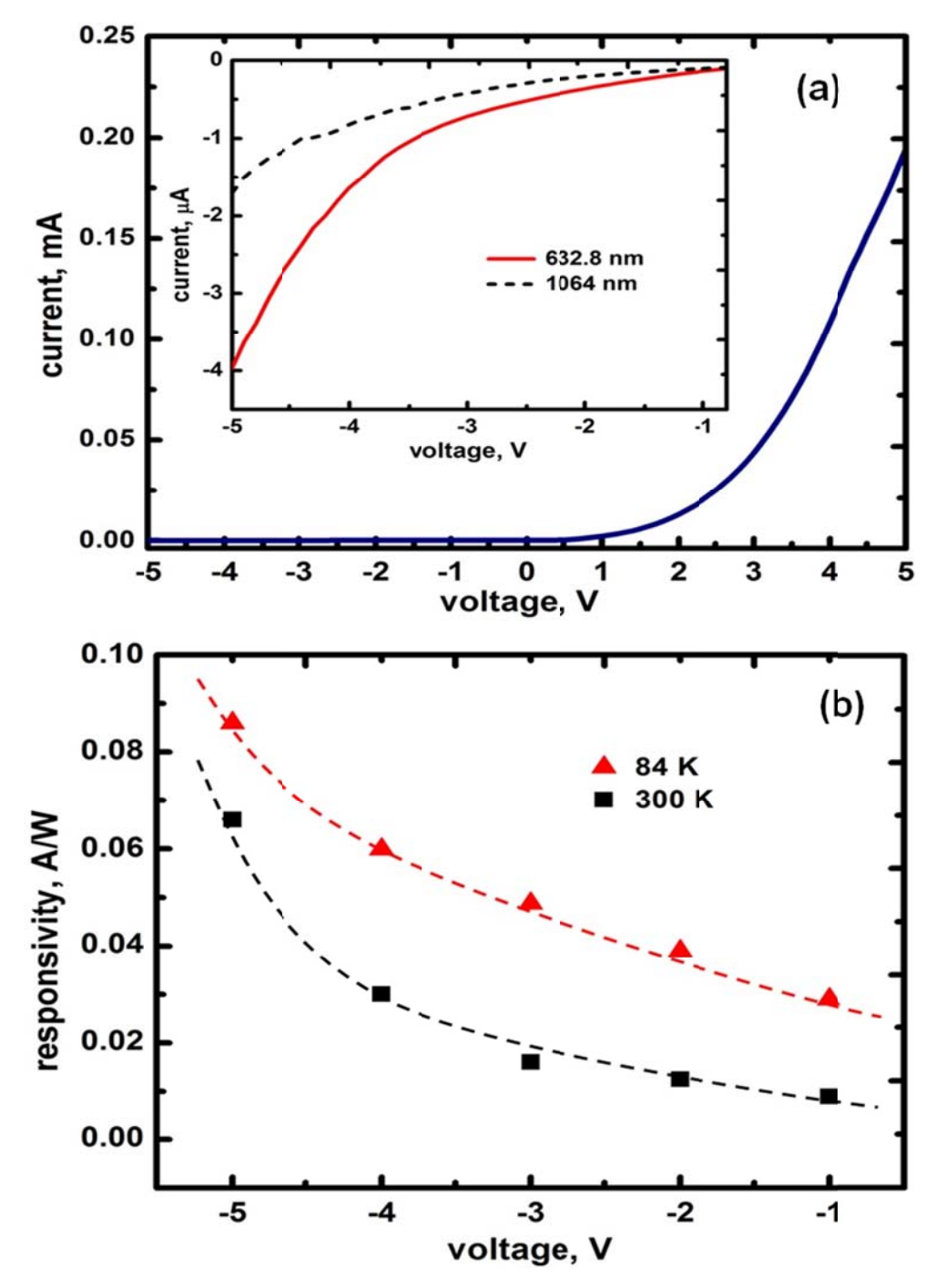


Figure 3.2 (a) Measured current versus voltage under dark condition. The inset shows the I-V under 632.8 nm and 1064 nm excitation at 300 K. (b) Responsivity of the tube detector versus the applied bias for 1064 nm excitation at 84 K and 300 K [72].

At V = -5 V, the responsivity was measured to be ~ 0.086 A/W and 0.066 A/W at 84 K and 300 K, respectively. Under 632.8 nm excitation, the responsivity was measured to be ~ 0.2 A/W at -5 V at 300 K. The external quantum efficiency is then calculated by QE(λ) = R(λ)(h)(c/e λ), where QE(λ) is the wavelength dependent external quantum efficiency, λ is the wavelength, λ is the Plank's constant, λ 0 is the speed of light in vacuum, and λ 0 is the elementary charge. At -5 V, the external quantum efficiency of the InAs quantum dot tube detector is λ 0.1 and λ 0.08 at 1064 nm at 84 K and 300 K, respectively. It is expected that with increasing the number of InAs quantum dot layers within the structure, the responsivity and quantum efficiency of the device can be further enhanced.

3.4 Conclusion

In summary we have demonstrated the first nanoscale tube photodetector, with the use of rolled-up InAs quantum dot tubes. The devices can exhibit responsivity of ~ 66 mA/W and external quantum efficiency of $\sim 8\%$ under 1064 nm excitation at 300 K. Additionally, the operating wavelength range of such devices can be readily tuned by engineering the sizes/compositions of the embedded quantum dots. Moreover, such devices can be further designed as resonantly enhanced photodetectors, leading to both ultrahigh efficiency and wavelength selective operation.

Chapter 4. Electrically Injected InP/InGaAsP Quantum Well Tube Lasers at Telecom Wavelength

4.1 Introduction

An electrically injected, low threshold micro- or nanoscale laser that can be integrated on a Si platform is essentially required for future chip-level optical communications, driven by the increasing demand for high data rate and low energy budget [15]. In this regard, different types of optical micro-/nano cavities have been intensively studied over the years [23, 24, 26, 103-108]. Among them are rolled-up semiconductor tubes, fabricated by selectively releasing strained nanomembranes from their host substrates, exhibit unique characteristics as described previously in section 1.2.3 including ultra-high Qfactors, directional emission, and controlled polarization[32, 49, 55, 60]. In addition, an exact tailoring of the optical emission characteristics can be achieved using standard photolithography process, which is in direct contrast to the extensive use of electronbeam lithography for the fabrication of photonic crystal, micro-disk, micro-pillar, and other micro/nanoscale optical cavities. As discussed in previous chapters, optically pumped rolled-up tube lasers incorporating self-organized quantum dots, quantum dashes, or quantum wells as the gain media have been demonstrated at both low temperature [89, 94] and room-temperature [26, 60, 90]. However, their practical application has been severely limited due to the lack of electrically driven types of devices.

The difficulty in achieving electrically injected lasing of rolled-up tubes, or any other whispering-gallery-mode based cavities lies in the highly inefficient carrier injection process of a conventional vertical p-i-n structure, due to the very thin nanomembranes [25, 109-111]. In addition, the optical performance, including the WGM profiles and Q-factor, can be adversely affected by the presence of electrical contacts and the heating effect, due to the large resistance and large surface recombination. In this chapter, we have investigated the design, fabrication and characterization of our novel electrically injected InP/InGaAsP rolled-up tube lasers, wherein multiple InGaAs quantum wells are

incorporated as the gain media. Efficient carrier injection into the device active region is achieved using a lateral carrier injection scheme without compromising the optical emission characteristics. The device exhibits a relatively low threshold current of ~ 1.05 mA at 80 K. The Purcell factor is estimated to be ~ 4.3 .

4.2 In_xGa_{1-x}As Quantum Well Heterostructure Design

The InP-based heterostruture of InGaAsP strain-driven tube devices embedding In_xGa_{1-x}As quantum wells is very similar to the previously discussed InAs/InGaAsP QD material layer structure described in chapter 2. However, since the tube formation mechanism and its final diameter is sensitively related to the existing and known strain within the heterosturcture, the incorporation of In_xGa_{1-x}As quantum well active layers should not impose any new strain to the crystalline structure, i.e. the composition of In_xGa_{1-x}As active layers must be such that they are lattice matched to their underlying crystalline material. Therefore, two layers of ~ 7 nm In_{0.53}Ga_{0.47}As quantum wells were grown on top of In_{0.81}Ga_{0.19}As_{0.41}P_{0.59} layers as shown in Fig. 4.1 (a). Also, the InGaAsP bilayer is doped *n*-type using silicon with the doping level of ~ 2×10^{17} cm⁻³. This was done to avoid the need for two step ion-implantation for carrier injection during later fabrication steps as was performed for the tube photodetector described in Chapter 3. The quantum well heterostructures exhibit strong photoluminescence emission, with the peak position at ~ 1.57 μ m at room temperature, illustrated in Fig. 4.1 (b).

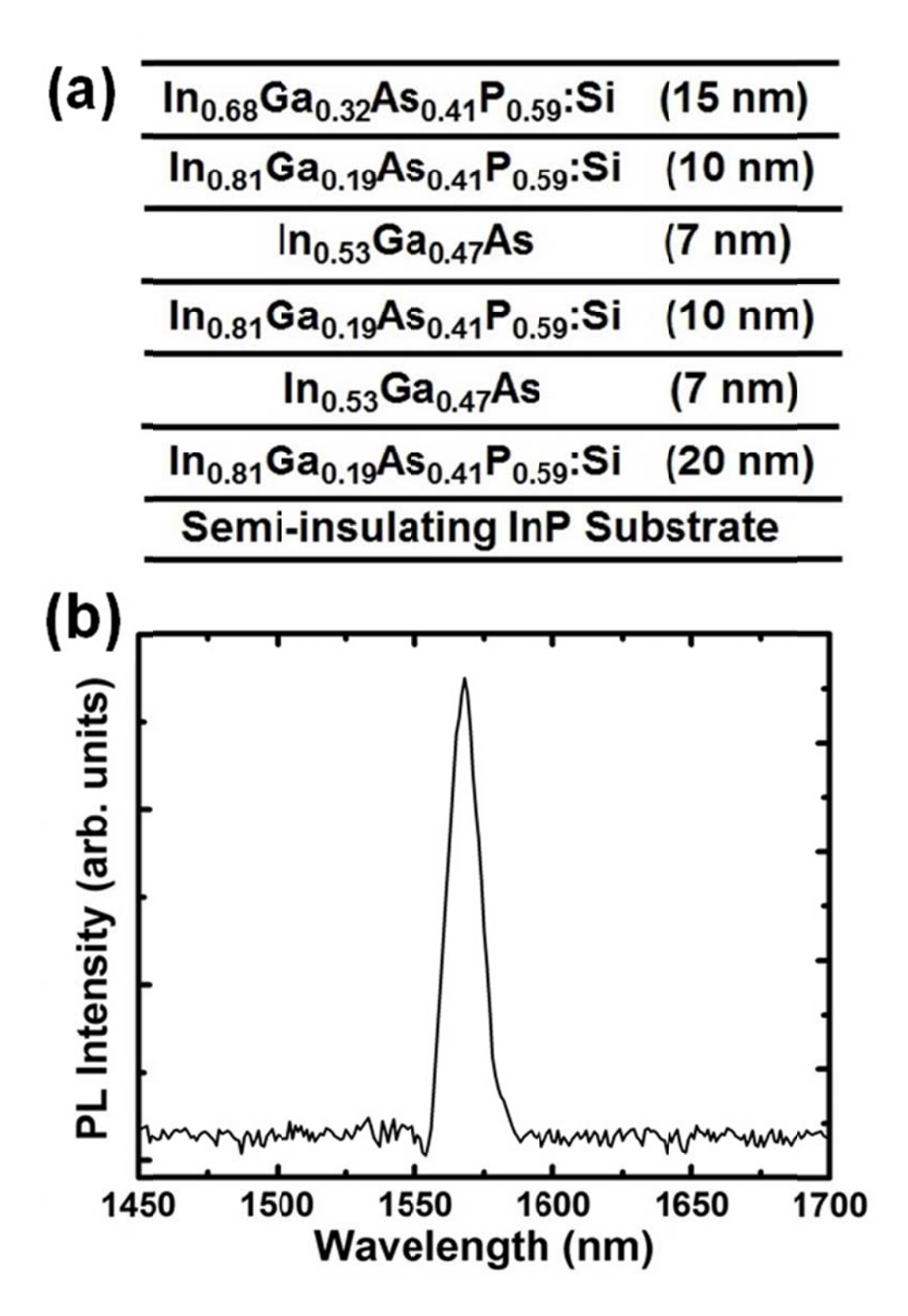


Figure 4.1 (a) Schematic of coherently strained InGaAs/InGaAsP quantum well heterostructures grown on semi-insulating InP substrate. (b) Photoluminescence spectrum measured at room temperature [112].

4.3 Fabrication Procedure

The fabrication of electrically injected rolled-up tube lasers is similar to the previously discussed optically pumped devices and quantum dot tube detectors. To achieve high Qfactors, it is imperative to develop free-standing microtube structures. This can be realized by employing a U-shaped mesa design, wherein the device active region is freestanding and is supported by the two side pieces, shown in Fig. 4.2(a). To achieve electrically injected device, a single step ion-implantation of Be was first performed to selectively p-dope part of the U-shaped mesa with a doping level of $\sim 2 \times 10^{19}$ cm⁻³. The implanted dopant was activated by annealing the sample at ~ 600 °C for 35 seconds. Prior to the annealing, the sample was covered by a 40 nm SiN_x capping layer to prevent the of out-diffusion arsenic and phosphor atoms. Subsequently, Ni/Ge/Au (20nm/30nm/100nm) and Pd/Ti/Pd/Au (10nm/40nm/40nm/100nm) were deposited as the *n*- and *p*-metal contacts, respectively, followed by an annealing at 400 °C for 1 min. The U-shaped mesa was defined by photolithography and etching into the top In_{0.81}Ga_{0.19}As_{0.41}P_{0.59} layer using HCl:HNO₃:H₂O (1:2:10) solution. With appropriate protection layers for the metal contacts, the sample was immersed in HCl:H₂O (2:1) solution to selectively etch the underlying InP layer, which leads to the formation of freestanding InGaAsP tubes, due to the strain relaxation. Shown in Fig. 4.2(a) is an optical microscopy image of a rolled-up microtube with the presence of p- and n-metal contacts on the two side pieces. The fabricated devices are ~ 100 µm long and have a wall thickness of ~ 140 nm. The scanning electron microscopy image of an electrically injected tube device is shown in Fig. 4.2(b). The deeply etched region beneath the rolledup device can be clearly identified, which is formed during the sacrificial etching step and reduces the leakage of optical modes into the substrate. Illustrated in Fig. 4.2(c), the tube devices have diameters of $\sim 5 \mu m$, which are largely determined by the relative thickness and strain of the InGaAsP bilayer [27]. Shown in Fig. 4.2(d), the presence of corrugations on the tube surface can be clearly identified, which provide strong optical confinement along the tube axial direction [54]. The controlled surface geometry was defined by the corrugations introduced at the inner edge of the U-shaped mesa. Fig. 4.3 shows a flow-chart illustrating the key device fabrication steps.

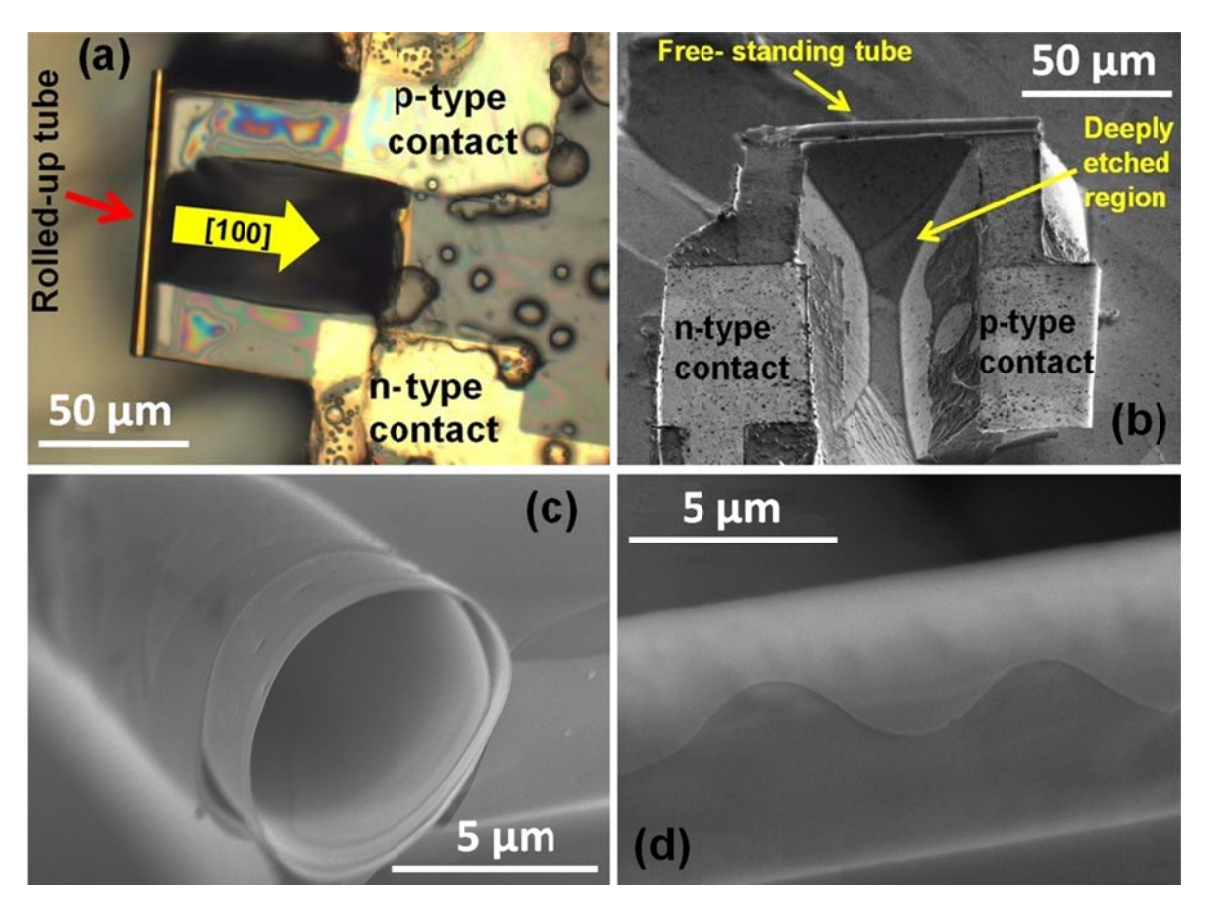


Figure 4.2 (a) Optical microscopy image of a free-standing rolled up tube device with the presence of n- and p-metal contacts on the two side pieces. The yellow arrow shows the rolling direction of the tube device. (b) SEM image of the fabricated tube device with *n*-and *p*-metal contacts. (c) SEM image of the tube device showing the side view of the tube cavity. (d) SEM image of the free-standing part of the tube device showing the presence of surface corrugations for axial mode confinement [112].

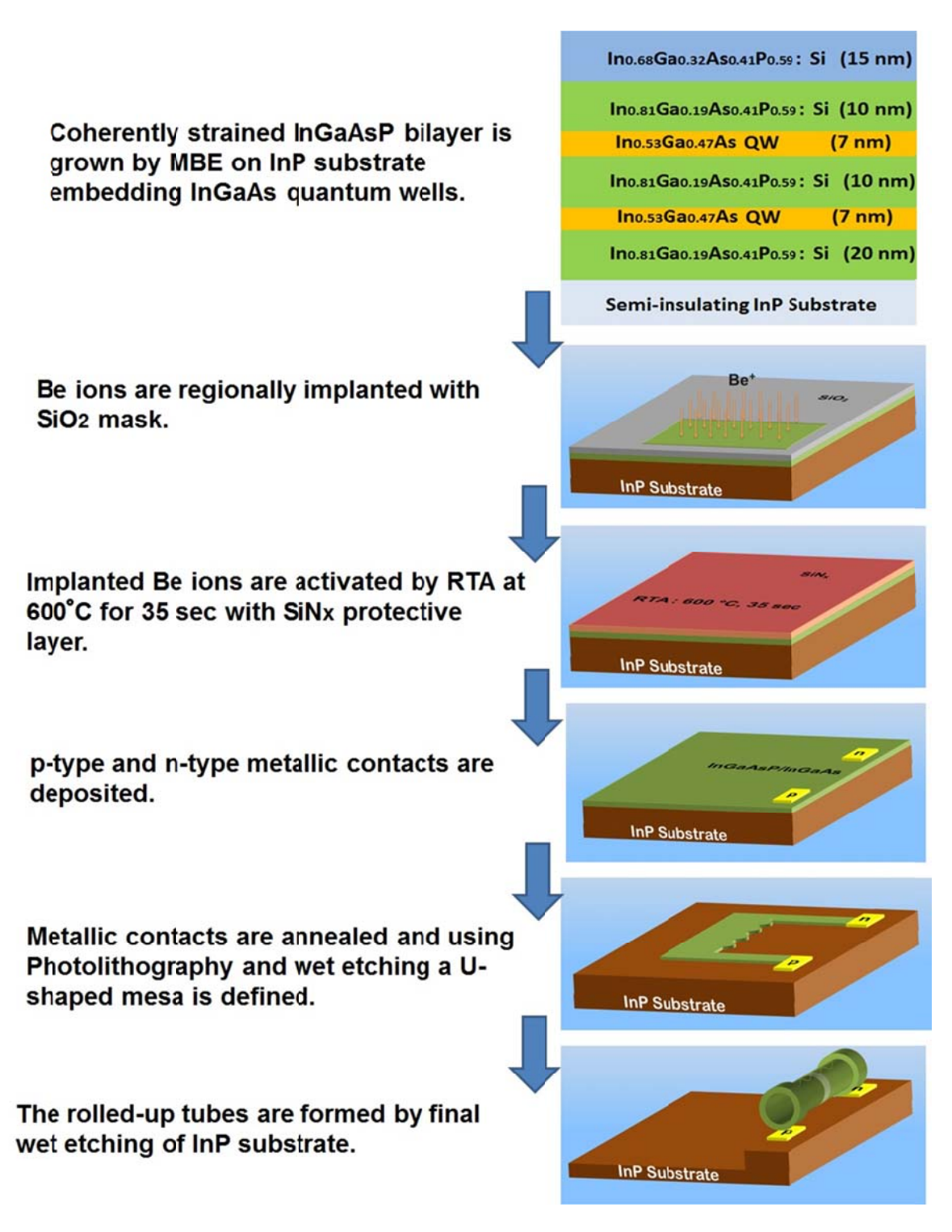


Figure 4.3 Schematic flow chart presenting the key device fabrication steps.

It is important to notice that to properly activate the implanted ions, they should be annealed at $\sim 800\text{-}900^{\circ}\text{C}$. However, no rolling of the strained bilayers was observed for

annealing temperatures well above $\sim 600^{\circ}\text{C}$. This is probably due to alterations in the crystalline structure of the strained bilayer at temperatures significantly higher than the growth temperature of the device heterostructure, i.e. $\sim 450^{\circ}\text{C}$.

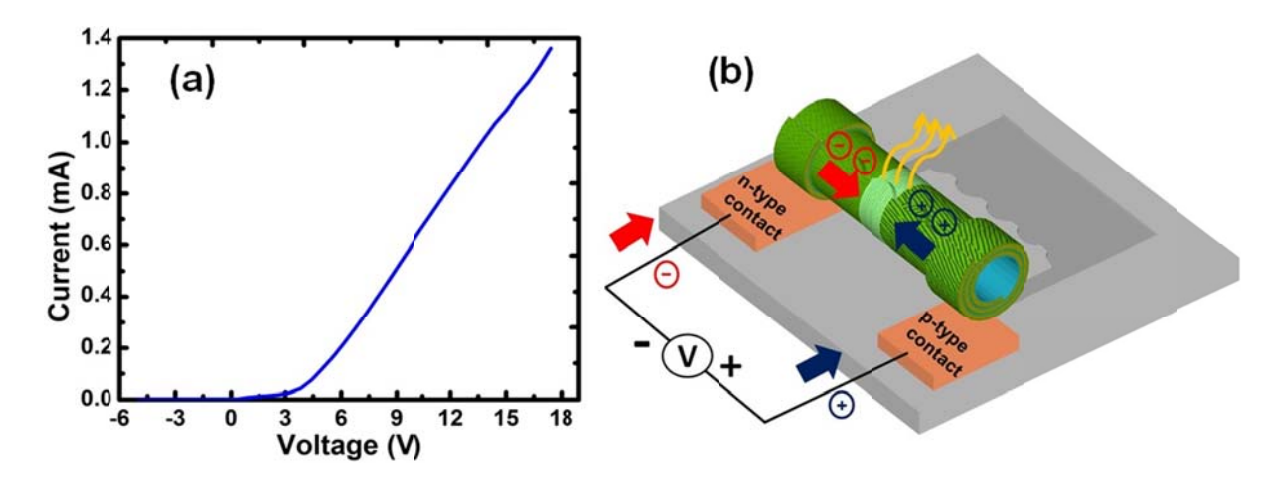


Figure 4.4 (a) Measured current-voltage characteristic of the device at room temperature. (b) Schematic of the electrically injected free-standing rolled-up tube laser on InP substrate [112].

This limitation in the applicable processing temperature has an adverse effect on the device characteristics, evidenced by the increased resistance as shown in Fig. 4.4 (a).

4.4 Electroluminescence Results and Discussion

The schematic of the current injection and light emission for the tube device is illustrated in Fig. 4.4(b). The device was measured under pulsed biasing conditions (1 KHz, 8% duty cycle) at 80 K. An optical fiber was used to collect the light emission, which was analysed by a spectrometer and detected by a liquid nitrogen cooled InGaAs detector with lock-in amplification. The output spectrum measured at 0.9 mA and 1.25 mA are shown in Fig. 4.5(a). The corresponding azimuthal and axial mode numbers are identified. The optical modes measured at various injection currents were analysed by using a Lorentzian function fitting method to derive the corresponding integrated area and full-width-at-half-maximum (FWHM). Fig. 4.5(b) shows the integrated intensity versus current for the mode (24,1) (\sim 1485 nm), which exhibits a clear threshold at \sim 1.05 mA. Variations of the FWHM of this lasing mode with current are shown in the inset of Fig. 4.5(b). A clear reduction of the spectral linewidth from \sim 3.3 nm to \sim 2 nm at the

same current value (~ 1.05 mA) is measured, further confirming the achievement of lasing. With further increasing the pumping current, the linewidth of this mode is slightly increased due to the heating effect of the tube device [97]. In addition, due to the presence of doublet modes related to the spiral symmetry of the tube cavity, the intrinsic linewidth of the lasing mode can be significantly smaller [58]. The heating effect, due to the relatively large resistance, also contributes to the measured spectral linewidth. Similar analysis of other modes does not show any lasing behaviour.

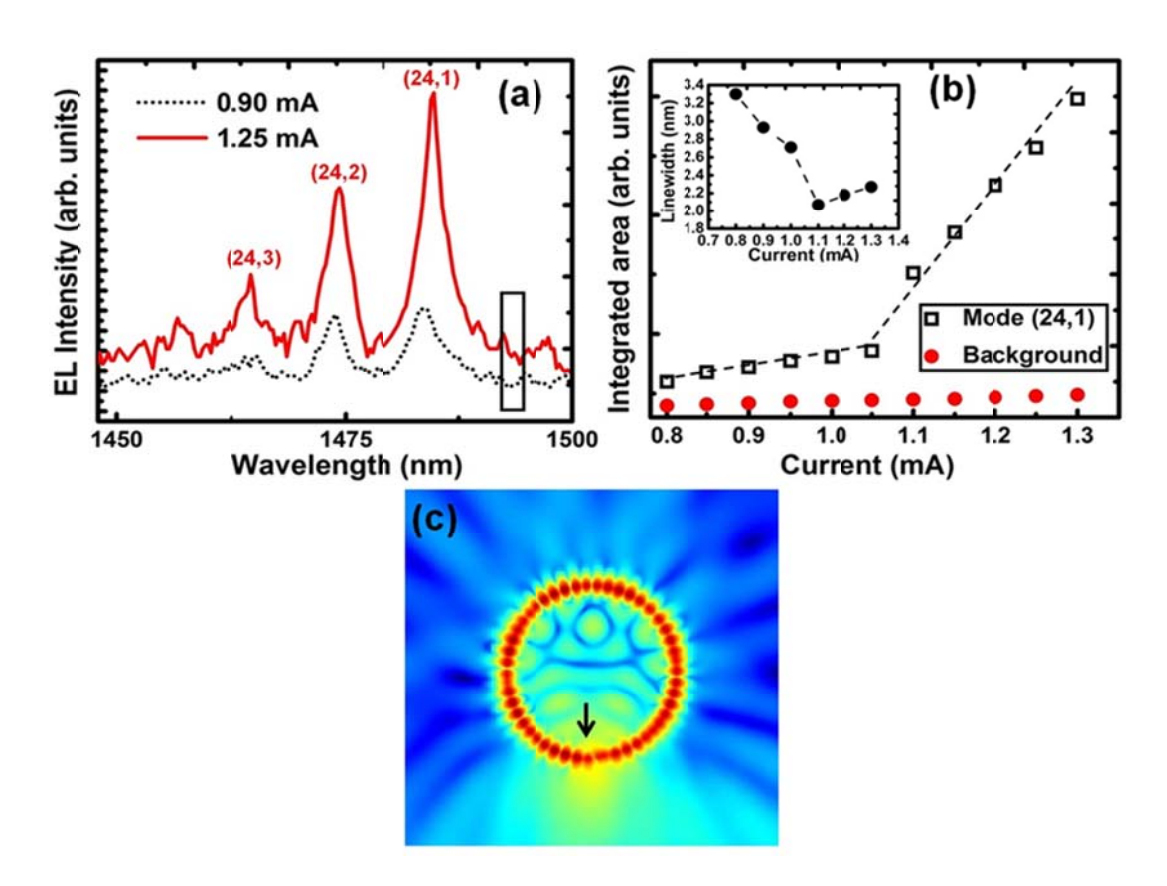


Figure 4.5 (a) Electroluminescence spectra of the rolled-up tube device measured at 0.9 mA (below threshold) and 1.25 mA (above threshold). (b) Integrated intensity versus current for the mode (24,1) and for the background emission extracted from the box shown in (a). Inset: Full-width-at-half-maximum of the mode (24,1) versus current. (c) Resonance mode distribution in a rolled-up InGaAsP tube with a wall thickness of \sim 140 nm and diameter of \sim 5 μ m calculated by the two-dimensional finite-difference time-domain method. The presence of inside notch is shown by the arrow [112].

In order to evaluate the behaviour of background emission at different currents, we have calculated the integrated area of a spectral width of ~ 4 nm separated from the mode

(24,1) by ~ 8 nm. This spectral area is shown as the square box in Fig. 4.5(a). It is observed that, compared to the intensity of the lasing mode, the background emission shows a negligible increase at or above the threshold current. This provides further evidence for the observed lasing behaviour, as the carrier concentration is clamped at the threshold value. By further increasing the current, a small increase in the background emission is observed which can be described by hot carrier effect [91].

The distribution of the stimulated optical resonance azimuthal mode for a rolled-up tube with a wall thickness of \sim 140 nm by the two-dimensional finite-difference time-domain method is shown in Fig. 4.5 (c). The scattered light by the inside notch is clearly seen, which can be used as the useful output of such devices, leading to controlled directional emission. For the rolled-up quantum well tube laser, the maximum Purcell factor is estimated by equation (2.1). For the lasing mode (24,1), Q is derived to be \sim 800, and V_{eff} and n_{eff} are estimated to be \sim 4 μm^3 and \sim 2.26, respectively. The Purcell factor is then calculated to be \sim 4.3.

Measurements were also done at higher temperatures but no lasing was observed. This is probably due the particularly high surface recombination velocity of $In_xG_{1-x}As$ compared to other types of semiconductors as shown in Table 4.1 [113]. Surface recombination result in heating of the surface and also reduced luminescence efficiencies associated with non-radiative recombination at the surface.

Semiconductor	Surface recombination velocity (cm/s)
GaAs	10 ⁶
GaN	5 × 10 ⁴
InP	10^3
Si	10 ¹

Table 4.1 Surface recombination velocities for different semiconductors

In addition to the heterostructure with InGaAs QW active material, we had also employed another heterostructure with embedded InAs quantum dots similar to the structure in Fig. 2.1 (a) only with Si-doped InGaAsP bilayer material. The doping level was also similar to that of QW structure. The structure is shown in Fig.4.6 with strong and broad PL emission very much similar to the as-grown material PL shown in Fig. 2.3. Although the fabricated devices show comparable I-V characteristics to QW devices but no EL was measured from QD tubes possibly due to their smaller saturation gain compared to InGaAs QWs and also the heating effect.

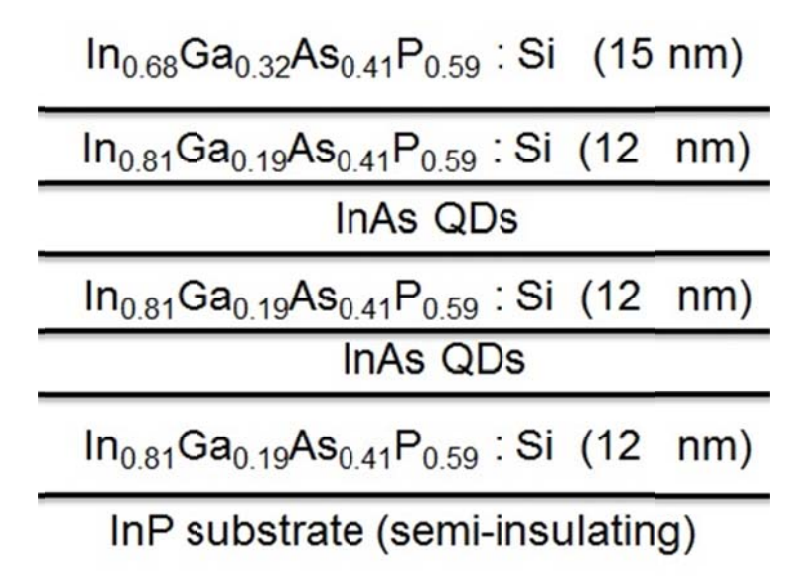


Figure 4.6 Schematic of coherently strained InAs/InGaAsP QD heterostructures grown on semi-insulating InP substrate.

4.5 Conclusion

In summary, we have demonstrated, for the first time, electrically injected rolled-up semiconductor tube laser at 80 K with the incorporation of multiple InGaAs quantum wells as the gain medium [112]. The lasing threshold was measured to be ~ 1.05 mA operating at the telecom wavelength range. Such devices can be readily transferred on silicon substrates, enabling the seamless integration with Si-waveguides, modulators, and other electronic and photonic components and provide an electrically injected coherent light source for applications in chip-level optical communications.

Chapter 5. Deep Ultraviolet AlN Nanowire LEDs

5.1 Introduction

In addition to microtube light sources, III-nitride nanowire LEDs and lasers are also important for applications in Si photonics, as they can be grown on Si and are free of dislocations. LEDs and lasers out of III-nitride materials can exhibit emission from DUV to NIR and there have been many reports on such III-nitride light emitting devices [82, 114, 115]. Planar DUV LEDs do not show high performance due to high densities of dislocations as a result of the lack of suitable substrates and difficulties in impurity doping due to the high activation energy of Mg. In addition, they present very low light extraction efficiencies. Due to low defect structure of nanowires, their high surface-tovolume ratio and low effective index, nanowire LEDs can outperform their planar counterparts. In this chapter, the growth, fabrication process, and electrical characterization of the first AlN nanowire LEDs emitting at 210 nm are discussed. These devices show low turn-on voltage of ~ 6 V which is much lower compared to planar AlN LEDs. Also a clear band-edge emission is observed at ~ 210 nm. Our III-nitride nanowires are grown on Si substrate by PAMBE, fabricated, and then subsequently characterized. The fabrication of UV nanowire LEDs has proven to be challenging due to the requirement of a suitable passivation material that is highly transparent in the UV range. In what follows, the fabrication procedure of the AlN LEDs and their electroluminescence results are presented. Subsequently, the processing and transmission characterization of a new passivation and planarization polymer material is described that is suitable for UV nanowire light emitting devices.

5.2 AlN nanowire LEDs

In what follows, a brief description of PAMBE system used to grow the III-N nanowires together with the fabrication process and characterization of AlN nanowire LEDs is presented. With optimized growth parameters and fabrication processing we have achieved AlN nanowire LEDs with emission at ~ 210 nm.

5.2.1 Growth of Nanowire LEDs

Our III-nitride nanowires are grown by catalyst-free (PAMBE) under nitrogen rich conditions. MBE has the advantage of growing high purity material with atomically smooth surfaces. Also, due to the absence of any foreign metal catalyst, catalyst-free MBE offers the advantage of increased material purity. In PAMBE [116], RF plasma is used to create atomic nitrogen (N) species from nitrogen molecule (N₂). The MBE growth conditions, such as growth rate, III/V flux ratio and substrate temperature determine the final length, diameter and shape of the grown nanowires together with their density and uniformity [117, 118].

The nanowires discussed in this chapter are grown by the Veeco Gen II MBE system equipped with a RF plasma assisted nitrogen source. The three main vacuum chambers in this MBE system are an introduction chamber, a buffer chamber, and a growth chamber. After removing the native oxide on the surface of the silicon wafers in HF acid, they are loaded into the introduction chamber and subsequently transferred to the buffer and growth chamber upon proper degassing. Group III elements (In, Ga, Al) reside in the effusion cells which are thermally evaporated by heating the effusion cells. The nitrogen source in the system is provided by plasma assisted radio frequency excitation. The group III fluxes and the amount of N plasma are controlled by changing the effusion cell temperatures and adjusting the plasma power and nitrogen flow rate, respectively. Once the effusion cells are heated, the group III atoms impinge on the substrate surface to react with the active nitrogen to create the III-nitride materials. Figure 5.1(a) shows the SEM image of the grown nanowires. Also the PL from the grown AlN nanowires is shown in Fig. 5.1(b).

The *p-i-n* LEDs are grown on heavily Si-doped GaN template on *n*-Si substrate. The thickness of the GaN template layer is 80 nm. This layer is followed by a 90 nm Si-doped AlN, a 60 nm non-doped AlN, and a 15 nm Mg-doped AlN layers. A thin 10 nm AlGaN layer is deposited at the top as the contact layer as shown in the Fig. 5.2 (a). The Al nominal concentration is calculated to be 20% by the Al/(Al + Ga) flux ratio. For the AlN LED, the Si cell temperature is 1250 0 C and the Mg-cell temperature is 280 0 C, which results in a Mg concentration of 1 × 10²¹ cm⁻³.

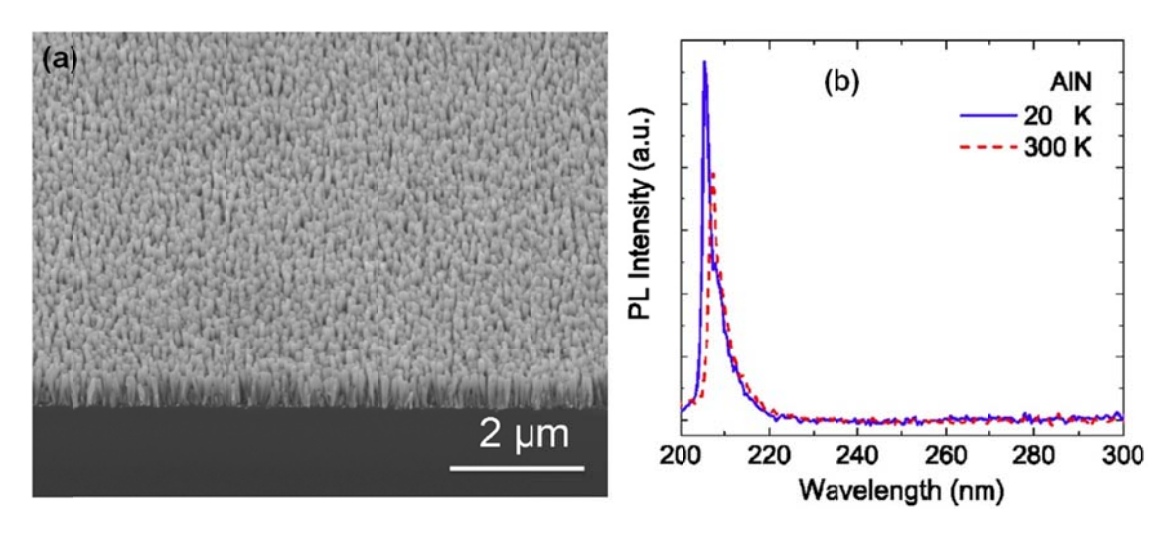


Figure 5.1 (a) SEM image of AlN/GaN nanowires grown on Si substrate. (b) PL spectra taken from AlN:Mg nanowires at room temperature and low temperature with an excitation of 1 mW [119].

5.2.2 Fabrication Procedure and Characterization

The AlN LED fabrication starts with e-beam evaporation of Ti (10 nm)/ Au (30 nm) and Ni (15 nm)/ Au (15 nm) as back and top metal contacts. The top metal contact is deposited at 30 degree angle. This is due to the fact that normal top contact deposition would cover the sidewall of the grown nanowire structures providing a current path between the p-doped and the n-doped parts of the nanowire which results in circumventing the active region and thus short-circuits the LED. Tilted angle deposition prevents the deposition of metal on the nanowire sidewalls by the ballistic shadowing effect [120]. Another way to prevent the short-circuit issue is to use a suitable dielectric passivation material which can be spin coated and therefore fill the gap between nanowires and protect the sidewalls. This processing step is common in white nanowire

LED device fabrication [114] in which polyimide or other polymers is employed as the passivation material. However, these polymers have poor optical transmission in the UV range and therefore, cannot be used for UV nanowire LED devices. A new passivation polymer material, suitable for UV LED devices will be introduced later in this chapter. The schematic of the fabricated devices is illustrated in Fig. 5.2 (b).

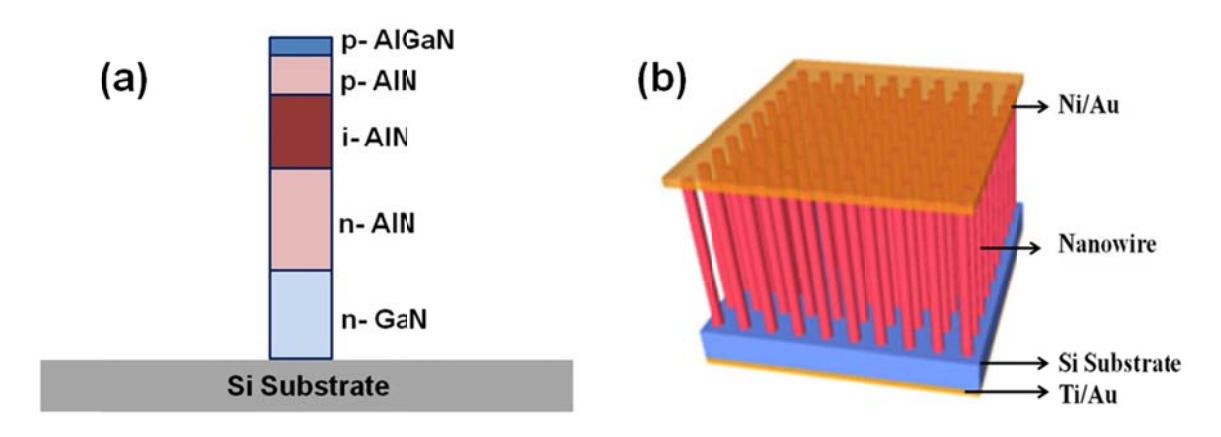


Figure 5.2 (a) Schematic diagram of the AlN *p-i-n* LED on GaN template on Si substrate. (b) Schematic diagram of the fabricated UV LED.

The I-V characteristic of the fabricated UV LED is presented in Fig. 5.3(a). The device shows a turn on voltage of ~ 6 V, which is close to the band gap energy of AlN. The operating voltage at 20 mA injection current is ~ 8 V which is considerably below the turn on voltage of ~ 20 V for the first AlN planar LED emitting at 210 nm, with an operating voltage of 45 V at 20 mA [121]. The high turn-on voltage and high resistance of planar devices are mainly originated from the poor material quality and inefficient impurity doping. However, our nanowire AlN UV LEDs [119] exhibit a significantly enhanced material quality and controllable impurity doping. This is further evidenced from the room temperature current dependent EL spectra presented in Fig. 5.3(b). A clear band edge emission at ~ 210 nm is observed in Fig. 5.3(b).

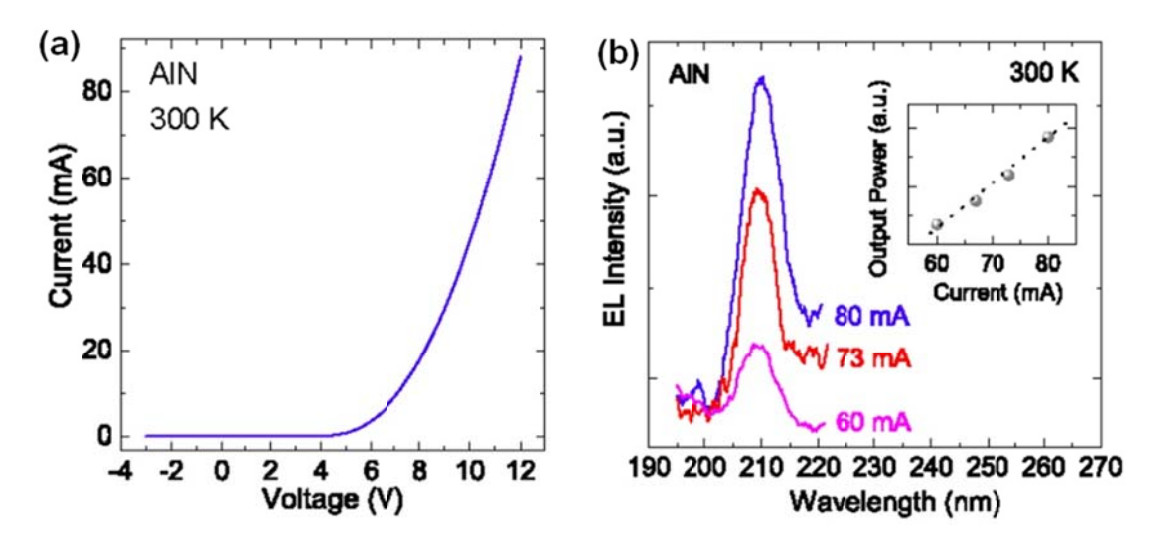


Figure 5.3 (a) The I-V characteristics of AlN LEDs. (b) The EL spectra of AlN LEDs under different injection levels measured at room temperature with the inset showing the output power as a function of current [119].

The diameter of nanowires and the spacing between them can change the efficiency of the UV NW LEDs. In the case of visible LEDs, TE modes are dominant and the light propagates mainly in the top direction. On the other hand, the light is mostly propagating in the horizontal direction for TM modes in the deep UV LEDs, which severely limits the light extraction efficiency of a conventional surface-emitting LED. Moreover, the light extraction efficiency is further limited by the strong total internal reflection at the semiconductor/air interface. The variation of external quantum efficiency with nanowire diameter has been calculated using simulation by changing the NW diameter from 98 to 130 nm which changes the light extraction efficiency from 8% to 72% for TM modes [122] as shown in Fig 5.4 (a). Compared to small nanowires which cannot support the coupled modes, the large nanowires could locally resonate and confine light inside the structure. Also Fig. 5.4 (b) shows the light extraction efficiency as a function of the spacing between nanowires from 163 to 203 nm with nanowire diameter of 119 nm. It is shown that when the spacing between nanowires is small light can be trapped in the space between the nanowires which results in decrease of light extraction efficiency. However, by increasing the spacing, light could propagate horizontally through the nanowires for TM mode due to the formation of coupled modes. Therefore, NW LEDs can show high

extraction efficiencies. However, the extraction mechanism is different for large spacing nanowires where light could propagate through the space between nanowires [122].

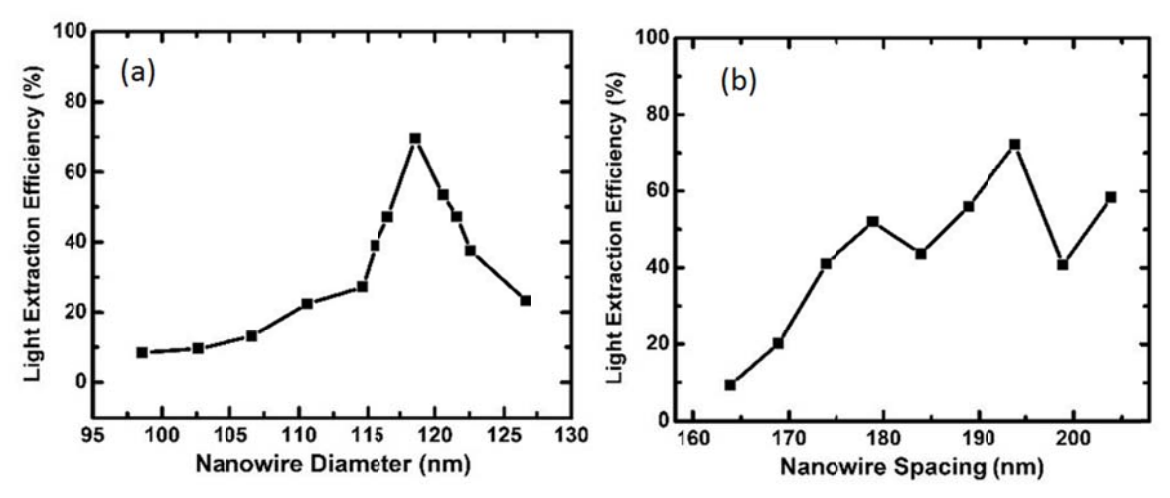


Figure 5.4 (a) Variations of the light extraction efficiency with nanowire diameter. (b) Variations of the light extraction efficiency with nanowire spacing.

5.3 Passivation Polymer Material for UV Nanowire LEDs

As discussed previously, there is an urgent need for a new polymer material for passivation and planarization step in nanowire UV LED fabrication process. In this regards, we have studied the characteristics of a synthetic polymer called "Polyisobutylene". This type of polymer is solved in "Toluene" solvent. To use this material for passivation of nanowire LEDs, first we optimized the spin coating parameters to ensure about the uniformity of the spin coated material. After spin coating, the extra polymer sitting on the nanowire tips should be dry etched –usually using O₂ plasma RIE- to the point that the nanowire tips are exposed and ready for top contact deposition. Therefore, it is important to be able to control the thickness of the polymer by spin coating parameters e.g. rotation speed (rpm), rotation time and material's concentration. For the same reason, uniformity of the coated material is too, of great concern. If the final coated polymer is uneven, the sidewall of nanowires with less coated polymer will be exposed to contact deposition resulting in short-circuiting of the corresponding nanowires. We have optimized the concentration (mg/mL), spinning speed (rpm) and coating time (sec) for polyisobutylene solved in toluene in order to get a linear dependence of the final thickness with the material concentration. Moreover, the samples

were prepared on silicon wafers, and the thickness of the coated polymer was measured using ellipsometry.

It is necessary to keep a relatively high spin-coating speed ~ 4000 rpm in order to ensure the coating uniformity. However, at such high spin-coating speeds, the thickness of the material becomes relatively thin and is not sufficient to cover the height of the nanowire device. To increase the thickness of the material at high spin-coating speeds, we have increased the concentration of the coated polymer and thus we could achieve both good uniformity and controlled thickness. Since the solution process for this polymer is performed manually, the constant stirring of the solution should be continued prior to spin coating, in order to ensure about the consistency of the fluid. Figure 5.5 shows the nearly linear dependence of the final film thickness on material concentration.

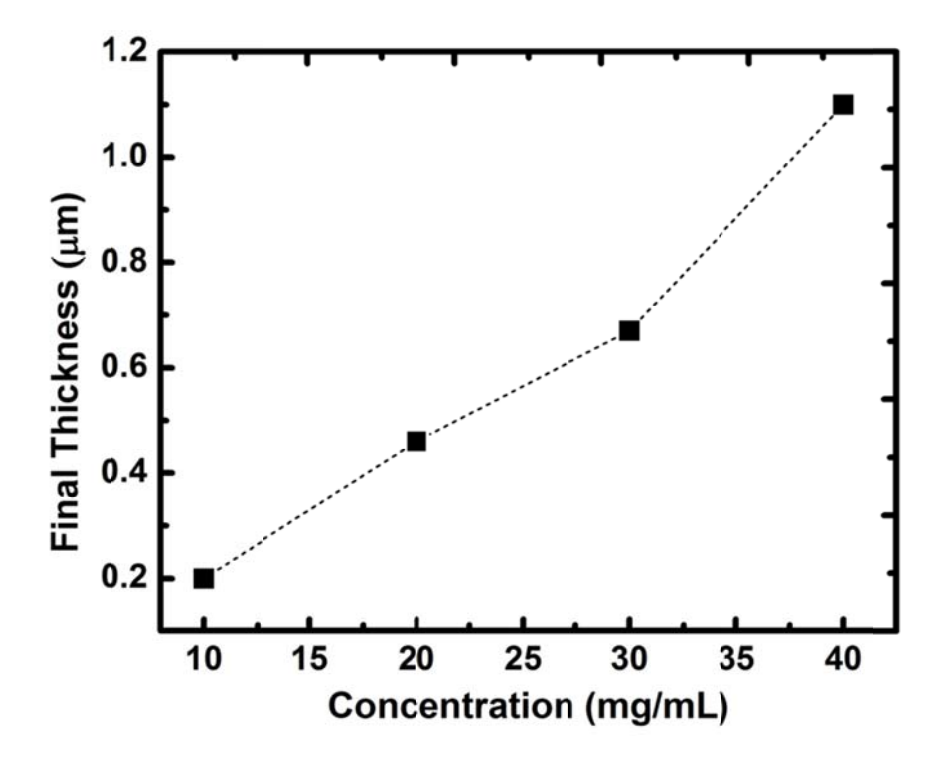


Figure 5.5 Final thickness of the spin-coated polyisobutylene/toluene solution measured on silicon wafer using ellipsometry versus the solution concentration. The solution was spin coated for 65 sec at 4000 rpm.

In order to measure the absorption spectrum of polyisobutylene/toluene solution we spin coated the material on a sapphire piece with ~ 38 mg/mL concentration to obtain ~ 1 μ m of coated polymer, shown in Fig. 5.4. Another sample with the same thickness of

polyimide was also prepared for comparison. The absorption spectrum measurements were performed using a Beckman DU640 UV/VIS spectrophotometer.

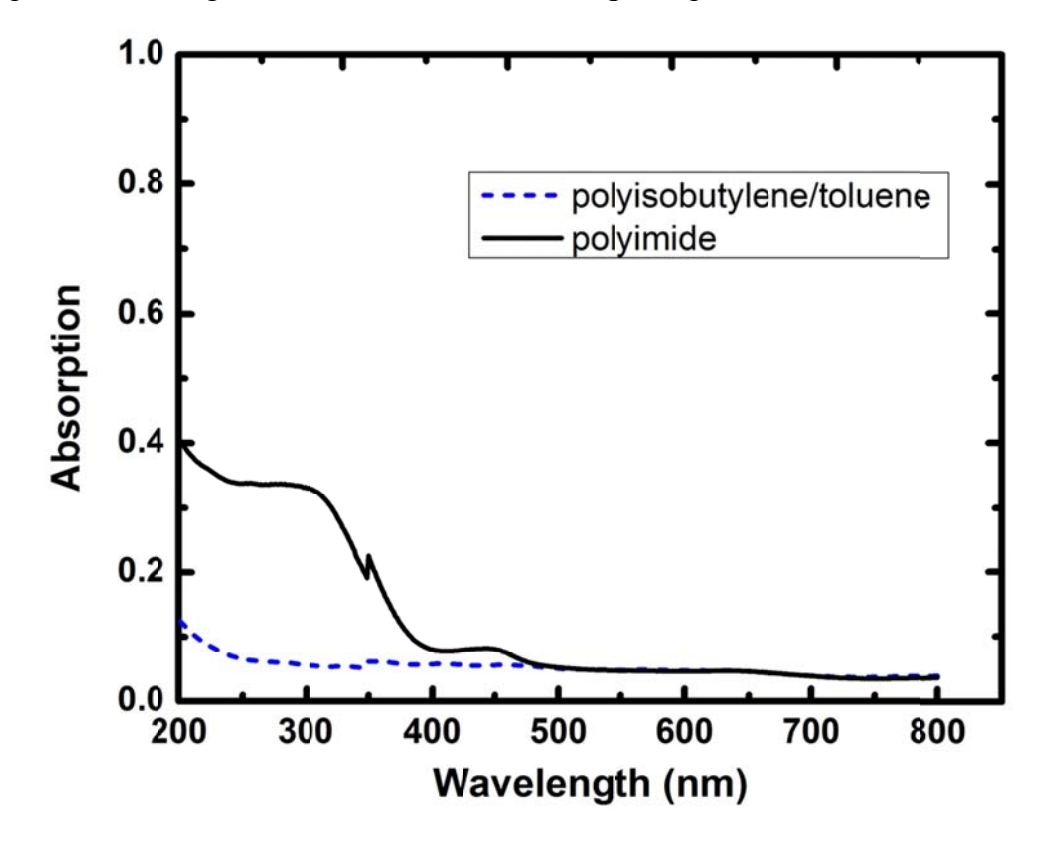


Figure 5.6 Absorption spectrum for spin-coated polyisobutylene/toluene and polyimide coatings with $\sim 1 \mu m$ thickness.

In the 200-350 nm wavelength range, the absorption of polyisobutylene/toluene coated material is much lower than that of polyimide as shown in Fig. 5.6. Therefore, polyisobutylene/toluene can be used in the passivation and planarization of UV nanowire LEDs.

5.4 Conclusion

In summary we have achieved, for the first time, AlN p-i-n nanowire LED emitting at \sim 210 nm with good electrical characteristics. The device has a low turn-on voltage of \sim 6 V, and a clear band-edge emission is observed at \sim 210 nm which outperforms the planar AlN LEDs. We also have introduced a new passivating polymer material with low absorption in the 200-350 nm wavelength range which is compatible with light emitting devices working in the UV range.

Chapter 6. Conclusions and Future Works

6.1 Conclusions

In this thesis we have demonstrated InP-based rolled-up microtube lasers at telecom wavelength range embedding quantum dots/dashes/wells with both optical and electrical pumping. In addition we have shown quantum dot infrared tube photodetectors that can be utilized for the emerging Si-based chip-level optical communications. Moreover, we have demonstrated the first AlN nanowire UV LED devices with emission at ~ 210 nm which outperform their planar structure LED counterparts. The significant findings of this thesis are summarized below.

There is an urgent requirement for a compact and efficient light source to complete the toolbox for photonics integrated communication systems. Rolled-up microtubes offer unique characteristics such as directional emission and polarization control, relatively straightforward fabrication process and the possibility of transferring onto other substrates including Si. These properties have defined this class of microcavity structures as competitive candidates among different types of microcavities as potential light sources for future chip-level optical communication systems.

In this regard, we have initially achieved the first demonstration of InAs/InGaAsP QD tube laser devices that operate at ~ 1470 nm at 80 K [94]. These devices show a threshold of $\sim 1.26~\mu W$ and Purcell factor of ~ 4.8 . Subsequently, with further improvement of the device fabrication, we demonstrated the first room temperature InAs/InGaAsP quantum dash lasers with close to 100% fabrication yield [60]. These lasing devices operate in the telecommunication wavelength range with emission at $\sim 1590~nm$. The measured threshold of these devices was $\sim 6~\mu W$ with the Purcell factor of ~ 6.54 .

Although the demonstrated optically-pumped rolled-up tube lasers show a great leap forward towards integrated photonic light sources, their practical utilization in such systems may be challenging considering the requirement of another optical pumping source. The ideal type of an integrated chip-level light source component would be an electrically driven device in which the excitation of the embedded active material is triggered by injecting the carriers through on-chip biasing of the device. To this end, we

have investigated the design, fabrication and characterization of electrically injected InP/InGaAsP quantum well rolled-up tube light sources with embedded InGaAs active material. We have further achieved, for the first time in the world, electrically injected lasing from such devices operating at \sim 1485 nm measured at 80 K [112]. A lasing threshold of \sim 1.05 mA was measured for a rolled-up tube with a diameter of \sim 5µm and wall thickness of \sim 140 nm. Such nanoscale devices can be further integrated with Sibased nanophotonic circuits for applications in ultrahigh-speed, ultralow power chip-level optical communications.

In addition to efficient and compact light sources, the emerging field of chip-level optical communications and interconnects also requires highly sensitive, Si-integrated infrared photodetectors. The device performance of Ge and III-V based photodetectors grown directly on Si has been limited due to incompatibilities in the growth parameters. On the other hand, QD photodetectors show unique characteristics such as high temperature operation, reduced dark current and tenability of the operation wavelength by engineering the size and composition of the QDs. In this thesis, we have demonstrated a novel rolled-up InAs QD tube photodetectors, wherein the light absorption length and charge carrier transport can be separately optimized, promising both ultra-high-speed and high-efficiency operation [72]. The device responsivity at 300 K is measured to be ~0.066 A/W at 1064 nm with an external QE of ~8%. The QE of such devices can also be increased considerably by increasing the number of embedded QD layers in the device heterostructure.

Also, in this thesis we have studied the fabrication and device passivation of UV LEDs based on direct bandgap III-nitride nanowires that are grown on Si substrate using MBE. Poor crystal quality due to the lack of suitable substrates, difficulties in impurity doping and low light extraction efficiency are among the main problems to overcome in order to achieve high performance DUV LEDs. Compared to III-nitride planar structures, III-nitride nanowires offer the possibility of growing dislocation-free crystals on a foreign substrate and therefore are considered as promising candidates for optoelectronic devices such as LEDs and lasers. By optimizing the growth conditions, we have realized AlN *p-i-n* LEDs. We have demonstrated the device fabrication and characterization of such LEDs

emitting at DUV range (\sim 210 nm) which show a low turn-on voltage of \sim 6 V [119] that outperform the planar AlN LEDs. Another important challenge in the fabrication of such devices is the search for a suitable passivation material that is highly transparent in the DUV range. In this regard, we have addressed the problem of passivating the UV nanowire LEDs by introducing a new polymer-based synthetic material, polyisobutylene. We have performed detailed studies on the processing parameters and transmission properties. We have shown that such a polymer material can be used in the fabrication of UV nanowire light emitting devices such as LEDs and lasers due to its low optical absorption in the 200-350 nm wavelength range.

6.2 Future Works

6.2.1 SiO_x Rolled-up Microtubes

As previously described, the resonance modes in WGM resonators with sub-wavelength wall thicknesses are highly sensitive to optical perturbations outside their structure such as very small changes in the refractive index of their environment. This characteristic makes WGM resonators interesting candidates for applications in biosensors. Also for integrated biosensor devices in practical applications, Si-based ring resonator sensors are preferred due to their compatibility with main stream microelectronics. One interesting application of microtube-based biosensors is to detect certain microorganisms such as viruses or bacteria. Certain types of large molecules, such as proteins are always present on the body of such microorganisms. These types of molecules are referred to as antigens. The immune system of human body naturally responds to the presence of any type of antigens by producing specific substances called antibodies. For every type of antigen there exists a unique type of antibody. Each type of antibody has a unique bonding site shape which only locks to the specific shape of its corresponding antigen, thereby forming an antigen-antibody complex. To use the microtube bisosensor devices to detect certain type of microorganism, the surface of the tube is covered with the corresponding type of antibody. This is called the activation step. This type of antibody will then attract the target antigen and bind to it which in turn causes the accumulation of bound protein on the surface of the microtube and increases the total diameter of the tube.

Increasing the tube diameter will in turn change the position of the WGM resonant wavelength. Therefore, the existence of particular microorganisms such as HIV virus can be detected. SiO_x surfaces are interesting material options for this purpose since they have similar dielectric properties as the condensed protein layers. Microsphere and microtoroid WGM biosensors based on this principle have been reported [67, 123]. In order to prepare such platforms based on microtube structures, that potentially could have numerous applications in biosensors and beyond, we have developed a new fabrication method to create SiO_x rolled-up microtubes on any arbitrary substrate.

The fabrication of these devices starts with e-beam deposition of 50 nm Ge sacrificial layer on the arbitrary substrate, e.g. Si. Standard photolithography and e-beam deposition of SiO (5nm)/SiO₂ (25 nm) followed by the subsequent lift-off is performed to create U-shaped or rectangular mesas of SiO_x bilayer material on Ge sacrificial layer. Later, the sample is subsidized in 90 °C hydrogen peroxide solution for 2 minutes which undercuts the Ge sacrificial layer leading to formation of the SiO/SiO₂ rolled-up tube structures as shown in Fig. 6.1.

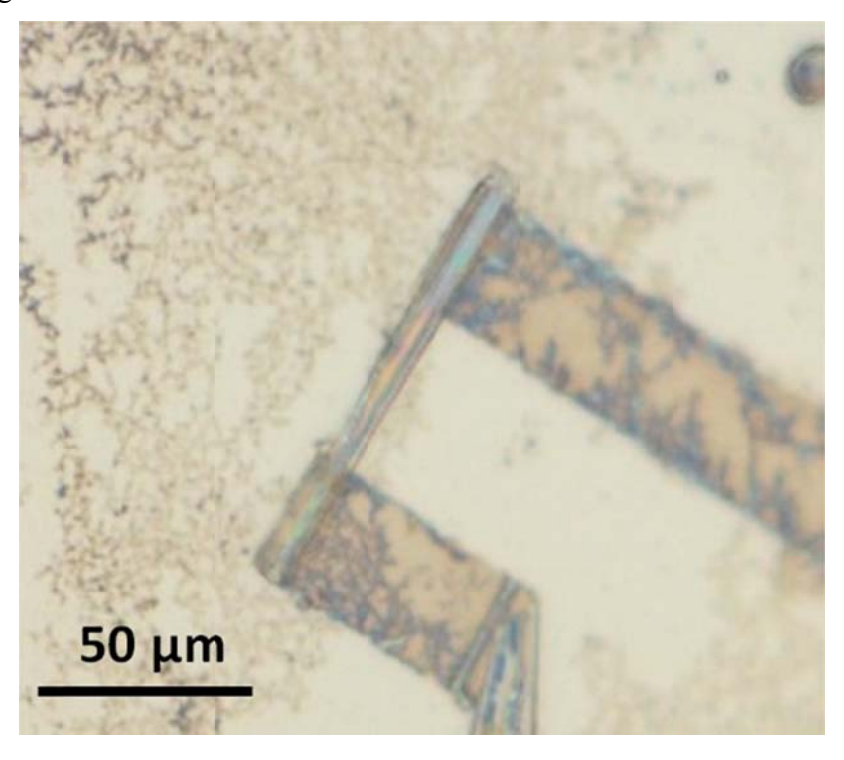


Figure 6.1 SiO/SiO₂ rolled-up tube on Si substrate.

As any other strain driven rolled-up tube structure, the diameter of such devices is determined by the bilayer thicknesses and also the internal strain. For the aforementioned SiO/SiO_2 bilayer thicknesses, the tube has a diameter of $\sim 5-6 \mu m$.

A critical condition in the formation of SiO_x tubes is the smoothness of the layer on which SiO/SiO₂ bilayer is deposited. This is even more important when the sacrificial material is not an epilayer. For instance, SiO_x tubes using photoresist sacrificial layers have been reported on glass substrates [66]. Different photoresists were selected to choose the one with the smoothest surface employing AFM measurements. We have also fabricated SiO_x tubes using InGaAsP as the sacrificial layer on InP substrate. Using photolithography and e-beam deposition of SiO (5 nm)/ SiO₂ (25 nm) on InGaAsP in the form of U-shaped mesas, we immersed the sample inside HCl:HNO₃:H₂O (1:2:10) for 15 minutes to undercut the InGaAsP layer after which the SiO/SiO₂ tube structures were formed as shown in Fig. 6.2.

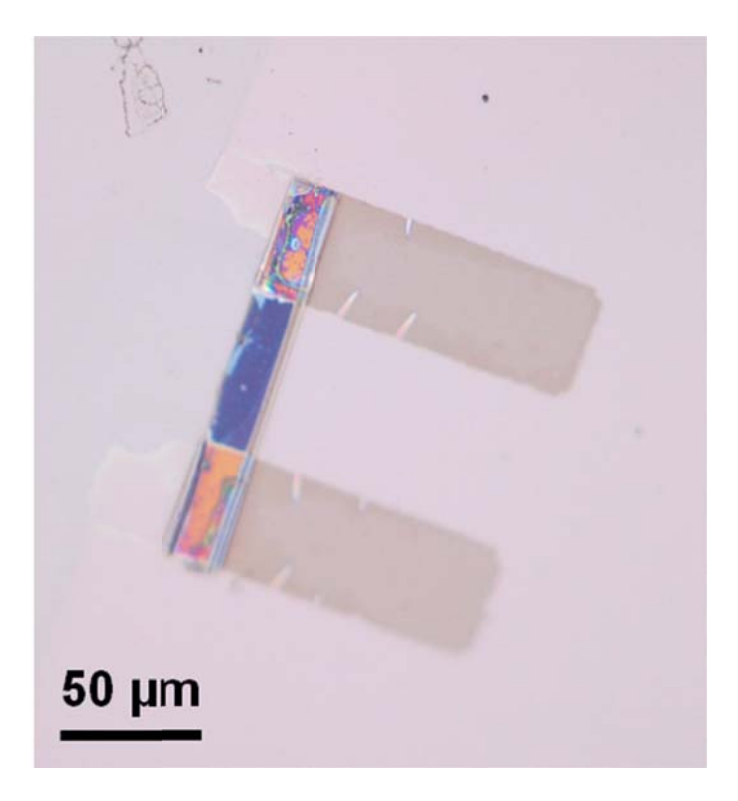


Figure 6.2 SiO/SiO₂ rolled-up tube using InGaAsP sacrificial layer.

The work is currently in progress in order to utilize these types of tubular structures in microfluidic devices used for point-of-care diagnosis applications. Another class of tube

biosensors can be used for the detection of microorganisms due to the assumption that forming antigen-antibody complex causes charge disturbance on the surface of the activated microtube. Therefore, detection of the microorganism can be done by passing a current through the activated tube structure and monitoring the change in the current by introducing the corresponding antigen to the system. In contrast to the first method, this technique can be used in point-of-care diagnosis.

6.2.2 III-N Rolled-up Tubes

Rolled-up microtube devices have been reported out of many semiconductors, including dielectrics and polymer materials for different applications [34-37, 39, 94]. However, they have not been demonstrated for all types of III-V materials including III-Nitride structures. Since emission from different types of III-N materials covers the whole solar spectrum from UV to IR, the realization of III-N rolled-up tubes can be interesting for LEDs and laser applications. As discussed previously, due to the lack of suitable substrates for the growth of III-N materials, the grown epilayers contain a considerable number of defects and dislocations. These dislocations act as non-radiative recombination centers for optoelectronic devices and lead to degradation of the device's performance. However, if III-N epilayers roll up into tubular structures and thereby leave the host Si substrate due to strain release associated with the rolling mechanism, the amount of dislocations should decrease. Furthermore, the number of defects could be decreased even more through an additional annealing step of the tubular structure. In addition to low defect density, rolled-up tubes also offer high integration densities when used as electronic devices, thanks to their cylindrical structures and circular cross sections.

They can also increase the light extraction efficiency of the optoelectronics devices. For example, simulation results have been reported [124] that show increase in light extraction efficiency of GaN LEDs using GaN nanotube structure placed on top of the planar LED structure as shown in Fig. 6.3 (a). The nanotube has a wall thickness that is well below the wavelength of the optical mode and therefore has a small refractive index that matches the refractive index between bulk GaN and air. This results in enhancement of the light extraction from LEDs by coupling the guided modes in the bulk structure into the leaky modes of the nanotube as shown in Fig. 6.3 (b) and Fig. 6.3 (c) [124].

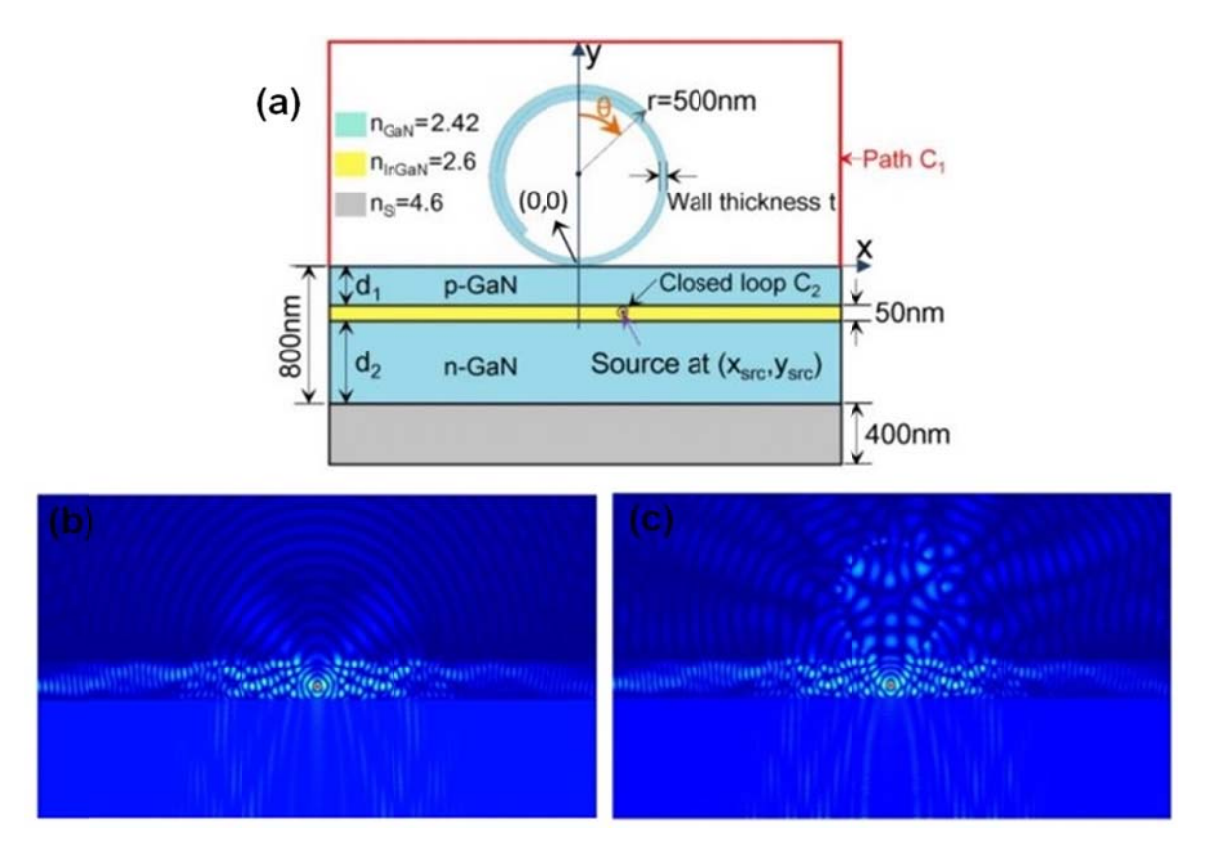


Figure 6.3 (a) Schematic of GaN LED and nanotube structures. Snapshot of the time domain simulation showing the electrical field pattern of the structure: (b) without nanotube and (c) with nanotube [124].

So far, only rolled-down AlN/GaN tube structures on Si have been demonstrated [125] due to the smaller lattice constant of AlN compared to GaN. The fact that those tubes are in complete contact with the underlying substrate, makes it difficult to use them as suitable platforms for light emitting devices due to high optical loss in the substrate. One possible way to fabricate a III-N rolled-up tube is by growing AlN on top of Si-based GaN layer, which should create some strain between the Si substrate and the top GaN layer. This strain then should be released by forming the tubular structure once the underlying Si substrate is removed.

6.2.3 Incorporation of other Active Materials for Microtube Light Sources

Rolled-up microtube device is a special type of WGM microcavity with unique characteristics that were discussed in section 1.2.3, including directional emission and

polarization control. The incorporation of the active material inside the heterostructure of tube devices is usually done during the growth of the material layer structure. However, the choice of such embedded active materials is limited by the growth conditions which then limit their operating wavelengths. Although some wavelength tuning is possible by engineering the size and composition of the active material but it cannot largely change the emission wavelength. Thus being able to incorporate other "foreign" active materials inside the tube structures to couple with the resonance modes of the microtube is a promising solution.

Injection of active material inside the tubular cavity is one way to achieve this goal. Filling a GaAs-based microtube using a micropipet and a syringe with PbS NCs (with emission at around 953 nm at 7 K) which were dispersed in a toluene solution has been reported [93]. However, this process needs an additional micro positioning system for the injection process and therefore is not very practical.

On the other hand, the rolling nature of tube devices immediately suggests entrapping active material during the rolling process which will result in embedding them within the microcavity structure. This can include dispersed NW devices such as $In_xGa_{1-x}N$ NWs, colloidal semiconductor quantum dots or 2-dimensional semiconductor flakes such as MoS_2 [126], WS_2 [127], etc. In contrast to 2-D semiconductor single layer flakes and colloidal QDs [128], that practically have negligible thicknesses, incorporation of dispersed NWs, can potentially have an adverse effect on the cavity formation, due to their comparable length and diameter to the tube's wall thicknesses. To demonstrate this, we have dispersed long ($\sim 4\mu m$) and short (~ 100 nm) InN nanowires onto GaAs-based heterostructures discussed in chapter 3, prior to tube formation. Long InN NWs have drastically hindered the tube formation resulting in deformation and breakage of the tube device as shown in Fig. 6.4 (a). The effect is less severe for shorter InN NWs seen in Fig. 6.4 (b).

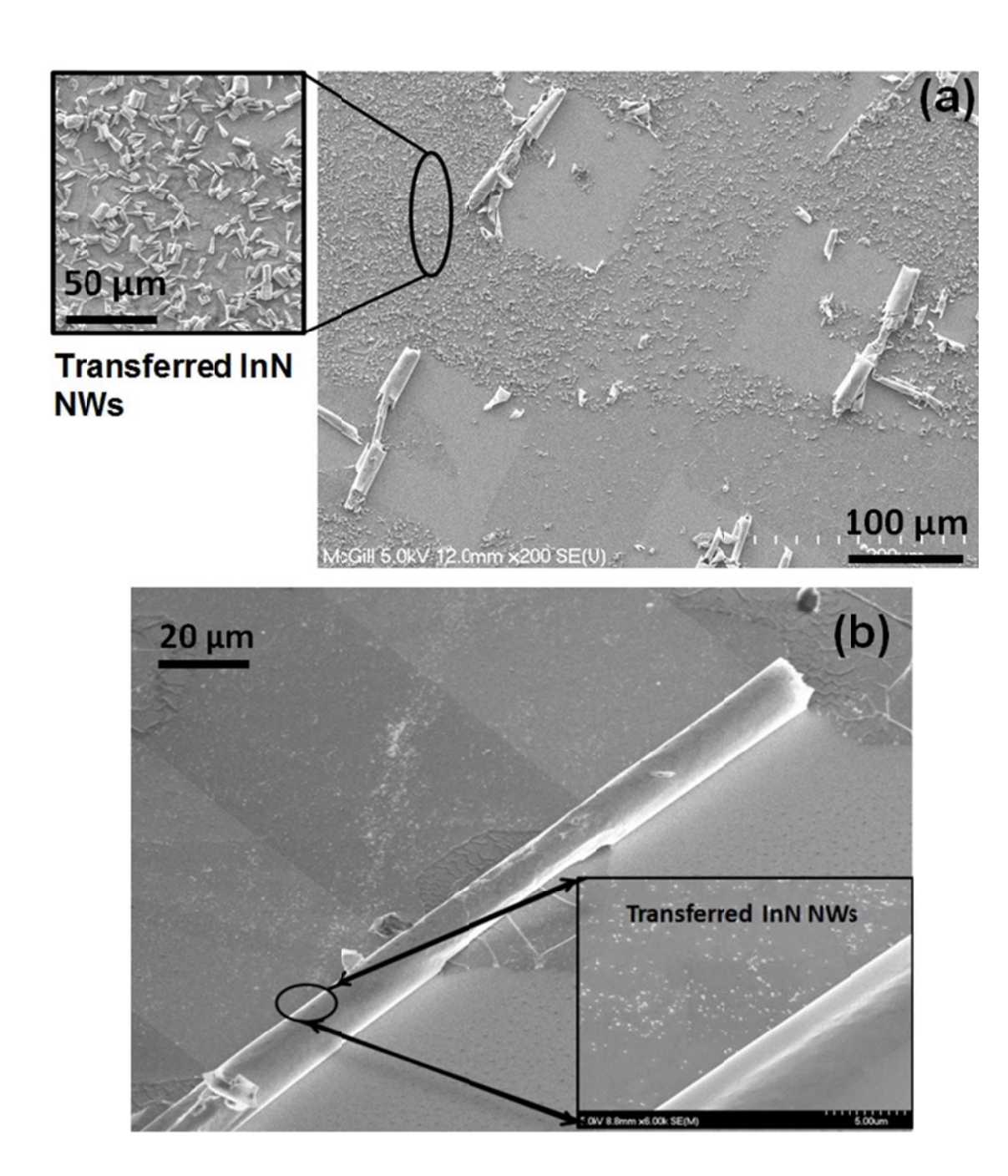


Figure 6.4 (a) Rolled-up GaAs-based microtubes embedding long InN NWs. The devices are mostly broken during rolling due to large dimensions of the NWs. (b) Rolled-up GaAs-based microtubes embedding short InN NWs.

Such devices should in principle perform as optically pumped light sources. It is also important to avoid light absorption by the tube's walls by considering the energy gap of the active material and also the tube's body material. For instance, GaAs/InGaAs tubes

shown in the Fig 6.4 are compatible with InN NWs since this material system does not absorb the emission from InN wires with wavelengths of $\sim 1.8~\mu m$. However, in the case of monolayer two-dimensional materials such as MoS_2 and WS_2 with emission wavelengths of $\sim 600\text{-}700$ nm, the GaAs/InGaAs material system is not suitable. On the other hand, SiO_x tube systems discussed before will be almost transparent in the visible range and could be used.

6.2.4 Room Temperature Electrically Injected Rolled-up Lasers and Photodetectors

In Chapter 4 we have described the electrically injected InGaAs QW tube lasers at 80 K. However, a more practical device should preferably operate at room temperature which circumvents the need for cryogenic cooling. As discussed in section 4.4, strong coherent emission from electrically-injected tube devices at room temperature is considerably limited by large surface recombination velocities associated with GaAs and related materials. Also the fabrication yield for these devices is still low and should be enhanced. Increasing the number of InGaAs QW active layers in the device heterostructure should increase the optical gain and possibly enhance the performance of the devices.

Moreover, rolled-up tube photodetectors with InGaAs QWs could be used as photodetectors in the telecom wavelength range. The fabrication of such devices is similar to the described tube laser. Increasing the number of active layers in such devices should result in increased absorption of the incoming light and therefore increase the responsivity and quantum efficiency of such devices. Considerable increase in the quantum efficiency is also expected by increasing the number of QD layers for the InAs-GaAs QD photodetectors discussed in Chapter 3.

As discussed in section 1.2.2 successful transferring of our III-V rolled-up tubes has been already demonstrated. However, a more interesting and challenging approach would be to grow the III-V layers directly on Si. Growth and fabrication of GaAs tubes directly on Si has been demonstrated recently [129]. Using a multistep MOCVD growth method a 2 μ m GaAs metamorphic epilayer was grown on Si as the buffer layer, on top of which AlAs sacrificial layer and GaAs/InGaAs strained bilayer were grown subsequently. Being able to directly grow such III-V heterostructures on Si would ideally address the integration

concerns for such micro/nano scale optoelectronics devices that have been demonstrated in this thesis to be practical candidates as light sources and photodetectors for future chiplevel optical communication systems.

Bibliography

- [1] D. A. Miller, "Optical interconnects to electronic chips," *Applied Optics*, vol. 49, pp. F59-F70, 2010.
- [2] R. Ho, K. W. Mai, and M. A. Horowitz, "The future of wires," *Proceedings of the IEEE*, vol. 89, pp. 490-504, 2001.
- [3] J. A. Davis, R. Venkatesan, A. Kaloyeros, M. Beylansky, S. J. Souri, K. Banerjee, et al., "Interconnect limits on gigascale integration (GSI) in the 21st century," *Proceedings of the IEEE*, vol. 89, pp. 305-324, 2001.
- [4] J. D. Meindl, "Interconnect opportunities for gigascale integration," *IEEE Micro*, vol. 23, pp. 28-35, 2003.
- [5] D. A. B. Miller and H. M. Ozaktas, "Limit to the bit-rate capacity of electrical interconnects from the aspect ratio of the system architecture," *Journal of parallel and distributed computing*, vol. 41, pp. 42-52, 1997.
- [6] K. C. Saraswat and F. Mohammadi, "Effect of scaling of interconnections on the time delay of VLSI circuits," *Solid-State Circuits, IEEE Journal of*, vol. 17, pp. 275-280, 1982.
- [7] M. Haurylau, G. Chen, H. Chen, J. Zhang, N. A. Nelson, D. H. Albonesi, *et al.*, "On-chip optical interconnect roadmap: challenges and critical directions," *Selected Topics in Quantum Electronics, IEEE Journal of,* vol. 12, pp. 1699-1705, 2006.
- [8] V. Prinz, V. Seleznev, A. Gutakovsky, A. Chehovskiy, V. Preobrazhenskii, M. Putyato, *et al.*, "Freestanding and overgrown InGaAs/GaAs nanotubes, nanohelices and their arrays," *Phys. E*, pp. 828–831, 2000.
- [9] J. Wu, "When group-III nitrides go infrared: New properties and perspectives," *Journal of Applied Physics*, vol. 106, p. 011101, 2009.
- [10] Z. Yarar, "Transport and mobility properties of wurtzite InN and GaN," *physica status solidi (b)*, vol. 244, pp. 3711-3718, 2007.
- [11] S. Strite and H. Morkoç, "GaN, AlN, and InN: a review," *Journal of Vacuum Science & Technology B*, vol. 10, pp. 1237-1266, 1992.
- [12] A. G. Bhuiyan, A. Hashimoto, and A. Yamamoto, "Indium nitride (InN): A review on growth, characterization, and properties," *Journal of Applied Physics*, vol. 94, pp. 2779-2808, 2003.
- [13] M. Van Schilfgaarde, A. Sher, and A.-B. Chen, "Theory of AlN, GaN, InN and their alloys," *Journal of crystal growth*, vol. 178, pp. 8-31, 1997.
- [14] I. Vurgaftman, J. Meyer, and L. Ram-Mohan, "Band parameters for III–V compound semiconductors and their alloys," *Journal of applied physics*, vol. 89, pp. 5815-5875, 2001.
- [15] D. A. Miller, "Device requirements for optical interconnects to silicon chips," *Proceedings of the IEEE*, vol. 97, pp. 1166-1185, 2009.
- [16] R. G. Beausoleil, P. J. Kuekes, G. S. Snider, S.-Y. Wang, and R. S. Williams, "Nanoelectronic and nanophotonic interconnect," *Proceedings of the IEEE*, vol. 96, pp. 230-247, 2008.

- [17] D. A. Miller, "Optical interconnects to silicon," *Selected Topics in Quantum Electronics, IEEE Journal of*, vol. 6, pp. 1312-1317, 2000.
- [18] "International technology roadmap for semiconductors."
- [19] D. A. Miller, "Physical reasons for optical interconnection," *International Journal of Optoelectronics*, vol. 11, pp. 155-168, 1997.
- [20] A. Shacham, K. Bergman, and L. P. Carloni, "Photonic networks-on-chip for future generations of chip multiprocessors," *Computers, IEEE Transactions on*, vol. 57, pp. 1246-1260, 2008.
- [21] D. A. Miller, "Optics for low-energy communication inside digital processors: quantum detectors, sources, and modulators as efficient impedance converters," *Optics Letters*, vol. 14, pp. 146-148, 1989.
- [22] M. Lončar, T. Yoshie, A. Scherer, P. Gogna, and Y. Qiu, "Low-threshold photonic crystal laser," *Applied Physics Letters*, vol. 81, pp. 2680-2682, 2002.
- [23] R. Chen, T.-T. D. Tran, K. W. Ng, W. S. Ko, L. C. Chuang, F. G. Sedgwick, *et al.*, "Nanolasers grown on silicon," *Nature Photonics*, vol. 5, pp. 170-175, 2011.
- [24] D. Liang, M. Fiorentino, T. Okumura, H.-H. Chang, D. T. Spencer, Y.-H. Kuo, *et al.*, "Electrically-pumped compact hybrid silicon microring lasers for optical interconnects," *Optics Express*, vol. 17, pp. 20355-20364, 2009.
- [25] J. Van Campenhout, P. Rojo Romeo, P. Regreny, C. Seassal, D. Van Thourhout, S. Verstuyft, *et al.*, "Electrically pumped InP-based microdisk lasers integrated with a nanophotonic silicon-on-insulator waveguide circuit," *Optics Express*, vol. 15, pp. 6744-6749, 2007.
- [26] F. Li and Z. Mi, "Optically pumped rolled-up InGaAs/GaAs quantum dot microtube lasers," *Optics express*, vol. 17, pp. 19933-19939, 2009.
- [27] C. Deneke, C. Müller, N. Jin-Phillipp, and O. Schmidt, "Diameter scalability of rolled-up In (Ga) As/GaAs nanotubes," *Semiconductor science and technology*, vol. 17, p. 1278, 2002.
- [28] I. S. Chun and X. Li, "Controlled assembly and dispersion of strain-induced InGaAs/GaAs nanotubes," *Nanotechnology, IEEE Transactions on*, vol. 7, pp. 493-495, 2008.
- [29] V. Y. Prinz, "A new concept in fabricating building blocks for nanoelectronic and nanomechanic devices," *Microelectronic engineering*, vol. 69, pp. 466-475, 2003.
- [30] R. t. Cottam and G. Saunders, "The elastic constants of GaAs from 2 K to 320 K," *Journal of Physics C: Solid State Physics*, vol. 6, p. 2105, 1973.
- [31] I. S. Chun, A. Challa, B. Derickson, K. J. Hsia, and X. Li, "Geometry effect on the strain-induced self-rolling of semiconductor membranes," *Nano letters*, vol. 10, pp. 3927-3932, 2010.
- [32] T. Kipp, H. Welsch, C. Strelow, C. Heyn, and D. Heitmann, "Optical modes in semiconductor microtube ring resonators," *Physical review letters*, vol. 96, p. 077403, 2006.
- [33] Z. Mi, P. Bianucci, F. Li, Z. Tian, V. Veerasubramanian, A. G. Kirk, *et al.*, "Selforganized InAs quantum dot tube lasers and integrated optoelectronics on Si," in *SPIE OPTO*, 2011, pp. 79431C-79431C-10.
- [34] F. Li, Z. Mi, and S. Vicknesh, "Coherent emission from ultrathin-walled spiral InGaAs/GaAs quantum dot microtubes," *Optics letters*, vol. 34, pp. 2915-2917, 2009.

- [35] R. Songmuang, A. Rastelli, S. Mendach, and O. Schmidt, "SiO x/Si radial superlattices and microtube optical ring resonators," *Applied Physics Letters*, vol. 90, pp. 091905-091905-3, 2007.
- [36] Y. Dror, W. Salalha, R. Avrahami, E. Zussman, A. Yarin, R. Dersch, *et al.*, "One-Step Production of Polymeric Microtubes by Co-electrospinning," *Small*, vol. 3, pp. 1064-1073, 2007.
- [37] V. Luchnikov, M. Stamm, C. Akhmadaliev, L. Bischoff, and B. Schmidt, "Focused-ion-beam-assisted fabrication of polymer rolled-up microtubes," *Journal of Micromechanics and Microengineering*, vol. 16, p. 1602, 2006.
- [38] H. Zhang, J. Peng, Y. Shen, X. Yu, F. Zhang, J. Mei, *et al.*, "Hybrid microtubes of polyoxometalate and fluorescence dye with tunable photoluminescence," *Chemical Communications*, vol. 48, pp. 4462-4464, 2012.
- [39] K. Kumar, B. Nandan, V. Luchnikov, E. B. Gowd, and M. Stamm, "Fabrication of metallic microtubes using self-rolled polymer tubes as templates," *Langmuir*, vol. 25, pp. 7667-7674, 2009.
- [40] D. Paolis and D. Vittorio, "Metallic rings in a self-rolled micro-tube for magnetic field mapping applications," in *The 40th European Microwave Conference*, 2010, pp. 1385-1388.
- [41] C. Giordano, M. Todaro, M. Palumbo, L. Blasi, V. Errico, A. Salhi, *et al.*, "Hybrid polymer/semiconductor microtubes: A new fabrication approach," *Microelectronic engineering*, vol. 85, pp. 1170-1172, 2008.
- [42] K. Tanabe, M. Nomura, D. Guimard, S. Iwamoto, and Y. Arakawa, "Room temperature continuous wave operation of InAs/GaAs quantum dot photonic crystal nanocavity laser on silicon substrate," *Optics express*, vol. 17, pp. 7036-7042, 2009.
- [43] Q.-Y. Tong, R. Scholz, U. Gösele, T.-H. Lee, L.-J. Huang, Y.-L. Chao, *et al.*, "A "smarter-cut" approach to low temperature silicon layer transfer," *Applied Physics Letters*, vol. 72, pp. 49-51, 1998.
- [44] E. Menard, K. Lee, D.-Y. Khang, R. Nuzzo, and J. Rogers, "A printable form of silicon for high performance thin film transistors on plastic substrates," *Applied Physics Letters*, vol. 84, pp. 5398-5400, 2004.
- [45] H.-C. Yuan, J. Shin, G. Qin, L. Sun, P. Bhattacharya, M. G. Lagally, *et al.*, "Flexible photodetectors on plastic substrates by use of printing transferred single-crystal germanium membranes," *Applied Physics Letters*, vol. 94, pp. 013102-013102-3, 2009.
- [46] D.-H. Kim, J.-H. Ahn, W. M. Choi, H.-S. Kim, T.-H. Kim, J. Song, *et al.*, "Stretchable and foldable silicon integrated circuits," *Science*, vol. 320, pp. 507-511, 2008.
- [47] S. Vicknesh, F. Li, and Z. Mi, "Optical microcavities on Si formed by self-assembled InGaAs/GaAs quantum dot microtubes," *Applied Physics Letters*, vol. 94, p. 081101, 2009.
- [48] Z. Tian, F. Li, Z. Mi, and D. V. Plant, "Controlled transfer of single rolled-up InGaAs–GaAs quantum-dot microtube ring resonators using optical fiber abrupt tapers," *Photonics Technology Letters, IEEE*, vol. 22, pp. 311-313, 2010.

- [49] Z. Tian, V. Veerasubramanian, P. Bianucci, S. Mukherjee, Z. Mi, A. G. Kirk, *et al.*, "Single rolled-up InGaAs/GaAs quantum dot microtubes integrated with silicon-on-insulator waveguides," *Optics express*, vol. 19, pp. 12164-12171, 2011.
- [50] L. Chrostowski and K. Iniewski, *High-speed Photonics Interconnects*: CRC Press, 2013.
- [51] I. S. Chun, K. Bassett, A. Challa, and X. Li, "Tuning the photoluminescence characteristics with curvature for rolled-up GaAs quantum well microtubes," *Applied Physics Letters*, vol. 96, p. 251106, 2010.
- [52] M. Hosoda, Y. Kishimoto, M. Sato, S. Nashima, K. Kubota, S. Saravanan, *et al.*, "Quantum-well microtube constructed from a freestanding thin quantum-well layer," *Applied physics letters*, vol. 83, pp. 1017-1019, 2003.
- [53] S. Mendach, R. Songmuang, S. Kiravittaya, A. Rastelli, M. Benyoucef, and O. Schmidt, "Light emission and wave guiding of quantum dots in a tube," *Applied physics letters*, vol. 88, p. 111120, 2006.
- [54] C. Strelow, H. Rehberg, C. Schultz, H. Welsch, C. Heyn, D. Heitmann, *et al.*, "Optical microcavities formed by semiconductor microtubes using a bottlelike geometry," *Physical review letters*, vol. 101, p. 127403, 2008.
- [55] O. G. Schmidt and K. Eberl, "Nanotechnology: Thin solid films roll up into nanotubes," *Nature*, vol. 410, pp. 168-168, 2001.
- [56] X. Li, "Strain induced semiconductor nanotubes: from formation process to device applications," *Journal of Physics D: Applied Physics*, vol. 41, p. 193001, 2008.
- [57] P. Bianucci, J. Rodríguez, C. Clements, C. Hessel, J. Veinot, and A. Meldrum, "Whispering gallery modes in silicon nanocrystal coated microcavities," *physica status solidi (a)*, vol. 206, pp. 973-975, 2009.
- [58] M. Hosoda and T. Shigaki, "Degeneracy breaking of optical resonance modes in rolled-up spiral microtubes," *Applied physics letters*, vol. 90, p. 181107, 2007.
- [59] C. Strelow, C. Schultz, H. Rehberg, H. Welsch, C. Heyn, D. Heitmann, *et al.*, "Three dimensionally confined optical modes in quantum-well microtube ring resonators," *Physical Review B*, vol. 76, p. 045303, 2007.
- [60] M. Dastjerdi, M. Djavid, S. Arafin, X. Liu, P. Bianucci, Z. Mi, et al., "Optically pumped rolled-up InAs/InGaAsP quantum dash lasers at room temperature," Semiconductor Science and Technology, vol. 28, p. 094007, 2013.
- [61] S. Hagness, D. Rafizadeh, S. Ho, and A. Taflove, "FDTD microcavity simulations: design and experimental realization of waveguide-coupled single-mode ring and whispering-gallery-mode disk resonators," *Lightwave Technology, Journal of,* vol. 15, pp. 2154-2165, 1997.
- [62] L. Ma, S. Li, V. A. B. Quiñones, L. Yang, W. Xi, M. Jorgensen, *et al.*, "Dynamic Molecular Processes Detected by Microtubular Opto-chemical Sensors Self-Assembled from Prestrained Nanomembranes," *Advanced Materials*, vol. 25, pp. 2357-2361, 2013.
- [63] G. Huang, V. A. Bolaños Quiñones, F. Ding, S. Kiravittaya, Y. Mei, and O. G. Schmidt, "Rolled-up optical microcavities with subwavelength wall thicknesses for enhanced liquid sensing applications," *Acs Nano*, vol. 4, pp. 3123-3130, 2010.

- [64] V. A. B. Quinones, L. Ma, S. Li, M. Jorgensen, S. Kiravittaya, and O. G. Schmidt, "Localized optical resonances in low refractive index rolled-up microtube cavity for liquid-core optofluidic detection," *Applied Physics Letters*, vol. 101, p. 151107, 2012.
- [65] D. J. Thurmer, C. Deneke, Y. Mei, and O. G. Schmidt, "Process integration of microtubes for fluidic applications," *Applied physics letters*, vol. 89, p. 223507, 2006.
- [66] S. M. Harazim, W. Xi, C. K. Schmidt, S. Sanchez, and O. G. Schmidt, "Fabrication and applications of large arrays of multifunctional rolled-up SiO/SiO 2 microtubes," *Journal of Materials Chemistry*, vol. 22, pp. 2878-2884, 2012.
- [67] S. M. Harazim, V. A. B. Quiñones, S. Kiravittaya, S. Sanchez, and O. G. Schmidt, "Lab-in-a-tube: on-chip integration of glass optofluidic ring resonators for label-free sensing applications," *Lab on a Chip*, vol. 12, pp. 2649-2655, 2012.
- [68] Q. Zhong, Z. Tian, V. Veerasubramanian, M. Dastjerdi, Z. Mi, and D. V. Plant, "Thermally controlled coupling of a rolled-up microtube integrated with a waveguide on a silicon electronic-photonic integrated circuit," *Optics letters*, vol. 39, pp. 2699-2702, 2014.
- [69] S. Bhowmick, T. Frost, and P. Bhattacharya, "Quantum dot rolled-up microtube optoelectronic integrated circuit," *Optics letters*, vol. 38, pp. 1685-1687, 2013.
- [70] S. Böttner, S. Li, M. R. Jorgensen, and O. G. Schmidt, "Vertically aligned rolled-up SiO2 optical microcavities in add-drop configuration," *Applied Physics Letters*, vol. 102, p. 251119, 2013.
- [71] S. Bhowmick, J. Heo, and P. Bhattacharya, "A quantum dot rolled-up microtube directional coupler," *Applied Physics Letters*, vol. 101, p. 171111, 2012.
- [72] M. Dastjerdi and Z. Mi, "Nanoscale rolled-up InAs quantum dot tube photodetector," *Electronics Letters*, vol. 50, pp. 680-682, 2014.
- [73] H. Ji, Y. Mei, and O. G. Schmidt, "Swiss roll nanomembranes with controlled proton diffusion as redox micro-supercapacitors," *Chemical Communications*, vol. 46, pp. 3881-3883, 2010.
- [74] R. Sharma, C. C. B. Bufon, D. Grimm, R. Sommer, A. Wollatz, J. Schadewald, *et al.*, "Large-Area Rolled-Up Nanomembrane Capacitor Arrays for Electrostatic Energy Storage," *Advanced Energy Materials*, 2014.
- [75] W. Xi, C. K. Schmidt, S. Sanchez, D. H. Gracias, R. E. Carazo-Salas, S. P. Jackson, *et al.*, "Rolled-up Functionalized Nanomembranes as Three-Dimensional Cavities for Single Cell Studies," *Nano letters*, 2014.
- [76] W. Huang, X. Yu, P. Froeter, R. Xu, P. Ferreira, and X. Li, "On-Chip Inductors with Self-Rolled-Up SiN x Nanomembrane Tubes: A Novel Design Platform for Extreme Miniaturization," *Nano letters*, vol. 12, pp. 6283-6288, 2012.
- [77] G. Huang, Y. Mei, D. J. Thurmer, E. Coric, and O. G. Schmidt, "Rolled-up transparent microtubes as two-dimensionally confined culture scaffolds of individual yeast cells," *Lab on a Chip*, vol. 9, pp. 263-268, 2009.
- [78] A. A. Solovev, Y. Mei, E. Bermúdez Ureña, G. Huang, and O. G. Schmidt, "Catalytic Microtubular Jet Engines Self-Propelled by Accumulated Gas Bubbles," *Small*, vol. 5, pp. 1688-1692, 2009.

- [79] M. A. Khan, M. Shatalov, H. Maruska, H. Wang, and E. Kuokstis, "III–nitride UV devices," *Japanese journal of applied physics*, vol. 44, p. 7191, 2005.
- [80] R. Halliday, "Key Benefits of Next-Gen UV LED Technology."
- [81] P. E. Editors, "Next Generation UV LED Technology Benefits Industrial Curing, Coating," 2012.
- [82] T. Egawa and B. A. B. A. Shuhaimi, "High performance InGaN LEDs on Si (1 1 1) substrates grown by MOCVD," *Journal of Physics D: Applied Physics*, vol. 43, p. 354008, 2010.
- [83] C. Lee, V. Ramachandran, A. Sagar, R. M. Feenstra, D. W. Greve, W. Sarney, *et al.*, "Properties of GaN epitaxial layers grown on 6H-SiC (0001) by plasma-assisted molecular beam epitaxy," *Journal of electronic materials*, vol. 30, pp. 162-169, 2001.
- [84] M. Haeberlen, D. Zhu, C. McAleese, M. Kappers, and C. Humphreys, "Dislocation reduction in MOVPE grown GaN layers on (111) Si using SiNx and AlGaN layers," in *Journal of Physics: Conference Series*, 2010, p. 012017.
- [85] H.-Y. Shin, S. Kwon, Y. Chang, M. Cho, and K. Park, "Reducing dislocation density in GaN films using a cone-shaped patterned sapphire substrate," *Journal of Crystal Growth*, vol. 311, pp. 4167-4170, 2009.
- [86] F. Glas, "Critical dimensions for the plastic relaxation of strained axial heterostructures in free-standing nanowires," *Physical Review B*, vol. 74, p. 121302, 2006.
- [87] D. Eaglesham and M. Cerullo, "Dislocation-free stranski-krastanow growth of Ge on Si (100)," *Physical Review Letters*, vol. 64, p. 1943, 1990.
- [88] S. Zhao, M. Kibria, Q. Wang, H. Nguyen, and Z. Mi, "Growth of large-scale vertically aligned GaN nanowires and their heterostructures with high uniformity on SiO x by catalyst-free molecular beam epitaxy," *Nanoscale*, vol. 5, pp. 5283-5287, 2013.
- [89] C. Strelow, M. Sauer, S. Fehringer, T. Korn, C. Schüller, A. Stemmann, *et al.*, "Time-resolved studies of a rolled-up semiconductor microtube laser," *Applied Physics Letters*, vol. 95, p. 221115, 2009.
- [90] J. Heo, S. Bhowmick, and P. Bhattacharya, "Threshold Characteristics of Quantum Dot Rolled-Up Microtube Lasers," *Quantum Electronics, IEEE Journal of*, vol. 48, pp. 927-933, 2012.
- [91] P. Bhattacharya and Z. Mi, "Quantum-dot optoelectronic devices," *Proceedings of the IEEE*, vol. 95, pp. 1723-1740, 2007.
- [92] P. Poole, K. Kaminska, P. Barrios, Z. Lu, and J. Liu, "Growth of InAs/InP-based quantum dots for 1.55 µm laser applications," *Journal of Crystal Growth*, vol. 311, pp. 1482-1486, 2009.
- [93] K. Dietrich, C. Strelow, C. Schliehe, C. Heyn, A. Stemmann, S. Schwaiger, *et al.*, "Optical modes excited by evanescent-wave-coupled PbS nanocrystals in semiconductor microtube bottle resonators," *Nano letters*, vol. 10, pp. 627-631, 2010.
- [94] P. Bianucci, S. Mukherjee, M. H. T. Dastjerdi, P. J. Poole, and Z. Mi, "Self-organized InAs/InGaAsP quantum dot tube lasers," *Applied Physics Letters*, vol. 101, p. 031104, 2012.

- [95] G. Bjork and Y. Yamamoto, "Analysis of semiconductor microcavity lasers using rate equations," *Quantum Electronics, IEEE Journal of,* vol. 27, pp. 2386-2396, 1991.
- [96] E. M. Purcell, "Spontaneous emission probabilities at radio frequencies," *Physical Review*, vol. 69, p. 681, 1946.
- [97] Z. Tian, P. Bianucci, P. J. Roche, M. Dastjerdi, Z. Mi, P. J. Poole, *et al.*, "Dynamical thermal effects in InGaAsP microtubes at telecom wavelengths," *Optics letters*, vol. 37, pp. 2712-2714, 2012.
- [98] R. Soref, "The past, present, and future of silicon photonics," *Selected Topics in Quantum Electronics, IEEE Journal of*, vol. 12, pp. 1678-1687, 2006.
- [99] J. Hartmann, A. Abbadie, A. Papon, P. Holliger, G. Rolland, T. Billon, *et al.*, "Reduced pressure–chemical vapor deposition of Ge thick layers on Si (001) for 1.3–1.55-μm photodetection," *Journal of Applied Physics*, vol. 95, pp. 5905-5913, 2004.
- [100] I. Sandall, J. S. Ng, J. P. David, C. H. Tan, T. Wang, and H. Liu, "1300 nm wavelength InAs quantum dot photodetector grown on silicon," *Optics express*, vol. 20, pp. 10446-10452, 2012.
- [101] Z. Sheng, L. Liu, J. Brouckaert, S. He, and D. Van Thourhout, "InGaAs PIN photodetectors integrated on silicon-on-insulator waveguides," *Optics express*, vol. 18, pp. 1756-1761, 2010.
- [102] Z. Mi, J. Yang, P. Bhattacharya, G. Qin, and Z. Ma, "High-performance quantum dot lasers and integrated optoelectronics on Si," *Proceedings of the IEEE*, vol. 97, pp. 1239-1249, 2009.
- [103] K. Yu, A. Lakhani, and M. C. Wu, "Subwavelength metal-optic semiconductor nanopatch lasers," *Optics express*, vol. 18, pp. 8790-8799, 2010.
- [104] Y. Halioua, T. Karle, F. Raineri, P. Monnier, I. Sagnes, G. Roelkens, *et al.*, "Hybrid InP-based photonic crystal lasers on silicon on insulator wires," *Applied Physics Letters*, vol. 95, p. 201119, 2009.
- [105] H.-G. Park, S.-H. Kim, M.-K. Seo, Y.-G. Ju, S.-B. Kim, and Y.-H. Lee, "Characteristics of electrically driven two-dimensional photonic crystal lasers," *Quantum Electronics, IEEE Journal of*, vol. 41, pp. 1131-1141, 2005.
- [106] S. J. Emelett and R. A. Soref, "Electrically pumped Group IV semiconductor micro-ring laser," ed: Google Patents, 2008.
- [107] J. Lott, N. Ledentsov, V. Ustinov, N. Maleev, A. Zhukov, A. Kovsh, *et al.*, "InAs-InGaAs quantum dot VCSELs on GaAs substrates emitting at 1.3 μm," *Electronics Letters*, vol. 36, pp. 1384-1385, 2000.
- [108] J. Ho, J. Tatebayashi, S. Sergent, C. F. Fong, S. Iwamoto, and Y. Arakawa, "Low threshold near infrared GaAs-AlGaAs core-shell nanowire plasmon laser," *ACS Photonics*, 2014.
- [109] M. H. MacDougal, P. D. Dapkus, V. Pudikov, H. Zhao, and G. M. Yang, "Ultralow threshold current vertical-cavity surface-emitting lasers with AlAs oxide-GaAs distributed Bragg reflectors," *Photonics Technology Letters*, *IEEE*, vol. 7, pp. 229-231, 1995.
- [110] K. Lau, P. Derry, and A. Yariv, "Ultimate limit in low threshold quantum well GaAlAs semiconductor lasers," *Applied physics letters*, vol. 52, pp. 88-90, 1988.

- [111] B. Ellis, M. A. Mayer, G. Shambat, T. Sarmiento, J. Harris, E. E. Haller, *et al.*, "Ultralow-threshold electrically pumped quantum-dot photonic-crystal nanocavity laser," *Nature Photonics*, vol. 5, pp. 297-300, 2011.
- [112] M. H. T. Dastjerdi, M. Djavid, and Z. Mi, "An electrically injected rolled-up semiconductor tube laser," *Applied Physics Letters*, vol. 106, p. 021114, 2015.
- [113] E. F. Schubert, T. Gessmann, and J. K. Kim, *Light emitting diodes*: Wiley Online Library, 2005.
- [114] H. P. T. Nguyen, M. Djavid, K. Cui, and Z. Mi, "Temperature-dependent nonradiative recombination processes in GaN-based nanowire white-light-emitting diodes on silicon," *Nanotechnology*, vol. 23, p. 194012, 2012.
- [115] T. Frost, S. Jahangir, E. Stark, S. Deshpande, A. Hazari, C. Zhao, *et al.*, "Monolithic Electrically Injected Nanowire Array Edge-Emitting Laser on (001) Silicon," *Nano letters*, vol. 14, pp. 4535-4541, 2014.
- [116] A. Vajpeyi, A. Ajagunna, G. Tsiakatouras, A. Adikimenakis, E. Iliopoulos, K. Tsagaraki, *et al.*, "Spontaneous growth of III-nitride nanowires on Si by molecular beam epitaxy," *Microelectronic Engineering*, vol. 86, pp. 812-815, 2009.
- [117] T. Stoica, R. Meijers, R. Calarco, T. Richter, and H. Lüth, "MBE growth optimization of InN nanowires," *Journal of crystal growth*, vol. 290, pp. 241-247, 2006.
- [118] K. Bertness, A. Roshko, N. Sanford, J. Barker, and A. Davydov, "Spontaneously grown GaN and AlGaN nanowires," *Journal of crystal growth*, vol. 287, pp. 522-527, 2006.
- [119] S. Zhao, A. T. Connie, M. H. T. Dastjerdi, X. H. Kong, Q. Wang, M. Djavid, et al., "Aluminum Nitride Nanowire Light Emitting Diodes: Breaking the Fundamental Bottleneck of Deep Ultraviolet Light Sources," *Scientific Reports*, 2015
- [120] M. M. Hawkeye and M. J. Brett, "Glancing angle deposition: Fabrication, properties, and applications of micro-and nanostructured thin films," *Journal of Vacuum Science & Technology A*, vol. 25, pp. 1317-1335, 2007.
- [121] Y. Taniyasu, M. Kasu, and T. Makimoto, "An aluminium nitride light-emitting diode with a wavelength of 210 nanometres," *Nature*, vol. 441, pp. 325-328, 2006.
- [122] M. Djavid, Z. Mi, "Achieving High Efficiency Deep Ultraviolet LEDs by Using Nanowire Structures," Submitted to *Optics Express*, 2015.
- [123] A. M. Armani, R. P. Kulkarni, S. E. Fraser, R. C. Flagan, and K. J. Vahala, "Label-free, single-molecule detection with optical microcavities," *science*, vol. 317, pp. 783-787, 2007.
- [124] M. Djavid, X. Liu, and Z. Mi, "Improvement of the light extraction efficiency of GaN-based LEDs using rolled-up nanotube arrays," *Optics Express*, vol. 22, pp. A1680-A1686, 2014.
- [125] Y. Mei, D. J. Thurmer, C. Deneke, S. Kiravittaya, Y.-F. Chen, A. Dadgar, *et al.*, "Fabrication, self-assembly, and properties of ultrathin AlN/GaN porous crystalline nanomembranes: tubes, spirals, and curved sheets," *Acs Nano*, vol. 3, pp. 1663-1668, 2009.

- [126] A. Splendiani, L. Sun, Y. Zhang, T. Li, J. Kim, C.-Y. Chim, *et al.*, "Emerging photoluminescence in monolayer MoS2," *Nano letters*, vol. 10, pp. 1271-1275, 2010.
- [127] H. R. Gutiérrez, N. Perea-López, A. L. Elías, A. Berkdemir, B. Wang, R. Lv, et al., "Extraordinary room-temperature photoluminescence in WS2 monolayers," arXiv preprint arXiv:1208.1325, 2012.
- [128] M. A. El-Sayed, "Small is different: shape-, size-, and composition-dependent properties of some colloidal semiconductor nanocrystals," *Accounts of chemical research*, vol. 37, pp. 326-333, 2004.
- [129] Q. Wang, E. Wang, Z. Pan, Y. Gao, B. Li, Z. Jia, et al., "Self-rolled-up InGaAs/GaAs microtubes fabricated directly on Si (100) substrates," *Journal of Vacuum Science & Technology B*, vol. 32, p. 030603, 2014.